

ABSTRACT

Title of Document: FIELD OBSERVATIONS AND MODEL
 SIMULATIONS OF LOW-LEVEL FLOWS
 OVER THE MID-ATLANTIC DURING
 AUGUST 1-5, 2006.

 Scott Daniel Rabenhorst, Doctor of Philosophy,
 2012

Directed By: Professor Da-Lin Zhang
 Department Atmospheric and Oceanic Science

For years, basic mountain, sea breeze, and low-level jet (LLJ) circulations have been studied, usually in locations with a high frequency of occurrence, sharp gradients, or significant geographic prominence. However, there is evidence that similar circulations exist in non-classic locations with more mild topography and atmospheric gradients. One such understudied area is the U.S. Mid-Atlantic region.

The Water Vapor Variability – Satellite/Sondes (WAVES) 2006 field campaign provided a contiguous 5-day period of concentrated high resolution observations to examine fine-scale details of a weather pattern typical of the Mid-Atlantic summertime. These measurements presented an opportunity for an intensive modeling study to further investigate peculiar phenomena with verification against research-grade observations.

The observations captured two significant events: an official LLJ and a cold front with a prefrontal trough. A pronounced diurnal cycle was revealed which can be categorized into three stages: (1) daytime growth of the planetary boundary layer (PBL), (2) flow intensification into a LLJ regime after dusk, and (3) interruption by downslope winds (DW) after midnight. The third stage is most interesting owing to the lack of literature documenting similar occurrences in the Mid-Atlantic, which can impact air quality forecasting.

Prior to high resolution modeling of the case study, sensitivity studies were conducted examining four areas to which the model was believed most sensitive: (1) initial condition data, (2) cumulus schemes, (3) PBL parameterizations, and (4) initialization times. Results also revealed shortcomings in model precipitation and PBL profiles, model biases, urban anomalies, and tendencies for forecast convergence.

High resolution regional modeling showed the evolution of these nocturnal events and were verified against WAVES observations. A hybrid solenoidal influenced afternoon and early evening circulation east of the mountains. Afternoon deepening of a lee trough by an oscillating warm air band influenced low-level wind fields. Wind flow was further influenced by the thermal wind that originated over sloping terrain. Airflow traversed the Appalachian barrier and moved down the east flank of the Appalachians with katabatic and hydraulic contributions. This DW swept the LLJ regime off to the southeast. The prefrontal LLJ outflow in the Midwest strengthened DW events as the cold front approached.

FIELD OBSERVATIONS AND MODEL SIMULATIONS OF LOW-LEVEL
FLOWS IN THE MID-ATLANTIC DURING AUGUST 1-5, 2006.

By

Scott Daniel Rabenhorst

Dissertation submitted to the Faculty of the Graduate School of the
University of Maryland, College Park, in partial fulfillment
of the requirements for the degree of
Doctor of Philosophy
2012

Advisory Committee:

Professor Da-Lin Zhang, Chair and Academic Advisor

Dr. David N. Whiteman, Research Advisor

Distinguished Professor Eugenia Kalnay

Professor Russell Dickerson

Professor Belay Demoz

Professor Michael Evans

© Copyright by
Scott Daniel Rabenhorst
2012

Dedication

To my beautiful wife Regina for your love, support, patience, and encouragement through these years. To my mother and father who inspired my interest in meteorology and rallied behind my pursuit of the Ph.D.

Acknowledgements

First and foremost, I want to thank my wife for her love, unending support, and for carrying the burden of daily demands while I focused on my academics and research. She provided continual encouragement and optimism throughout my graduate career and devoted many hours to proofing my work. I want to thank my family and in-laws for their prayers and support. The interest they had in my work was heartfelt and meaningful. I thank my mother and father for inspiring me to study meteorology and reach high for this goal. To my friends, thank you for your help, advice and support. In particular, thanks to Debra Baker, Dave Kuhl, and Elizabeth Satterfield who helped me along the way. They are not just as colleagues but great friends.

I am forever indebted to Dr. David N. Whiteman, my advisor and mentor. He has continually taken every opportunity to help me succeed and prepare me for this career. At the same time, he has granted me freedom to pursue my research and showed compassion and flexibility during periods when I faced personal injury. He has graciously supported my time at AOSC and additionally provided resources for my research. The field experience I gained by working with him during all the WAVES campaigns was invaluable, in particular the RASL flight missions during 2007. His support has been unwavering and his character exemplifies what every graduate student hopes for in an advisor.

I am grateful to my committee members and for their time investment. I have learned so much through the insight of Professor Da-Lin Zhang, who has been exceptionally responsive with helpful feedback and always with an open door. He has

spent much time to help me become a great researcher. Likewise, I have been privileged to learn from Professor Eugenia Kalnay who has always been encouraging and uplifting. Dr Belay Demoz has been a constant source for advice and help. To my other committee members Professor Russell Dickerson and Professor Michael Evans, UMD faculty, and AOSC staff, thank you for all your help.

I also want to thank the Aura validation project for funding the WAVES 2006 campaign, Howard University for allowing the use of their facility and data, and the staff at Maryland Department of the Environment for their profiler and air quality data.

Table of Contents

Dedication.....	ii
Acknowledgements.....	iii
Table of Contents.....	v
List of Tables.....	viii
List of Figures.....	ix
Chapter 1: Introduction.....	1
1.1 WAVES Field Campaign.....	4
1.1.1 Overview.....	4
1.1.2 Instrumentation.....	6
1.2 Thermal Circulations.....	9
1.2.1 Low-level jets.....	9
1.2.2 Mountain circulations.....	12
1.2.3 Sea breezes.....	14
1.3 Mountain Waves.....	15
1.4 Nocturnal PBL.....	17
1.5 Research Objectives.....	18
Chapter 2: Observational Detection of Fine Scale Phenomena.....	20
2.1 Synoptic Overview.....	20
2.1.1 Steering level charts.....	20
2.1.2 Surface charts.....	24
2.2 Analysis of Diurnal Variations.....	27
2.2.1 WAVES profiling.....	27
2.2.2 WAVES surface observations.....	30
2.2.3 WAVES soundings.....	38
2.2.4 Regional wind profilers.....	39
2.2.5 Regional WeatherBug network.....	44
2.3 Discussion.....	47
2.3.1 Stage I: Convective boundary layer.....	50
2.3.2 Stage II: Nocturnal low-level jet regime.....	51
2.3.3 Stage III: Downslope wind regime.....	54
2.3.4 Inertial oscillation.....	55
2.3.5 Prefrontal trough.....	58
2.3.6 Cold front.....	60
2.4 Summary.....	62
Chapter 3: Numerical Simulations.....	65
3.1 Experiment Design.....	65
3.1.1 Control run.....	66
3.1.2 Terrain height modification.....	68
3.2 Model Verification.....	69
3.2.1 Winds.....	69
3.2.2 Mixing ratio.....	73
3.2.3 Planetary boundary layer height.....	75
3.3 Analysis of Regional Flow.....	77

3.3.1	Horizontal evolution	77
3.3.2	Vertical structure.....	83
3.4	Contributions to Nocturnal Downslope Winds.....	86
3.4.1	Cross-Appalachian wind flow.....	87
3.4.2	Prefrontal LLJ	87
3.4.3	Potential vorticity.....	92
3.4.4	Influence of mountain height.....	93
3.5	Daytime Solenoidal Forcing	94
3.6	Thermal forcing	99
3.6.1	Warm air anomaly.....	99
3.6.2	Thermal wind.....	102
3.7	Summary and Conclusions	105
Chapter 4:	Model Sensitivity Studies	110
4.1	Experiment Design.....	114
4.2	Sensitivity to Model Initial Conditions.....	114
4.2.1	Upper-air verification.....	115
4.2.2	Surface verification.....	116
4.2.3	WAVES verification.....	118
4.3	Sensitivity to Model Cumulus Schemes	119
4.3.1	Upper-air verification.....	120
4.3.2	Surface verification.....	121
4.3.3	Precipitation verification.....	124
4.4	Sensitivity to Model Planetary Boundary Layer Parameterizations.....	130
4.4.1	Upper-air verification.....	131
4.4.2	Surface verification.....	132
4.4.3	WAVES verification.....	134
4.4.4	Precipitation verification.....	139
4.5	Results Discussion	141
Chapter 5:	Summary and Future Work.....	147
Glossary of	Acronyms	154
Appendix A:	Sensitivity to Model Initialization Time	158
A.1	Upper-air verification.....	159
A.2	Surface verification	159
A.3	Precipitation verification.....	159
A.4	WAVES verification.....	161
Appendix B:	Post-processing and Graphics Generation.....	169
B.1	WRF Output	169
B.2	Intermediate Processing	169
B.3	Mathematica Graphics.....	170
B.3.1	Function "ArrayPlot".....	170
B.3.2	Function "ListContourPlot".....	171
B.3.3	Function "ListVectorPlot".....	171
B.3.4	Graphics primitives	172
B.3.5	Function "Show"	172
B.3.6	Tick marks.....	173
B.3.6	GIS data.....	174

B.4 Adobe Software.....	174
Bibliography	176

List of Tables

Table 3.1: WRF Configuration for IC Sensitivity Tests	115
---	-----

List of Figures

- Figure 1.1: The Mid-Atlantic is a complex region with 7 distinct geographies (a): Western slopes (blue), Appalachian Highlands (red), Ridge and Valley region (orange), the Great Valley (purple), Blue Ridge Mountain range (cyan), Piedmont Plateau (green), and the Coastal Plains (yellow). The coastal plains are further subdivided into the Western and Eastern Shores to the west and east of the Chesapeake Bay, respectively. The corresponding terrain is shown on right (b).....2
- Figure 2.1: Six day sequence of NARR reanalysis showing 500 mb temperature (shading) and geopotential height (contours). Frontal boundaries and troughs from Unisys surface analysis are superimposed. The purple line identifies a trough rotating around L0. Reanalysis times are (a) 0000 UTC 1 Aug, (b) 0000 UTC 2 Aug, (c) 0000 UTC 3 Aug, (d) 0000 UTC 4 Aug, (e) 0000 UTC 5 Aug, (f) 0000 UTC 6 Aug.23
- Figure 2.2: Nexrad composite radar reflectivity (dBZ) and RUC sea level pressure contours (hPa) are overlaid on shaded relief at times (a) 1900 UTC 3 Aug, (b) 2300 UTC 3 Aug, (c) 0400 UTC 4 Aug, (d) 0900 UTC 4 Aug, (e) 2100 UTC 4 Aug, and (f) 0000 UTC 5 Aug. The surface cold front (blue line) and prefrontal trough (yellow dashed line) are drawn based on analysis of RUC 950 mb fields.....26
- Figure 2.3: HUBC 4 km AGL time series from 0000 UTC 1 August to 0000 UTC 6 Aug. Panels show (a) SRL water vapor mixing ratio, (b) SRL

aerosol scattering ratio, (c) MDE wind speed, and (d) direction. Gray shaded background indicates nighttime periods. "J", "D", and "F" designate low-level jet, downslope winds, and cold front events.....28

Figure 2.4: Surface observations collected at HUBC from 0000 UTC 1 August to 0000 UTC 6 Aug. Panel (a) shows air quality measurements. PM units are $\mu\text{g m}^{-3}$. O_3 , SO_2 , NO_y , NO_x have units of ppb. CO is ppb/10. Panel (b) shows precipitable water vapor and temperature from the 31 m meteorological tower. Panel (c) shows wind speed and direction at the tower top. Panel (d) shows surface pressure and mixing ratio at the tower base and top. Gray shaded background indicates nighttime periods.32

Figure 2.5: The Mid-Atlantic is a complex region with of seven distinct regional geographies: (1) Western Upslope, (2) Appalachian Mountain Highlands, (3) Ridge and Valley, (4) Great Valley, (5) Blue Ridge Mountains, (6) Piedmont Plateau, and the (7) Coastal Plains regions. The Coastal Plains are further subdivided into the Western and Eastern Shores to the west and east of the Chesapeake Bay, respectively. Locations A-Z were WeatherBug sites selected to observe surface winds. The nearest operational wind profilers during this case study are labeled in yellow. The distance between the profiler sites and the Appalachian Mountains was approximately 30, 75, 125, and 190 km for RUTNJ, BLTMD, CHANC, and RALNC, respectively.40

Figure 2.6: Comparison of wind direction between profilers at (a) Rutgers, NJ, (b) Beltsville, MD, (c) Raleigh, NC, and (d) Charlotte, NC from 0000 UTC 1 August to 0000 UTC 6 Aug. These locations are marked in Figure 2.5. White lines mark the beginning of the DW regime at HUBC. Gray shaded background indicates nighttime periods.42

Figure 2.7: Same as Figure 2.6 except showing wind speed.44

Figure 2.8: WeatherBug surface wind observations from 2100 UTC 1 Aug to 1200 UTC 2 Aug. Station sites are labeled A-Q and correspond to the locations in Figure 2.5. Vectors are oriented with the wind flow. Two red lines are superimposed to delineate the nocturnal transitions that propagated from west-to-east. Line α marks the change in wind direction and β marks the change in wind speed.46

Figure 2.9: Diurnal evolution of (a) the classic boundary layer depicted by Stull (1988) and a (b) modified PBL evolution according to case study observations.48

Figure 2.10: Enlargement of Figure 2.3b showing ASR data for 1 August. Important features are labeled. The blue line shows lifting by the DW, and the cyan line traces the top of the developing CBL.51

Figure 2.11: Enlargement of nocturnal phenomena from 1800 UTC 1 August to 1200 UTC 2 August. Panels show (a) ASR, wind (b) direction, and (c) speed. Collocated black lines are superimposed on each panel as visual

aid to help identify common features between fields. White line is the hypothesized PBLT.....	52
Figure 2.12: LLJ observed by Beltsville profiler showing (a) wind direction and (b) wind speed from 0430-0545 UTC 1 August.	53
Figure 2.13: MDE wind profiler hodographs for the periods: (a,c,e) 2000 UTC 1 August to 1500 UTC 2 August, and (b,d,f) 2000 UTC 2 August to 1500 UTC 3 August. Hodographs are shown at three heights: (a,b) 0.5 km, (c,d) 1 km, and (e,f) 1.5 km.	57
Figure 2.14: Enlargement of Figure 2.3b showing ASR data on 4 August. Yellow lines accentuate the DW air mass, with arrows indicating areas of lifting. The DW event was greatly enhanced by the prefrontal trough compared with previous days.....	59
Figure 2.15: (a) Water vapor satellite image at 2245 UTC. Blue (orange) arrow(s) show the general motion of the frontal boundary (upper-level clouds). (b) The KLWX (Sterling, VA) base reflectivity at 2110 UTC shows refractive lines, in the circled area, which were moving opposite of the upper-level clouds.....	61
Figure 3.1: Locations of outer domain (D01) and nested domain (D02) outlined in yellow. WRF terrain elevation scaled by (a) 100% in run IN212, (b) 40% in run IN212L, and (c) 200% in run IN212H.	67
Figure 3.2: Observed (a) and control run (b) wind direction indicated by shading. Sunrise (dashed lines), sunset (dotted lines), nocturnal periods	

(gray) are indicated, Model (black line) and observed (white line) PBLT are superimposed on both panels.70

Figure 3.3: Mean LLJ profiles showing wind (a) speed ($m s^{-1}$) and (b) direction (degrees) from 0100-0400 UTC 3 Aug. Mean DW profiles showing wind (c) speed and (d) direction from 0800-1200 UTC 3 Aug. Mean post-frontal wind profiles showing wind (e) speed and (f) direction from 0800-1200 UTC 5 Aug. Wind observation profiles are plotted using blue/green lines, and model profiles use red/purple lines. Northwest quadrant of wind direction is shaded gray.71

Figure 3.4: Observed (a) and control run (b) mixing ratio indicated by shading. Model error (c) from subtracting b from a. All units in $g kg^{-1}$. White areas mask out background noise during the daytime. Rest as in Figure 3.2.....74

Figure 3.5: WRF wind direction at 500 m MSL. Gray areas indicate elevations exceeding the plane height, the yellow dot indicates the HUBC location, and terrain is shown in (a). Wind direction at times (b) 1730, (c) 2000, (d) 0100, (e) 0500 , and (f) 0900 UTC show the diurnal transition of wind direction from northwesterly to southwesterly and back to northwesterly again. The blue line in panel (a) indicates the location of the vertical cross sections in Figure 3.6.78

Figure 3.6: Vertical cross sections from D2 of run IN212 located along the cyan line marked in Figure 3.5a. Shaded areas show (a) θ_e at 2200 UTC 2 Aug, (b) WDIR at 0100 UTC 3 Aug, and (c) WSPD at 0600 UTC 3

Aug. Contours indicate θ spaced every 2 K with a white line every 10 K. Vectors represent U-W components of wind on a vertical plane. Solid brown is the surface terrain and the blue lines on top show the location of water bodies. Hatched pattern indicates areas with positive V-wind.84

Figure 3.7: WRF output at 0500 UTC 3 August for D01. Horizontal 600 m MSL planes show (e) WSPD and (d) WDIR. Lines [A,B,C] in panels (d-e) show the locations of the vertical cross sections (a,b,c), respectively. WSPD (shading), θ (contours), and positive V-wind (hatching) is shown in panels (a-c).....89

Figure 3.8: Panels (a-c) show model output from runs using 200% (Figure 3.1c), 100% (Figure 3.1a), and 40% (Figure 3.1b) Appalachian Mountain height. The simulation time is 2300 UTC 2 August. The x-axes extend from the Ohio-Indiana-Kentucky border to the Atlantic Ocean. Shading shows the cross-barrier wind speed whereby warm (cool) colors indicate positive (negative) west-to-east (east-to-west) flow over the mountains. Contours show θ and streamlines show the wind field on the vertical plane. Magenta dots (lines) reveal the centers (axis) of circulation about the leeside solenoids.95

Figure 3.9: Horizontal planes at 500 m ASL which show temperature (shading), geopotential heights (contours), and wind vectors at (a) 1500 UTC 2 Aug, (b) 2300 UTC 2 Aug, (c) 0300 UTC 3 Aug, and (d) 1000 UTC 3 Aug. A green dashed line marks an abrupt change in wind direction, and usually correlated with the lee trough. Geopotential heights were

smoothed using a Gaussian filter with a temporal window of 2 h and a spatial radius of 10 km to eliminate noise from high-frequency waves. Wind data were smoothed spatially using the same technique. No vertical smoothing was applied.....100

Figure 3.10: Top halves of each graphic show the diurnal temperature evolution at (a) 950 hPa and (b) 900 hPa along an east-west transect in D2 over Baltimore, MD. The legend shows the temperature curve at a given hour. The bottom halves of each graphic show the (a) 950 hPa and (b) 900 hPa horizontal planes in relation to surface pressure (brown terrain). In the top panel, the red (blue) line is a visual aid and approximates a tangent to the isotherms associated with period of maximum heating (cooling). The white arrow indicates tilting of the isotherms throughout the night. In the bottom panel, black lines provide a visual aid to illustrate a more uniform temperature field throughout the night at 900 hPa.....103

Figure 4.1: ACARS Temperature Mean Error for IC Sensitivity Tests.116
 Figure 4.2: SFC Temperature Mean Error for IC Sensitivity Tests.....117
 Figure 4.3: SFC Mixing Ratio Mean Error for IC Sensitivity Tests.....117
 Figure 4.4: SFC Precipitable Water Mean Error for IC Sensitivity Tests.117
 Figure 4.5: SFC Pressure Mean Error for IC Sensitivity Tests.....118
 Figure 4.6: SRL Mixing Ratio RMSE for IC Sensitivity Tests.119
 Figure 4.7: SFC Mixing Ratio for Cumulus Sensitivity Tests.....121

Figure 4.8: SFC ME anomalies showing (a) WVMR at 1800 UTC 2 August, (b) WVMR at 2200 UTC 2 August, (c) TMP at 2100 UTC 2 August, and (d) PRES at 2100 UTC 4 August.....	124
Figure 4.9: GSS for 6-hr precipitation (neighborhood statistics).	126
Figure 4.10: Cumulus Sensitivity comparison of MODE 1-hr precipitation objects at 1900 UTC 3 August.....	128
Figure 4.11: Cumulus Sensitivity CSI for MODE objects for (a) Grell-3D, (b) Betts-Miller-Janjic, (c) Grell-Devenyi, (d) No-cumulus scheme, and (e) Kain-Fritsch.	130
Figure 4.12: SFC Mixing Ratio for PBL Sensitivity Tests.....	133
Figure 4.13: SFC Temperature for PBL Sensitivity Tests.....	134
Figure 4.14: Beltsville Temperature for PBL Sensitivity Tests.....	135
Figure 4.15: Beltsville Relative Humidity for PBL Sensitivity Tests.	137
Figure 4.16: SRL mean Error by height for PBL Sensitivity Tests.....	138
Figure 4.17: GSS for 6-hr precipitation for PBL sensitivity tests.....	141
Figure A.1: Initialization sensitivity runs compared with 1755 UTC 3 August radiosonde: left profile is (a) mixing ratio and right profile is (b) V-wind....	163
Figure A.2: Initialization sensitivity runs compared with 0559 UTC 4 August radiosonde: left profile is (a) mixing ratio and right profile is (b) V-wind....	164
Figure A.3: Initialization sensitivity runs compared with 1706 UTC 4 August radiosonde: left profile is (a) mixing ratio and right profile is (b) temperature.	165

Figure A.4: Initialization sensitivity runs compared with 2313 UTC 4 August
radiosonde: left profile is (a) mixing ratio and right profile is (b) U-wind....166

Figure A.5: Initialization sensitivity runs compared with 0601 UTC 5 August
radiosonde: left profile is (a) mixing ratio and right profile is (b)
temperature.167

Figure A.6: Initialization sensitivity runs compared with 1837 UTC 5 August
radiosonde: left profile is (a) mixing ratio and right profile is (b) V-wind....168

Chapter 1: Introduction

Regional scale dynamics can play a significant role in the transport of meteorological quantities and contaminants with wide-ranging impacts, from poor air quality downwind of urban and industrial sources to modification of precipitation patterns (Givati; Rosenfeld 2004; Jauregui; Romales 1996; Niyogi et al. 2010; Rosenfeld; Bell 2011). This is particularly relevant to the Mid-Atlantic region. The Baltimore-Washington area is a densely populated part of the East Coast; it is also a location with many parks, encouraging outdoor recreational activities where exposure to pollutants transported by local dynamics can directly impact human health. Outside the urban centers there is a large agricultural sector that is also sensitive to regional pollution. Therefore, it is particularly important to investigate and understand fine scale dynamics and their interaction with the complex geography of the Mid-Atlantic, in particular where low-level flows are exposed to surface pollution sources.

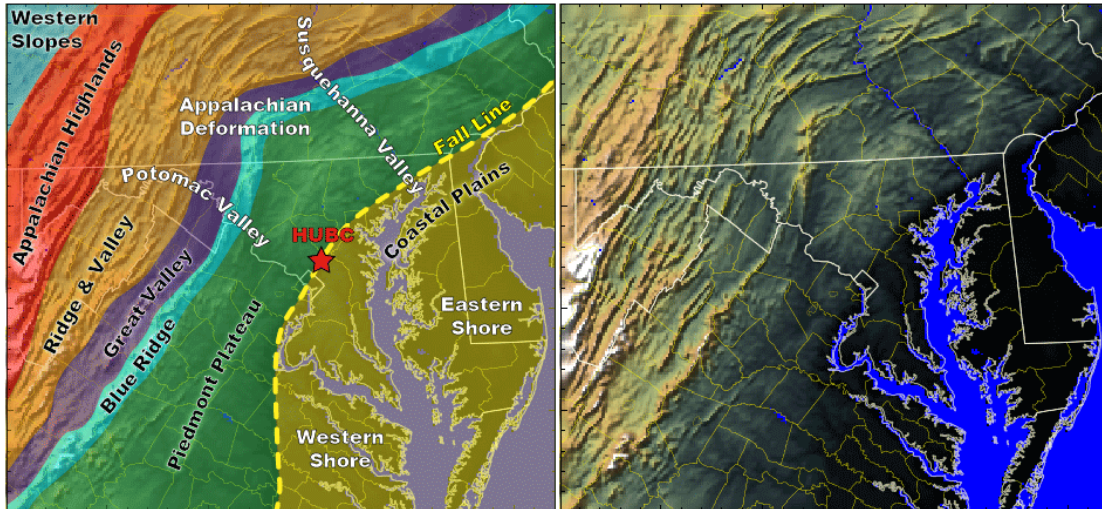


Figure 1.1: The Mid-Atlantic is a complex region with 7 distinct geographies (a): Western slopes (blue), Appalachian Highlands (red), Ridge and Valley region (orange), the Great Valley (purple), Blue Ridge Mountain range (cyan), Piedmont Plateau (green), and the Coastal Plains (yellow). The coastal plains are further subdivided into the Western and Eastern Shores to the west and east of the Chesapeake Bay, respectively. The corresponding terrain is shown on right (b).

The backdrop for Mid-Atlantic meteorology is a complex land surface and topography that includes seven distinct geographies; this is especially pertinent to low-level flows and regional circulations. Basic geographies are illustrated in Figure 1.1. The most prominent feature is the Appalachian Highlands, which has a maximum elevation (within coverage of Figure 1.1) of 1.34 km above sea level (ASL). Immediately to the west of the Appalachian Highlands are the western slopes. To the east are numerous mountain crests in the undulating terrain called the Ridge and Valley region. The average elevation of the Ridge and Valley region is notably lower than the Appalachian Highlands. Immediately east of that region are the Great Valley lowlands. The Blue Ridge Mountain range marks the eastern extent of the mountains but also poses a significant meteorological barrier for shallow circulations to the east and to the west of this range. The Piedmont Plateau is characterized by rolling hills and drops sharply down to the coastal plains along the Fall Line. The Fall Line runs

nearly parallel to the I-95 corridor. The Coastal Plains are very flat with numerous water bodies, swamps, and marshes. Another interesting feature is a deformation, or bend, in the backbone of the Appalachian Mountains near State College, PA. The deformation re-orientates the overall axis of the ridges and valleys toward the east. As a result, prevailing winds can be channeled differently to the north and south of the deformation. Lastly, the lowlands along the Potomac and Susquehanna Rivers are important because these valleys often funnel prevailing winds from the west or the north.

After a cursory review of important Mid-Atlantic geographies that affect low-level winds, this research proceeds as follows. Chapter 1 provides a brief background on the Water Vapor Variability – Satellite/Sondes (WAVES) 2006 field campaign. A concise background is provided on three different thermal circulations which affected low-level flows in the Mid-Atlantic during this case study: the nocturnal low-level jet (LLJ), mountain-plains circulation, and sea breeze. The sea breeze circulation is mentioned, not because it was directly observed as a stand-alone circulation, but because the surface gradients driving this circulation enhanced the existing LLJ and mountain-plains circulations. Additionally, a brief background on the hydraulics of mountain flows leading to downslope winds (DW) is presented. DWs can also arise from katabatic or drainage flows. In general, however, katabatic flows are thermally driven, whereas mountain hydraulics are mechanically forced. In this case study, the DW appears to have a contribution from both mechanisms. Lastly, a short background is provided on the nocturnal planetary boundary layer (PBL), since the LLJ and DW flows affected the structure of this layer during the nighttime hours.

Chapter 2 presents observations acquired during WAVES that unveiled intriguing nocturnal phenomena which motivated the investigation of this case study. Since observations alone could not confirm the source of the low-level flows nor explain their regional and temporal evolution, Chapter 3 presents high resolution numerical simulations that were conducted to address these questions. Chapter 4 highlights findings from model sensitivity studies that were conducted prior to the high resolution modeling. Chapter 5 summarizes the main conclusions from this research.

1.1 WAVES Field Campaign

Fine scale boundary layer profiling and modeling has been the focus of numerous campaigns. Studies have looked at the role of low-level winds in the transport and dispersion of pollution in complex orography (Bao et al. 2008; de Foy et al. 2006) and urban environments (Mestayer et al. 2005; Tie et al. 2009). Others closely examined the intricacies of valley flows (Fast; Darby 2004), with downslope jets (Pinto et al. 2006), on steep (De Wekker et al. 2005) or low angle slopes (Whiteman; Zhong 2008). Much knowledge has been gained through intensive field campaigns using a variety of instrumentation rarely collocated outside this context. Observations alone are important, often revealing features models cannot reproduce.

1.1.1 Overview

The WAVES field campaign commenced 27 June 2006 and continued until 12 August 2006. Measurements were centered at the Howard University research campus (HUBC) in Beltsville, MD, located at 39.0543°N, 76.8776°W (Figure 1.1) with an elevation of 52 m above sea level. This location was in between Baltimore

and Washington, DC, immediately adjacent to agricultural, industrial, and urban areas. The campaign was a collaborative effort among several government agencies and universities including the [NASA/Goddard Space Flight Center](#) (GSFC), National Oceanic and Atmospheric Administration (NOAA) - [National Weather Service](#), [Howard University](#), [University of Maryland Baltimore County](#), [Pennsylvania State University](#) (PSU), [University of Maryland College Park](#) and [Maryland's Department of the Environment](#) (MDE). The primary objective of the WAVES 2006 field campaign was to acquire a robust set of coordinated measurements that could be used for satellite validation and inter-instrument comparison, assessing variability and accuracy, with an emphasis on water vapor, ozone, temperature, and aerosol profiles. WAVES 2006 was funded under the Earth Observing System Aura satellite validation program.

Another aim of WAVES 2006 was to perform case studies on regional scale meteorological events. An intensive phase of the field campaign was launched in early August in anticipation of a series of days with poor air quality that would culminate by the passage of a weak summertime cold front. Round-the-clock measurements were conducted with the goal of capturing the pre- and post-frontal meteorology. The result was a unique continuous dataset of fine-scale observations that showed the passage of a prefrontal trough, cold front, and revealed a detailed view of the diurnal evolution of the PBL with nocturnal low-level wind maxima. This period of 1-5 August 2006 is the case study discussed in this paper.

1.1.2 Instrumentation

A host of ground-based and in-situ sensors contributed to WAVES field operations, including nine lidar systems, ten different radiosonde technologies, Doppler C-band radar, wind profiler and radio acoustic sounding system (RASS), microwave radiometer, ceilometer, whole-sky imager, broad-band and spectral radiometers, Suominet GPS total column measurements, and several air quality instruments measuring trace gases and particulates. Additionally, a 31-m instrumented tower extended just above the tree canopy. Wind, temperature, humidity, and radiation sensors were located at various heights on the tower to allow surface flux measurements.

Research lidar systems were among the most useful instruments of WAVES, providing a detailed evolution of the lower atmosphere through continuous high resolution measurements. Lidar is the optical analog to radar and began to gain recognition in the early 1960s, shortly after the invention of the pulse laser (Weitkamp 2005). There are many different types of lidar systems specialized for different measurements. Weitkamp's book provides a thorough review of this technology. Two common techniques for measuring water vapor are Differential Absorption Lidar (Bösenberg 1998; Browell et al. 1979; Ismail; Browell 1989; Wulfmeyer; Bösenberg 1998) and the Raman lidar.

The lidar data presented in this paper were acquired through Raman systems, which are named after Sir Chandrasekhara Venkata Raman, whose pioneering work in molecular physics founded Raman spectroscopy. These systems operate by emitting laser pulses into the atmosphere. Radiation strikes and energizes molecules

within the swept volume of the beam. A large portion of the momentarily excited molecules quickly release their gained energy, both rotational and vibrational, through elastic and inelastic re-emission. The inelastic scattering is spectrally shifted from the excitation wavelength. This Raman shift is unique to different molecular species, and thus it can be a reliable signature of atmospheric composition. A telescope is used to collect backscattered radiation which is spectrally selected with precise narrow-band filters, measured, and clocked.

The spectral data are processed to create a profile of various atmospheric constituents. Water vapor mixing ratio (WVMR) is derived by comparing the water vapor signal to that of nitrogen, which composes a near uniform 78% of the lower atmosphere (Goldsmith et al. 1998; Melfi et al. 1989; Turner et al. 2000; Whiteman 2003). Aerosol Scattering Ratio (ASR) was another product that was helpful in diagnosing different air masses. ASR is derived from the ratio of Mie scattering (including non-spherical objects) to molecular scattering (Ferrare et al. 2006; Whiteman 2003). ASR data typically have high return values for strong scatterers, such as particulate matter, pollutants, dust, pollen, or cloud droplets. Many other atmospheric constituents can be measured as well, such as carbon dioxide (Ansmann et al. 1992b), and other trace gases commonly measured using different filters and wavelengths. Wind (Gentry et al. 2000; Koch et al. 2008; Rees; McDermid 1990), temperature (Arshinov et al. 2005; Behrendt et al. 2002; Di Girolamo et al. 2004), cloud liquid water (Whiteman et al. 2007), cirrus clouds (Ansmann et al. 1992a; Reichardt et al. 2002; Whiteman et al. 2004), and other atmospheric information can be derived by further decomposition of the spectrum looking at the

shape of the peak and sidebands, Stokes and anti-Stokes shifts, vibrational and rotational energy, and polarization.

Simultaneous collection of wavelength-dependent backscatter gives Raman systems an advantage over other types of lidars. Datasets can be further processed to estimate other meteorological variables, such as boundary layer fluxes and height, cloud properties, and ceiling height. It is commonly stated that lidar data are under-utilized by numerical weather prediction (NWP) models for verification and assimilation.

The lidar data presented in this paper were acquired by the NASA/GSFC Scanning Raman Lidar (SRL) (Whiteman et al. 2006), with the exception of a small three hour time gap when SRL was offline. Data were “patched in” from the Howard University Raman Lidar, described in Adam et al. (2010). Both Raman lidar systems used a tripled Nd:YAG laser emitting in the near UV at 354.7nm. This excitation wavelength produces Raman-shifted scattering for nitrogen and water vapor centered near 386.7, and 407.5 nm, respectively. The WVMR and ASR data in this paper were collected using a zenith pointed beam with a vertical and temporal resolution of 30 m and 1 min, respectively. Although the SRL collected data at other wavelengths to generate several products, the discussion in this paper will focus on WVMR and ASR. More information about WAVES 2006, particularly the lidar measurements during the campaign, can be found in Adam et al. (2010).

Another important instrument during the WAVES campaign was the MDE 915 MHz radar wind profiler with RASS. Depending on atmospheric conditions, this system provided continuous PBL wind data from near the surface up to a maximum

of 4 km. However, decreasing signal to noise ratio above 3 km above ground level (AGL) generally restricted valid data to lower levels. The temporal and vertical resolution of the wind data were 15 min and 90 m, respectively. Unfortunately, the RASS virtual temperature was not operational during this case study.

The above instrumentation was used to measure the low-level flows produced by the following thermal circulations. The following sections provide a succinct review of theory behind these circulations.

1.2 Thermal Circulations

1.2.1 Low-level jets

The LLJ is the first nocturnal regime presented in a conceptual model in Chapter 2 (Figure 2.9). The LLJ was noted as early as 1935 by Farquharson (1939) and has since become the subject of numerous investigations in which many theories have been proposed regarding the formation and evolution of the LLJ. Blackadar (1957) theorized the sudden vertical decoupling in the PBL, by means of a sharp reduction of thermally-driven eddy viscosity near sunset, was sufficient to allow the development of supergeostrophic winds resulting from the rotation of the ageostrophic component around an inertial oscillation within the residual layer. However, this did not address the preferred location of the LLJ over the Great Plains. Wexler (1961) believed westward moving air circulating around the Bermuda High was deflected northward by the Rocky Mountains analogous to the behavior of the Gulf Stream Jet, thus situating the jet east of the mountains over the central Great Plains. Holton (1967) noted that previous theories insufficiently described the observed amplitude and shape of the oscillation. He showed that diurnal heating and

cooling across sloping terrain could generate thermally-driven flows from an oscillating pressure gradient force, which oriented the geostrophic wind vector perpendicular to the down-gradient direction. Consequently, the rotating vector affected the wind magnitude and the ellipticity of the oscillation. This idea was reaffirmed in other studies (Bonner; Paegle 1970). Uccellini (1980) pointed out that synoptic conditions should not be minimized and factors such as lee troughing, cyclogenesis, and upper level jet streaks also impacted LLJs. There is still uncertainty whether the dominant mechanisms influencing the LLJ are topography (Pan et al. 2004; Ting; Wang 2006), inertial oscillations (Zhong et al. 1996), sloping terrain (Parish; Oolman 2010), or other phenomena, such as modulation through vertical diffusion (Jiang et al. 2007). It is likely that some of these theories can combine synergistically to produce the observed LLJ.

The LLJ is a frequently occurring feature of the Mid-Atlantic warm season (Zhang et al. 2006) and believed to be responsible for significant transport of regional pollutants, thereby creating an antecedent environment that can enhance or reduce air quality during subsequent days. Yet there have been relatively few publications about the Mid-Atlantic LLJ, so its regional impact remains uncertain. While much of the past literature has exclusively focused on understanding the Great Plains LLJ (Bonner 1968; Jiang et al. 2007; Parish et al. 1988; Song et al. 2005), there is an increasing awareness that these features occur around the world (Rife et al. 2010) with varying characteristics and evolution. While more research is needed in these understudied areas, such as the LLJs along the US East Coast, some notable literature has documented LLJ occurrences in Florida (Karipot et al. 2009), the Carolinas (Sjostedt

et al. 1990), the Mid-Atlantic (Zhang et al. 2006), Pennsylvania (Verghese et al. 2003), and New York (Colle; Novak 2009). More attention should be given to the local mechanisms driving these LLJs and unique characteristics affected by their particular environment in order to better understand their evolution and prediction.

The Mid-Atlantic warm season climatology reveals that a majority of events with low-level wind speed maxima have a southwesterly direction, analogous to the Great Plains LLJ (Zhang et al. 2006). However, there are still many events that center about other wind directions. Such cases are suspected of being influenced by other mechanisms.

Past research has used various criteria to define LLJ cases, such as fixed (Banta et al. 2002; Whiteman et al. 1997) and relative (Andreas et al. 2000; Zhang et al. 2006) wind speed thresholds and falloff parameters (Bonner 1968; Sjostedt et al. 1990), or a combination of the above (Baas et al. 2009). Most literature has used the wind speed profile as the principal metric for LLJ determination. However, based on this approach, both the LLJ and DW regimes in this case study would satisfy criteria based solely on wind speed profiles. While the phrase “LLJ” may be literally true for DW events, the mechanisms driving these flows are significantly different from the classic notion of the Great Plains LLJ (Parish et al. 1988; Song et al. 2005; Whiteman et al. 1997), characterized by a moist southerly flow that can potentially be supergeostrophic following the inertial oscillation and brought on by a sudden vertical decoupling (Blackadar 1957; Holton 1967) over sloping terrain (Parish; Oolman 2010). Therefore, in this case study we define Mid-Atlantic LLJ as flowing parallel to the Appalachian Mountains with a southwesterly wind direction.

1.2.2 Mountain circulations

The second nocturnal regime observed at HUBC was a downslope flow. Many large mountain ranges around the world generate thermally-driven circulations. These have been the subject of numerous field campaigns (Banta et al. 2004; Bossert 1997; Schmidli et al. 2009). Periods of weak synoptic forcing often provide a favorable environment for development of these circulations (Banta et al. 2004; Pinto et al. 2006). Banta; Cotton (1981) examined summertime broad mountain basin thermal circulations in South Park, Colorado, and expanded the traditional notion of a simple two-way flow regime (daytime upslope and nocturnal downslope) to include a third afternoon regime. A study by Wolyn; McKee (1994) demonstrated the existence of a mountain-plains solenoid, in which circulation arose from thermal gradients between the dry Rocky Mountain slopes and the moist plains. The solenoidal circulation had several distinct phases, one of which included an intense down flow jet. Bossert; Cotton (1994) broadened the three-dimensional understanding of regional scale mountain flows linked to the diurnal cycle, and also identified a nocturnal density current. The properties of nocturnal drainage flows within deep valleys and their interaction with surface inversions were studied in Alberta, Canada (Sakiyama 1990). In Salt Lake City, an intense down-valley jet from nearby mountains also affected the basin cold pool, inversions, and the vertical mixing of the stable boundary layer below (Pinto et al. 2006), additionally affecting vertical motion through flow convergence measured by Doppler lidar (Banta et al. 2004) and analyzed in model simulations (Darby et al. 2006).

Recent advances in scientific computing have contributed to increasingly complex numerical weather prediction models which enable a more accurate representation of fine-scale meteorology that was previously too cumbersome to resolve. High resolution modeling has successfully simulated nocturnal downslope flows over the complex island terrains (Cuxart et al. 2007; Feng; Chen 2001) and intricate mountain-valley systems (Seaman et al. 2011; Zhong; Whiteman 2008). High resolution studies have also examined the behavior of nocturnal katabatic flows over idealized terrain examining different topography (Catalano; Cenedese 2010; O'Steen 2000; Trachte et al. 2010).

While previous studies have primarily focused on thermally-driven circulations that are observed on large mountains with steep terrain, such as the Rocky Mountains, there has been less research on orographically-driven circulations within regions with more gentle slopes and smaller mountain prominence. It is reasonable to believe that similar circulations can occur in regions with reduced topographic gradients. One such region is the Mid-Atlantic, situated between the Appalachian Mountains and the Atlantic Ocean. Wolyn; McKee (1994) showed a simulation using the half-barrier height of the Rocky Mountains still produced a mountain-plains solenoid, upslope winds, lee convergence zone, and a nocturnal jet, even though they were somewhat weaker. That experiment's half-barrier height is comparable to the elevation difference between the West Virginia Appalachian Mountains and Washington, DC, located just to the east. Idealized simulations have already indicated the presence of a solenoid east of the Appalachian Mountains, which may play a role in suppressing precipitation (Parker; Ahijevych 2007). Recent

research has found downslope flows over low-angle slopes are much stronger and deeper than previously believed (Whiteman; Zhong 2008). Another study underscored the development of thermal circulations with moderate wind speeds within Arizona's meteor crater (Lehner et al. 2010), which is a relatively small geographic feature compared to most mountains. The scope of this paper is to highlight the circulations and downslope winds which occurred in the Mid-Atlantic region in order to better understand their evolution and forcings.

1.2.3 Sea breezes

Sea breezes are phenomena that arise from the heating differential between land surfaces and water bodies during maximum daytime heating. The Mid-Atlantic region has large water bodies, such as the Chesapeake Bay and Atlantic Ocean, which are located adjacent to inland areas that can heat up very quickly in the summertime. Therefore, it is reasonable to assume these temperature differentials could influence low-level flows. Sea breezes are usually local in nature but can extend many kilometers inland (Simpson et al. 1977). They are thermally direct circulations that can occur nearby water bodies of any size, from oceans to large lakes (Keeler; Kristovich 2012; Keen; Lyons 1978), or even small lakes (Baker et al. 2001; Zumpfe; Horel 2007). The surface flow can come onshore as a front (Yoshikado 1990), multiple boundaries (Novak; Colle 2006), or simply a steadily increasing breeze. Onshore circulation depth vary greatly from shallow surface winds to deeper than 1 km (Darby et al. 2002). Sea breezes have been analyzed by Doppler lidars (Banta et al. 1993; Darby et al. 2002), spotted by radar (Atlas 1960; Meyer 1971), and observed

by sodar networks (Mastrantonio et al. 1994). Often these breezes can trigger precipitation (Baker et al. 2001) or even a rare tornadic event (Hidalgo et al. 2009).

The role of topography in governing sea breeze circulations is most pertinent to this case study. Early modeling analyzed the structure and evolution of two-dimensional circulations (Hong; Lin 1982; Mahrer; Pielke 1977) with various hypothetical terrain configurations. These studies indicated that the presence of terrain can significantly enhance a sea breeze circulation, which has been echoed by more recent work (Estoque 1981; Estoque; Gross 1981; Porson et al. 2007; Qian et al. 2011).

As mentioned in the previous sections, to our knowledge there has been very little published on the sea breeze effects in the Mid-Atlantic. However, a cursory review of radar archives and research data (Vermeesch et al. 2009) show these phenomena exist here.

1.3 Mountain Waves

In addition to thermally-driven downslope flows, significant downslope wind events can result from the hydraulics of mountain flows. DWs associated with mountain waves have been well documented in large mountain ranges around the world (Grisogono; Belušić 2009; Klemp; Lilly 1975; Koletsis et al. 2009; Nkemdirim 1986; Raphael 2003). Much of the previous research has focused on regions where damaging windstorms occur (Blier 1998; Brinkmann 1974; Meyers et al. 2003), which is usually correlated with steep terrain or high mountain profiles. However, mountains with lower elevations and gentler slopes, such as the Appalachians, have also demonstrated the capability of producing DWs (Decker; Robinson 2011; Gaffin

2009). Clearly, mountain flow hydraulics operate over the Appalachian Mountains, too. The research in this paper examines DWs from a different perspective. Here, the focus is not on high speed wind events, but rather the downstream effects of a reoccurring, mild DW over the central Appalachians that impacts Mid-Atlantic air quality and other regional circulations. A distinguishing characteristic of DWs in this case study is low-level flow that is perpendicular to the mountain ridges, similar to Colle; Mass (1998).

Several studies noted that DWs tended to occur in the late afternoon (Grubisic; Xiao 2006; Seluchi et al. 2003) or nighttime periods from 0000-0700 LST (Brinkmann 1974). A quasi-regular timing of DW events suggests a possible linkage to the diurnal cycle. Ying; Baopu (1993) argued that the classic theory of mountain flows does not consider the thermal-forcing or turbulence produced by the PBL, but that it may play a key role in governing the dynamics of mountain flows. To address this question, there have been several recent studies with a renewed interest in understanding the affect of the PBL on leeside mountain flows. It has been demonstrated that the boundary layer can affect mountain wave amplitude (Ólafsson; Bougeault 1997; Peng; Thompson 2003) through absorption (Jiang et al. 2006) or reflection (Lott 2007). An idealized study by Smith; Skillingstad (2009) examined the affect of weak, strong, and negative surface heat fluxes on mountain flows. Of particular interest was the finding that strong surface heating (daytime conditions) can significantly weakened DW flows, while surface cooling (nighttime conditions) can enhanced the downslope jet and lee rotors. In a subsequent study, Smith; Skillingstad (2011) showed the height of temperature inversions, located at the PBL top, can

significantly alter the spatial extent and intensity of the downslope jet. Smith; Skyllingstad (2011) also investigated the katabatic contribution of DW flow experiments and found that surface cooling and a low inversion height significantly increased flow velocity in areas far downstream. Therefore, it is likely that DW flows have both a katabatic and hydraulic component which may be governed by diurnal evolution of the PBL and temperature inversions. Typical Mid-Atlantic summertime conditions which are characterized by weak synoptic forcing, strong solar heating, and high pressure subsidence, which can lead to a stratified atmosphere with multiple temperature inversions, may create an ideal environment for Appalachian Mountain DW events.

1.4 Nocturnal PBL

Measurements discussed in Chapter 2 will show that the LLJ and DW flows significantly modified the structure of the nocturnal PBL. Determining the structure and evolution of a nocturnal PBL and its respective top (PBLT) remains an active area of research and a continued challenge for both modelers and observationalists alike. Generally, the daytime PBL is characterized by convective mixing which produces a more defined PBLT compared to nocturnal periods. On the other hand, the nighttime PBL tends to be more stratified with multiple temperature inversions that can lead to areas with seemingly sporadic mixing in an atmosphere which contains particulates with various settling rates. Therefore, the dichotomous appearance of PBLTs in the lower atmosphere, at this time, implies that using any single observation field (ie. temperature, water vapor, aerosols, wind, etc) for determination

of the PBLT could be misleading. This greatly complicates an accurate determination of the nocturnal PBLT.

There has been much discussion regarding an appropriate determination of the nocturnal PBLT (Arya 1981; Garratt 1982; Mahrt; Heald 1979; Stull 1983; Vickers; Mahrt 2004; Yamada 1979; Yu 1978) or the PBL structure (Bader; McKee 1992; Clarke 1969; Krishna et al. 2003; Kumar et al. 2012; Mahrt 1998; Seaman et al. 2011). Further variability among nocturnal PBLs can be introduced by synoptic conditions (Estournel; Guedalia 1985; Gopalakrishnan et al. 1998; Krishna et al. 2003), terrain (Bader; McKee 1992; Kumar et al. 2012; Seaman et al. 2011), or local environment (Godowitch et al. 1985; Martilli 2002). Some authors have suggested defining the PBLT as the maximum height affected by the turbulent transfer of heat or mass from the Earth's surface (Arya 1981). Yamada (1979) defined the PBLT as "the maximum vertical extent at which surface effects are still perceived." The two preceding definitions are somewhat subjective, but will be adapted for this case study in the observational and modeling discussions of nocturnal PBLT.

1.5 Research Objectives

In Chapter 2 we present field observations from the Baltimore-Washington region during a case study from 1-5 August 2006. The objectives of Chapter 2 are to (a) describe the synoptic setting of this case study to establish context for understanding the observations; (b) present the WAVES observations acquired at HUBC, which include vertical profiles of the lower atmosphere, surface observations, and soundings; (c) then examine regional observations for consistency and new information. The objectives of the discussion are to (d) demonstrate the presence of

two distinct nocturnal low-level flows that could be misconstrued as a single LLJ; (e) explore their impact of significantly modifying the profile of the lowest two kilometers of the atmosphere; and (f) summarize the pronounced diurnal cycle revealed from observations, which is contrasted with the traditional notion of diurnal PBL evolution.

High resolution simulations of the case study are presented in Chapter 3. The main objectives were to (g) show the model shortcomings in reproducing WAVES observation profiles; (h) determine the origin and evolution of the LLJ and DW events; (i) analyze the structure of these nocturnal features; and (j) highlight basic mechanisms behind the low-level flows patterns.

In Chapter 4, several model sensitivity tests were conducted prior to the high resolution simulations that are presented in Chapter 3. The overarching objective of this Chapter 4 is to (k) ascertain model uncertainty in four areas believed to be most influential on the simulation accuracy of this case study: (1) initial condition sources; (2) cumulus parameterizations; (3) PBL parameterizations; and (4) simulation differences among runs that used staggered initialization times. Another objective was to (h) comprehensively verify sensitivity tests using observations from: (1) WAVES measurements; (2) upper air data from aircraft and soundings; (3) surface observations from a large ground-based network; and (4) precipitation data generated from radar and ground measurements.

An overall summary of this research is presented in Chapter 5, which emphasizes the major findings. Possible areas of future research are also mentioned.

Chapter 2: Observational Detection of Fine Scale Phenomena

2.1 Synoptic Overview

During the first week of August 2006, a frontal boundary progressed from the upper Great Plains through the Northeast. In the Mid-Atlantic region, operational numerical weather prediction models had difficulty correctly forecasting precipitation totals and the timing of the frontal passage ahead of this weak cold front. Most forecasts indicated an earlier arrival than actually occurred, and for there to be more convective activity associated with the frontal passage. Although the boundary was marked by a well-defined line of precipitation in the Midwest, the convective activity diminished and became less organized as the front approached the Appalachian Mountains. The cold front made a dry passage through HUBC at 2100 UTC 4 August, bringing in slightly cooler postfrontal air and a significant drop in humidity.

2.1.1 Steering level charts

The major upper level synoptic features governing the weather pattern that extended across the eastern half of the US were low pressure centers in Canada and a quasi-stationary ridge of high pressure that was located over the Southeastern US. Figure 2.1 shows the North American Regional Reanalysis (NARR) 500 mb geopotential heights and temperature, along with surface boundaries provided by the Unisys Weather (<http://weather.unisys.com/>) analyses for the first 6 days of August, at 0000 UTC (or 1900 LDT) each day. The overall meteorological pattern showed a high pressure ridge (H1, H2) that was eroded by eastward propagating troughs which moved across the northern tier of the US. Over the course of several days, this

processes deformed the high pressure region and resulted in a more zonal orientation of the jet stream axis. At 0000 UTC 1 August (Figure 2.1a) there were three low pressure centers in Canada: near the Gulf of Alaska (L4), in the lee of the Rockies (L1), and over the Labrador Sea (L0). The ridge of high pressure in the southeast US was made up of two high pressure centers (H1, H2), which advected warm moist air up from the Gulf of Mexico into the Midwest. A surface cold front associated with L1 stretched from southeastern Colorado to the triple point in Minnesota, and from there a warm front extended eastward toward Vermont and was reinforced by an anticyclonic circulation about H1. Another surface cold front associated with L0 was located north of Maine. Although no frontal boundaries were present near HUBC at this time, the Unisys analysis consistently placed a trough in the lee of the Appalachians throughout the first four days of August. This trough is later hypothesized to be an indicator of a DW regime. At the beginning of 2 August (Figure 2.1b), L1 became elongated with two smaller low pressure centers labeled L2 and L3, respectively. The reduced geopotential gradient between the low pressure centers and H1 slowed the frontal progression through the upper-Midwest, and gave rise to a single continuous boundary from Colorado northeast to L3. The purple line superimposed in Figure 2.1b designates the overall trough axis orientation formed by the juxtaposition of L3 and L0. L3 merged with the larger L0 by 0000 UTC 3 August (Figure 2.1c), which deepened the trough axis and allowed it to extend further out toward L2. At this time the leading surface cold front had virtually stalled, while a second reinforcing cold front associated with L2 developed behind it. Figure 2.1d shows that by the start of 4 August L2 had also merged with L0, promoting the

continued deepening of the trough axis which was rotating counterclockwise about L0 and facilitating the frontogenesis of the second cold front. The rotation of the trough axis drove the second cold front forward and propelled the leading cold front further to the southeast, displacing H1 off the North Carolina coast. Figure 2.1e shows that at 0000 UTC 5 August the leading cold front had just passed through HUBC. By 6 August (Figure 2.1f), the trough axis associated with L0 was oriented toward the southeast allowing cooler Canadian air to infiltrate the Mid-Atlantic and continue pushing southward.

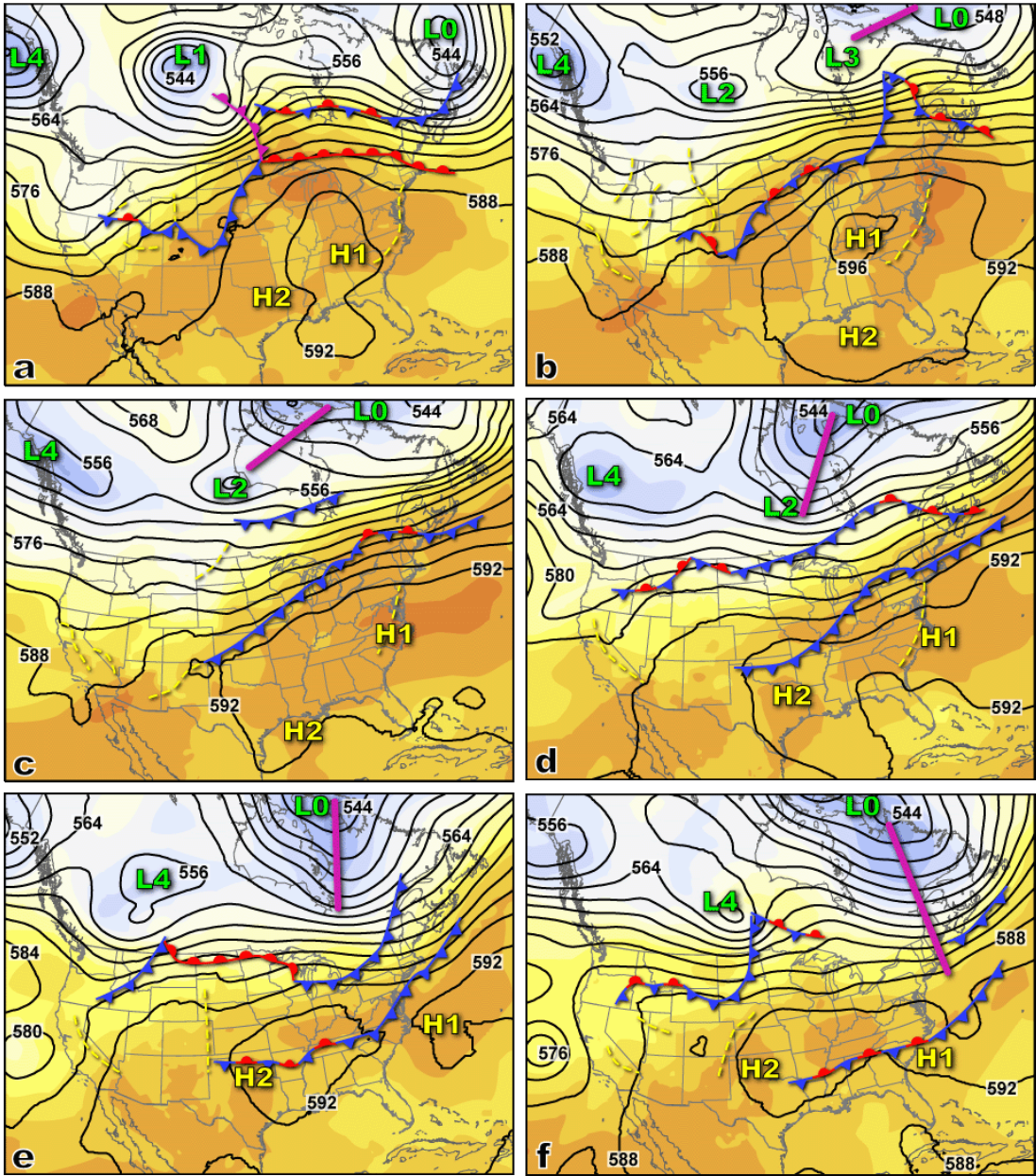


Figure 2.1: Six day sequence of NARR reanalysis showing 500 mb temperature (shading) and geopotential height (contours). Frontal boundaries and troughs from Unisys surface analysis are superimposed. The purple line identifies a trough rotating around L0. Reanalysis times are (a) 0000 UTC 1 Aug, (b) 0000 UTC 2 Aug, (c) 0000 UTC 3 Aug, (d) 0000 UTC 4 Aug, (e) 0000 UTC 5 Aug, (f) 0000 UTC 6 Aug.

2.1.2 Surface charts

The two most influential synoptic events which occurred at HUBC during this case study were the passages of a prefrontal trough and the cold front. The prefrontal trough propagated ahead of the cold front exhibiting a minimum in surface pressure, a wind shift, and other characteristics that were similar to the discussion of prefrontal troughs by Schultz (2005). Both the prefrontal trough and cold front events marked a transition between air masses which affected HUBC measurements. Figure 2.2 illustrates the evolution of the regional meteorology during this period. The yellow dashed line denotes the position of the prefrontal trough. The frontal boundary (Figure 2.2) was identified by a sharp gradient in the 950 mb temperature field (not shown), and its location was consistent with the frontal position in the Unisys Weather surface analysis plots.

Although precipitation was forecasted for HUBC, it remained rain-free for the entire 5-day period. All regional convective activity remained confined between the cold front and the prefrontal trough. At 1900 UTC 3 August (Figure 2.2a), the most intense convective storms (A,B,C) were located 300-400 km ahead of the cold front, while a region of less convective precipitation (D) was located along the cold front in the vicinity of the surface low pressure. By 2300 UTC (Figure 2.2b) the convective cells advected further east with areas A and B merging into a broader area of precipitation, while new convective precipitation (E) appeared over the Ohio River Valley. At this point it appeared as though HUBC would receive rainfall from storms that were merely 250 km upstream. However, by 0400 UTC 4 August (Figure 2.2c) the convective activity associated with region A-B had rapidly decayed after

orthogonally traversing the backbone of the Appalachian Mountains. By contrast, regions D and E circumnavigated the steep topography and slightly intensified. By 0900 UTC (Figure 2.2d) all nocturnal convective activity was diminished by the increased atmospheric stability. Convective area E also decayed upon encountering higher terrain, but precipitation around D continued through the unstable region created by the frontal boundary. The advancing surface cold front was still located approximately 350 km northwest of HUBC at 0900 UTC 4 August. At 2100 UTC 4 August (Figure 2.2e), the surface cold front was located immediately north of HUBC. By 0000 UTC 5 August (Figure 2.2f), the cold front had passed over HUBC and was moving south. The frontal progression west of the Appalachian Mountains stalled in the high elevations and rough terrain. To the east of the mountains, the surface cold front quickly propagated down the Mid-Atlantic.

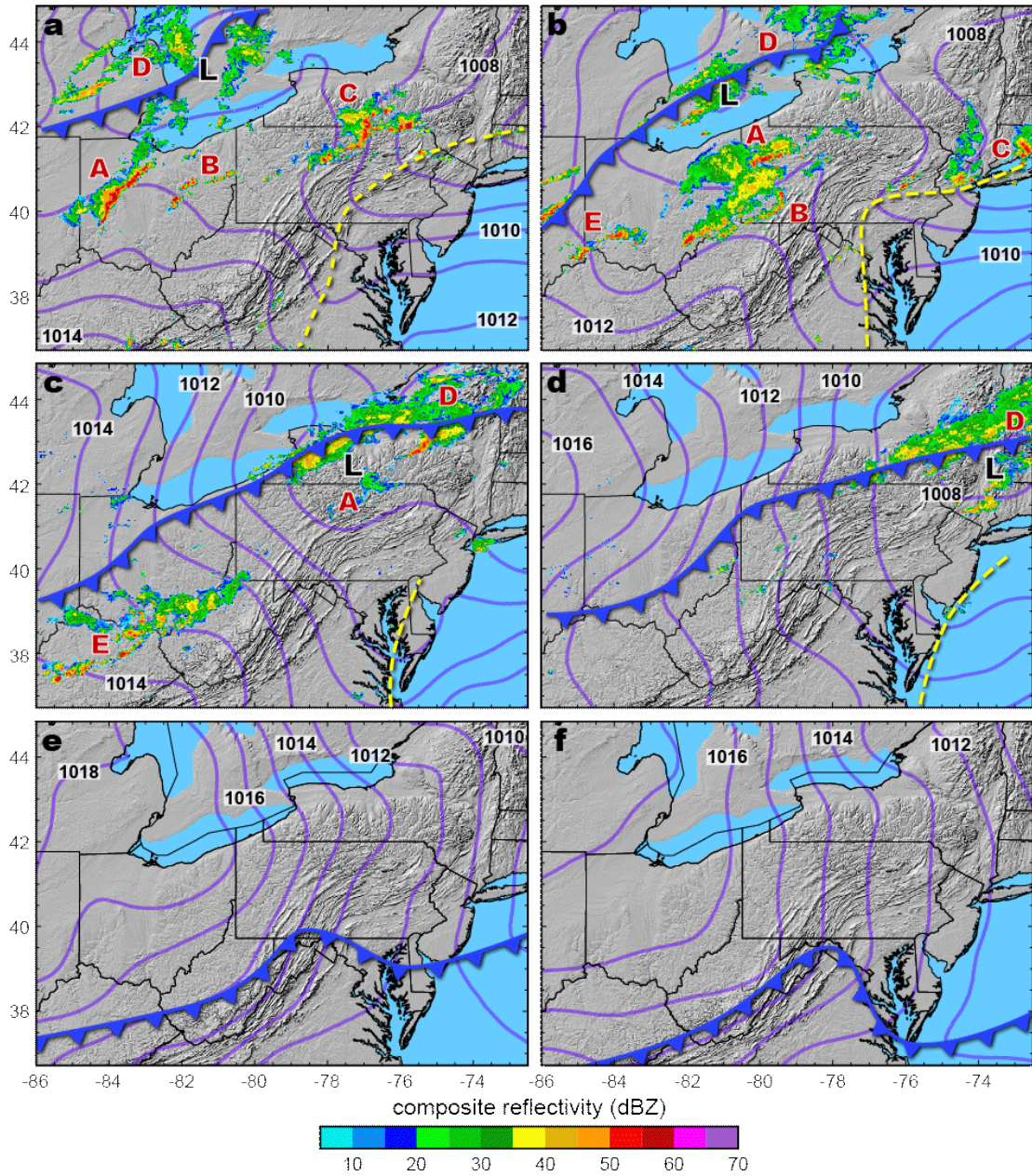


Figure 2.2: Nexrad composite radar reflectivity (dBZ) and RUC sea level pressure contours (hPa) are overlaid on shaded relief at times (a) 1900 UTC 3 Aug, (b) 2300 UTC 3 Aug, (c) 0400 UTC 4 Aug, (d) 0900 UTC 4 Aug, (e) 2100 UTC 4 Aug, and (f) 0000 UTC 5 Aug. The surface cold front (blue line) and prefrontal trough (yellow dashed line) are drawn based on analysis of RUC 950 mb fields.

2.2 Analysis of Diurnal Variations

2.2.1 WAVES profiling

A continuous PBL profile time series for 1-5 August is presented in Figure 2.3, showing the overall low-level meteorology at HUBC during this case study. A pronounced diurnal cycle was revealed in the data. Regions marked with "J" correspond to a LLJ wind regime and regions labeled with "D" correspond to a DW regime. The surface cold frontal passage is marked by "F" around 2200 UTC 4 August, at which time there was a large drop in WVMR (Figure 2.3a) and ASR (Figure 2.3b) values. An uptick in wind speed was evident and was followed by prevailing northeasterly winds.

The DW and LLJ regimes could be identified by their unique characteristics. The DW flow corresponded to a significant reduction in the ASR values. There was a slight reduction in WVMR, most evident between 0.8-2.5 km AGL, indicating that the DWs likely carried slightly drier air than was at HUBC. The winds below 1.5 km AGL were notably northwesterly (purple shading, Figure 2.3d) and corresponded to a wind speed maximum (Figure 2.3c). The LLJ regime was also identified by a sub-kilometer wind speed maximum, but with a west-southwesterly direction. The ASR values typically decreased during the LLJ regime, perhaps most notably during the nights of 1-2 August. The LLJ regime was also correlated with a slight increase in WVMR field.

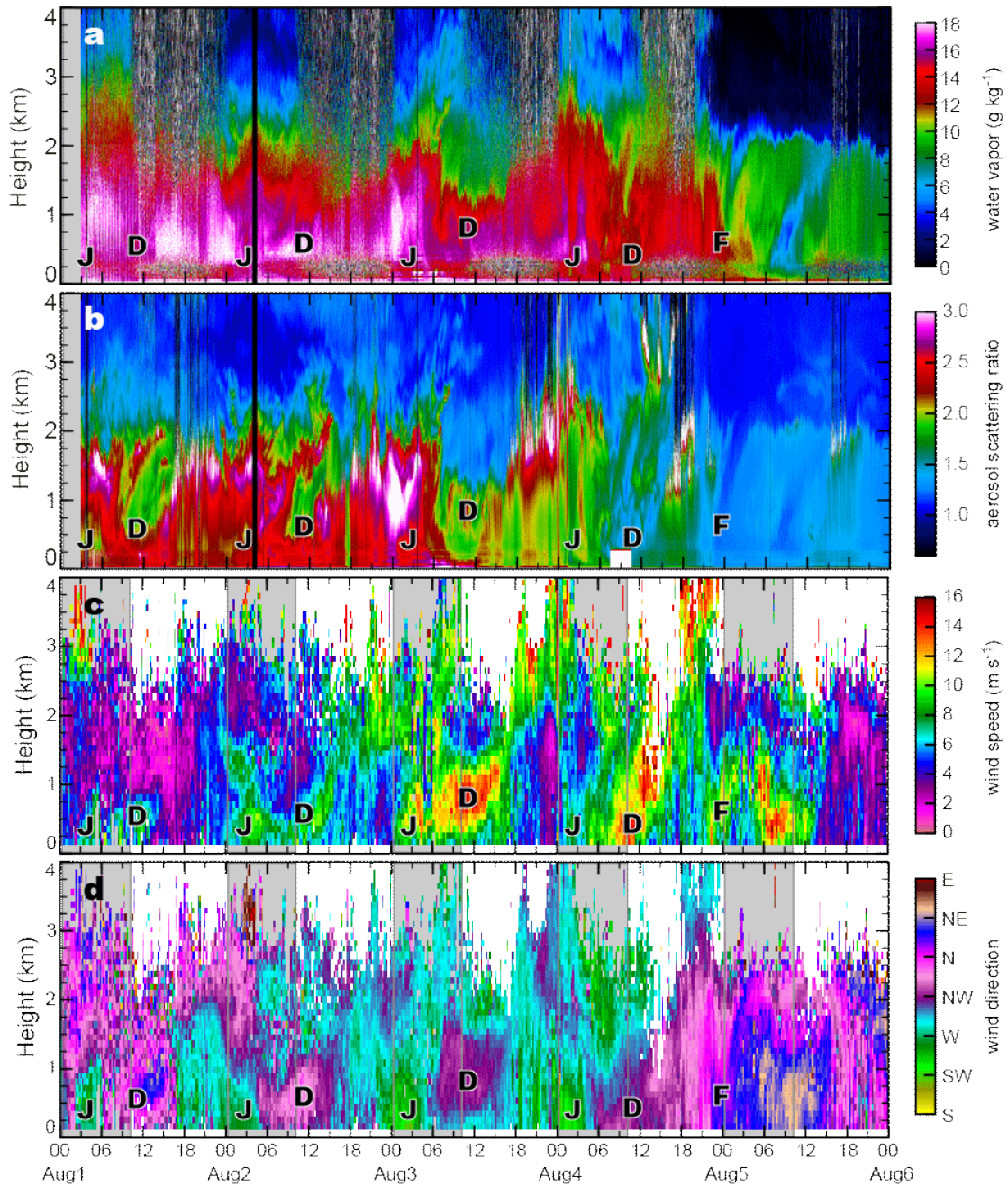


Figure 2.3: HUBC 4 km AGL time series from 0000 UTC 1 August to 0000 UTC 6 Aug. Panels show (a) SRL water vapor mixing ratio, (b) SRL aerosol scattering ratio, (c) MDE wind speed, and (d) direction. Gray shaded background indicates nighttime periods. "J", "D", and "F" designate low-level jet, downslope winds, and cold front events.

August 1-4 showed a diurnal signature that became progressively more apparent with time. This was particularly apparent in nocturnal low-level wind speed which consistently increased with each subsequent DW regime. This is consistent with the general expectations of stronger gradients and an amplified thermal wind ahead of a cold front.

The backdrop for 1-4 August was a predominantly northwesterly background flow (magenta-purple hues) due to the anticyclonic circulation about H1 (Figure 2.1). A separate shallow layer of west-southwesterly flow (green-cyan hues) was also present during this time. This layer became increasingly expansive as the frontal passage approached, which is consistent with the typical surge of southwesterly prefrontal air. However, fine-scale observations indicated more complicated sub-kilometer dynamics existed between the two airflow directions associated with the DW and LLJ. The layer of west-southwesterly flow remained confined to the lower atmosphere but underwent periodic lifting and descent each day. The morning periods (1000-1700 UTC) associated with the diurnal cycles seen during 1-3 August possessed ambient northwesterly flow in the lowest 1.5 km. During the afternoon (1700-2200 UTC) the convective boundary layer (CBL) transitioned to a calm west-southwesterly wind and then intensified into a LLJ regime after nightfall (0000-0600 UTC). Approximately halfway through the night, between 0600-0700 UTC, the DW regime displaced the lowest 1.5 km and lifted the layer of southwesterly flow for the remainder of the night and into the daylight hours. In the wake of the DW regime, a northwesterly wind exceeding 10 m s^{-1} occupied the lowest kilometer of the atmosphere. After dawn, it is hypothesized that surface heating led to the growth of

the CBL which weakened the DW flow. The eddy viscosity associated with the rising thermals increased and would likely impede the strong low-level laminar DW flow. The result was a CBL that was characterized by calm winds that veered southwesterly as the afternoon progressed.

2.2.2 WAVES surface observations

Several surface observations were also acquired at HUBC for the 5-day period (Figure 2.4). Precipitable water vapor (PW) and air quality measurements were collected at a height of approximately 7 m AGL. Other measurements were collected at various heights along a 31 m instrument tower. The details in many of the measurements in Figure 2.4 show similarity from day-to-day, indicative of the repetitive diurnal cycle under discussion.

Air quality measurements were collected from PSU's Nittany Atmospheric Trailer and Integrated Validation Experiment (NATIVE, <http://ozone.met.psu.edu/Native/index.html>) and MDE analyzers as shown in Figure 2.4a. The NATIVE system was at HUBC through 3 August. MDE data were used to extend certain measurements provided by the NATIVE system beyond this date. NATIVE data provided additional measurements of carbon monoxide (CO) and sulfur dioxide (SO₂) gases, while MDE complemented the observation dataset through sampling particulate matter with a diameter of 2.5 micron or less (PM_{2.5}). MDE and NATIVE both collected data for nitrogen oxides. However, the MDE system collected NO_x, which is predominantly composed of nitrogen oxide (NO) and dioxide (NO₂), whereas NATIVE collected NO_y, a superset including NO_x plus organic and inorganic nitrates and nitric acid (HNO₃). Although NO_y and NO_x

measurements are generally similar, NO_y data usually have higher levels accounting for a wider range of species. Both platforms measured ozone (O₃). All NATIVE data had temporal resolution of less than 1 minute while the MDE data were available in hourly samples.

Air quality measurements collected at HUBC show consistently high values for O₃ and PM_{2.5} during the first three days of August, peaking on 2 August. Daily peak concentrations of O₃ and PM_{2.5} were considerably lower on 4-5 August, after the passage of the prefrontal trough and cold front. Shortwave radiation measurements (not shown) tracked closely with the trend in prefrontal daytime O₃ concentrations, correlating the highest levels with clear skies and the lowest to cloudier conditions. Surface temperatures were slightly warmer on 3 August, but O₃ levels were slightly lower. This is partly due to lower concentrations of O₃ present at daybreak on 3 August, and also because of more afternoon cloudiness.

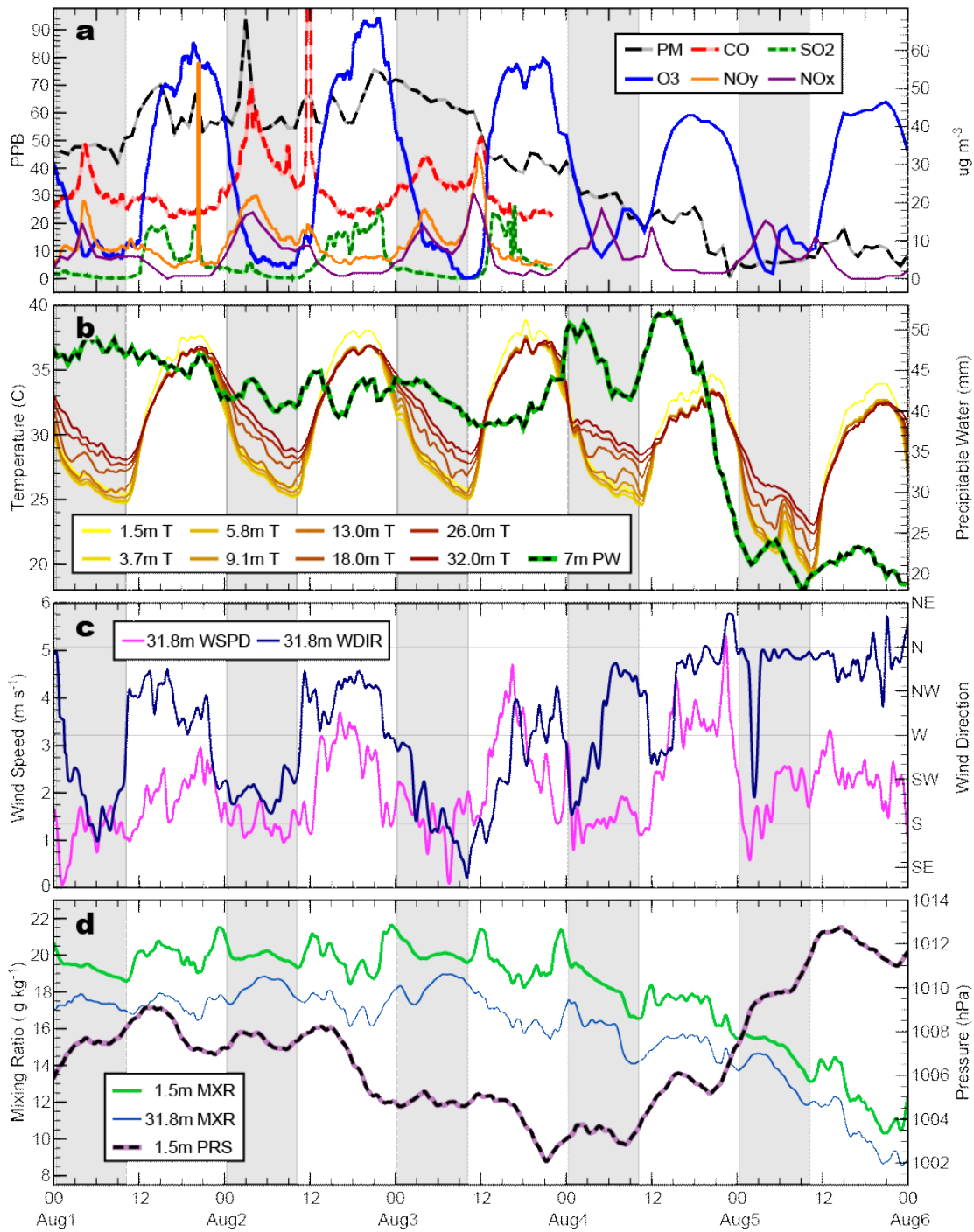


Figure 2.4: Surface observations collected at HUBC from 0000 UTC 1 August to 0000 UTC 6 Aug. Panel (a) shows air quality measurements. PM units are $\mu\text{g m}^{-3}$. O_3 , SO_2 , NO_y , NO_x have units of ppb. CO is ppb/10. Panel (b) shows precipitable water vapor and temperature from the 31 m meteorological tower. Panel (c) shows wind speed and direction at the tower top. Panel (d) shows surface pressure and mixing ratio at the tower base and top. Gray shaded background indicates nighttime periods.

In urban regions, such as the Baltimore-Washington metro area, a significant source of nitrogen oxides is the burning of fossil fuels. The 1-3 August (Tuesday-Thursday) data show a spike each day around 1200 UTC, which corresponds with the morning rush hour. NO_x/y levels reach a minimum during the daytime from photolysis, but increase again toward nightfall. This is related to the titration of ozone and concentration levels produced by the vertical stretching (contraction) of the PBL during the daytime (nighttime). Each night around 0400 UTC there is a prominent spike in nitrogen oxides. Considering that HUBC was downwind of industrial parts of northeast Washington, DC at that time, this spike might also be related to the advection and convergence of pollutant laden air between the DW and LLJ regimes. It is clear that a reduction in NO_x/y occurred after the DW passage. Outside the diurnal pattern, the overall trend of nitrogen oxide concentrations remained relatively consistent throughout the five-day period and appeared minimally affected by the frontal passage. In general, the NO_x and NO_y curves closely agreed, with NO_y exhibiting slightly higher concentrations with larger spikes.

CO concentrations followed a trend similar to that of nitrogen oxides. Data spikes occurred at the same times, midway through the nocturnal period and during the morning rush hours. Generally the concentration was higher during the nighttime hours and the lowest in the afternoon. Sulfur dioxide showed a pattern opposite of CO, trending high during the daytime and lower at night. It is likely that daytime mixing through the CBL tapped into non-local pollutants aloft, which had advected from elsewhere. Regional power plants are a major contributor of SO₂ emissions found in the Mid-Atlantic during this time of year. Back trajectories indicated these

sources were located along the Ohio River Valley. During late afternoon, the SO₂ levels dropped significantly with the decay of the CBL followed by dry deposition processes.

A more thorough investigation of regional air quality during this case study would be beneficial and likely the subject of future research. However, an in-depth analysis of the complex relationships between the pollutants and the meteorology is beyond the scope of this paper.

Meteorological surface observations also showed a strong diurnal cycle. The daytime mixing of the CBL resulted in small temperature deviations throughout the depth of the 31 m tower (Figure 2.4b). Conversely, nocturnal radiational cooling produced stratification which created large temperature differences of up to 5° C between the ground and the top of the tower.

Mixing ratio data (Figure 2.4d) acquired at top and bottom of the tower showed similar variation of features although the values at the ground were approximately 2 g kg⁻¹ higher on average. The mixing ratio data vacillated about 18 and 20 g kg⁻¹, for the tower top and base measurements, respectively, until 4 August. After that time, the mixing ratio steadily decreased and reached a mean value of approximately 9-11 g kg⁻¹ by 2100 UTC 5 August when the post-frontal air mass dominated HUBC. As mentioned, the mixing ratio curves show similar features from day-to-day. For example, in the 2-3 hours prior to sunset the mixing ratio spiked by 2 g kg⁻¹. The mixing ratio trend throughout the nocturnal period was generally decreasing. However, sudden transitions in the data curves were observed each night coincident with the DW events. Mixing ratio values were typically higher during the

late morning than early afternoon. Mixing ratio values appeared to have an inverse relationship with wind speed (Figure 2.4c). Higher wind speeds often facilitate increased vertical mixing through turbulence and advect moisture away from the surface more quickly. On the other hand, calmer winds can allow surface moisture to accumulate and moisten low-level air. Therefore, the surface fluctuations in mixing ratio are not necessarily reflected in the lidar profile for a couple of reasons. First, the overlap correction function for the lidar field of view limited SRL's ability to resolve features in the water vapor field within the lowest 200 m. Secondly, surface moisture fluxes are diffused by convective eddies and may not be as clear above 200 m. This is demonstrated by the difference in mixing ratio measurements between the 31 m tower top and base. However, notwithstanding the above limitations between constituents measured at the surface versus aloft, the increase in surface mixing ratio during the evening periods also appeared in the lidar profile as well. This is most evident on 2 August below 1.5 km, but can be discerned on other days.

High-resolution surface wind data (Figure 2.4c) were sampled at the top of the tower by sonic anemometers. Wind speeds were strongest during daytime hours with increasing magnitude each day ahead of the cold front, exceeding 5 m s^{-1} on the afternoon of 4 August. Nocturnal winds were generally calm around 1.5 m s^{-1} . In general, the strongest (weakest) wind speed coincided with the warmest (coldest) surface temperature, which was similar to the findings mentioned in (Zhang; Zheng 2004). Postfrontal wind speeds on 5 August were on average about 2.5 m s^{-1} for daytime and nighttime periods. The daytime direction was usually northwesterly for 1-3 August, although the wind direction was slower to transition to this quadrant on 3

August. The nocturnal wind direction during this time was mostly south-southwest, but rotated even further on 3 August gaining an easterly component. The prefrontal trough influenced the weather of 4 August, which we characterized as a transition day between the pre-trough and postfrontal environments. The nocturnal wind direction was briefly southwest during the LLJ regime on this day, then became northwesterly until late afternoon. After the passage of the cold front, the wind direction became predominantly northerly. It is curious to note the dramatic wind shifts that occur near dawn. The wind shift was an abrupt change from the southwestern to the northwestern on 1-2 August, a more gradual transition on 3 August, and a sharp change from the northwest to southwest quadrant on 4 August. It is hypothesized these abrupt transitions in surface winds could result from a momentum synchronization between higher wind speeds aloft and a more calm shallow nocturnal surface layer dissolving quickly after dawn. Unfortunately, there is a vertical gap in wind observation data between the 31 m tower top and the lowest level of the wind profiler near 175 m. Sonde data indicated the depth of the nocturnal surface layer was approximately 100 m, so the breakdown of this shallow surface layer after dawn would not be captured by WAVES instrumentation. A similar phenomenon occurred over a 3-h period prior to sunset on 1-3 August, when wind speeds rapidly decreased and transitioned from northwesterly to southwesterly. This time period was correlated with the previously mentioned increase in mixing ratio. Upon close examination, there were subtle perturbations in wind speed and direction coincident with the arrival of the LLJ and DW air flows. However, these perturbations appeared relatively muted in comparison with the expectation of a larger impact on the wind field transitioning

between the LLJ and DW regimes. It is likely that atmospheric stability created a layered environment, particularly at low-levels such as a nocturnal surface layer, which mitigated the depth of turbulent eddies, thereby insulating the lowest layers from any significant downward transport of horizontal momentum. This implies the existence of a possible time lag between events aloft and their effect near the surface.

The surface pressure throughout this period is shown in Figure 2.4d. From 1 to 3 August the overall pressure trend was negative, reaching a 5-day minimum of 1002 hPa at 2100 UTC 3 August, coincident with the passage of the prefrontal trough. Thereafter, it increased slightly to 1006 hPa by the time of the frontal passage. Afterward, the surface pressure rose rapidly to over 1012 hPa by 1200 UTC 5 August. The timing of the overall pressure minimum, which was roughly 24 h prior to the cold front arrival, is further justification for classifying this period as a prefrontal trough. Overriding the pressure tendency was the signature of a daily diurnal tide (Whiteman; Bian 1996). Every night there was a local maximum pressure around 0400 UTC and a minimum pressure near 0700 UTC. Similarly, the local daytime maximum and minimum occurred near 1500 and 2100 UTC, respectively. However, it is unclear whether the coincidence of these pressure inflections were more broadly linked to either the LLJ, DW, or the observed surface wind shifts near dawn and dusk.

Total column PW decreased slightly over the period of 1-3 August, ranging from 45 to 40 mm (Figure 2.4b). The beginning of 4 August was characterized by a push of moisture immediately ahead of the cold front. This time corresponded to the convective period showed in Figure 2.2c-d. The first push of moisture from 0000-0300 UTC 4 August was associated with the northward transport of post-convective

moisture from the Carolinas and Southwestern Virginia. Upper-level winds in addition to the LLJ had a role in transporting this moisture. A second maximum in PW occurred around 1200-1500 UTC 4 August and was associated with moisture convergence immediately ahead of the frontal boundary. Throughout the evening of 4 August and into the nocturnal hours of 5 August, the PW decreased sharply by more than 30 mm due to the passage of the frontal boundary. However, there was a small increase in PW from 0200-0900 UTC 5 August. This increase was related to the two-prong passage of the surface cold front (Figure 2.2f). First, the cold front dipped past HUBC from the northeast and then the western frontal boundary folded over the Appalachian Mountains with reinforcing air. It is hypothesized that moisture convergence led to the PW increase during this time. August 5 was notably drier than the preceding days. Additionally, the nights of 2-3 August showed an increase (decrease) in PW during the time of the LLJ (DW). Therefore it is believed that the LLJ and DW were responsible for moist and dry transport in the lower atmosphere, respectively.

2.2.3 WAVES soundings

In addition to surface observations and lower atmosphere profiling, nine radiosondes were launched during this case study. The launches usually occurred twice daily around 0600-0700 UTC and 1700-1800 UTC timed according to satellite overpasses. However, there were no soundings from high-quality sensors on 2 August. An additional sonde was launched at 2313 UTC 4 August to coincide with the anticipated frontal passage. During these 5 days the upper atmosphere was mostly stable and contained many inversion layers. For example, on 3 August more than 10

inversion layers were observed below 10 km. The generally stable atmospheric conditions were due to the high pressure over the Southeast and Mid-Atlantic regions. Mixing ratio and wind speed profiles between atmospheric layers were relatively uniform, but showed sharp discontinuities in transition zones between layers. This gave profiles of either water vapor mixing ratio or temperature a step-like appearance. HUBC radiosonde temperature profiles indicated the lowest 2 km were nocturnally stable and neutral during the daytime for this period.

2.2.4 Regional wind profilers

The nearest wind profilers along the US East Coast (Figure 2.5) were examined to determine whether nocturnal phenomena similar to those uncovered by WAVES observations were occurring at other locations. Although the Rutgers site is located near mountainous terrain, most elevations are relatively low. In general, the Appalachian Mountain elevation increases from New Jersey (~350 m) southward to North Carolina (~1400 m). The Fall Line (between regions 6 to 7 in Figure 2.5) is an important meteorological barrier and often channels or limits the westward extent of LLJs even though it has a relatively small elevation drop. The Rutgers, HUBC, and Raleigh sites are all located near the Fall Line, whereas the Charlotte site is located to the west of the Fall Line, well into the Piedmont region.

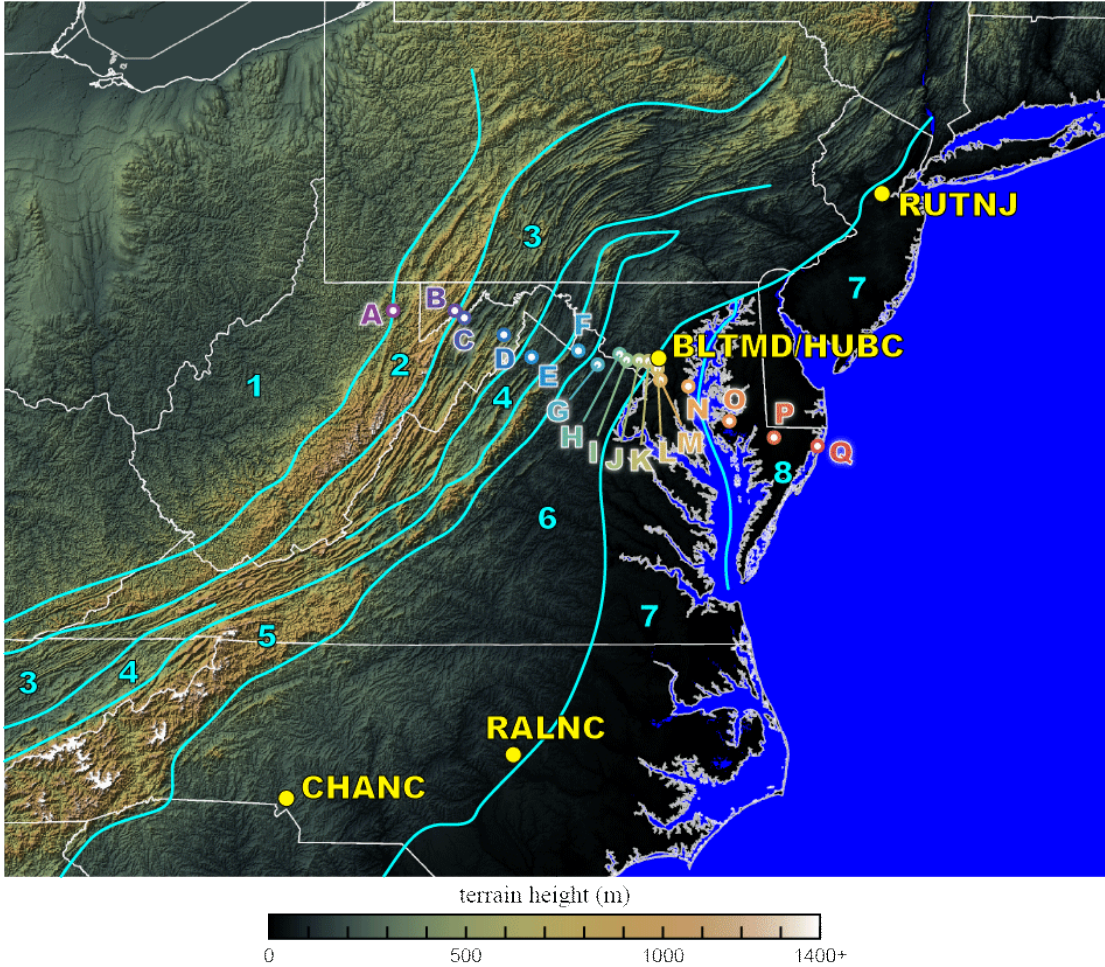


Figure 2.5: The Mid-Atlantic is a complex region with of seven distinct regional geographies: (1) Western Upslope, (2) Appalachian Mountain Highlands, (3) Ridge and Valley, (4) Great Valley, (5) Blue Ridge Mountains, (6) Piedmont Plateau, and the (7) Coastal Plains regions. The Coastal Plains are further subdivided into the Western and Eastern Shores to the west and east of the Chesapeake Bay, respectively. Locations A-Z were WeatherBug sites selected to observe surface winds. The nearest operational wind profilers during this case study are labeled in yellow. The distance between the profiler sites and the Appalachian Mountains was approximately 30, 75, 125, and 190 km for RUTNJ, BLTMD, CHANC, and RALNC, respectively.

Figure 2.6 shows compares the wind direction between the four wind profiler sites. HUBC data showed the clearest depiction of the LLJ and DW nocturnal features. The broad areas of southwesterly flow among the non-HUBC sites make it difficult to discern the extent of any LLJ regimes that may have been present. Therefore, the following discussion will focus on the more clearly defined DW

features that were detectable at all four sites, although their structures appear different from site to site. The nocturnal events observed at HUBC were shallower than at the other sites, being confined to less than 1.5 km AGL. The Rutgers DW regime on 2-3 August had a similar timing to that of HUBC (Figure 2.6a). However, it appeared at approximately 500 m above the ground as opposed to near the surface at HUBC. In Raleigh (Figure 2.6c) and Charlotte (Figure 2.6d) the DW arrival was later and closer to dawn. The 4-5 hour lag is hypothesized to be partially the result of increased travel time from the mountain region, assuming DW propagation speeds were somewhat similar. However, it is impossible to determine with certainty, from this dataset alone, the relative propagation speeds of the DW events at each site. DW events were less defined in the North Carolina sites, which could be the result of air mass moderation traveling the greater distance from the mountain regions. The DW arrival in the northern sites appeared more bore-like and was confined under 2 km AGL. In the North Carolina sites the DW arrival was more disorganized with a front-like appearance, showing a slight vertical slant through a deeper layer. The difference in appearance may be indicative of weaker DWs in the south.

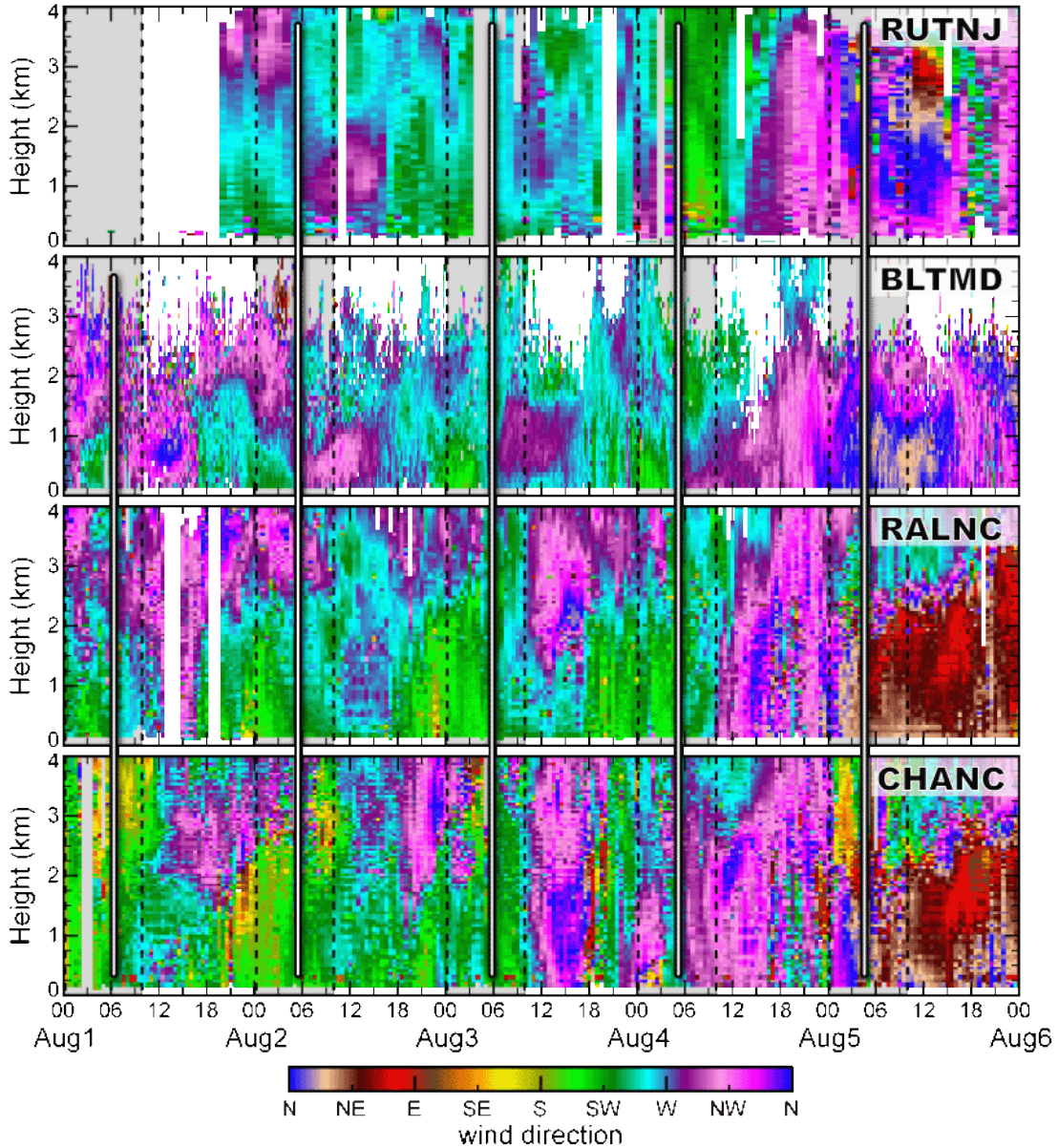


Figure 2.6: Comparison of wind direction between profilers at (a) Rutgers, NJ, (b) Beltsville, MD, (c) Raleigh, NC, and (d) Charlotte, NC from 0000 UTC 1 August to 0000 UTC 6 Aug. These locations are marked in Figure 2.5. White lines mark the beginning of the DW regime at HUBC. Gray shaded background indicates nighttime periods.

Figure 2.7 compares the wind speed among the four sites. In general, winds were stronger at sites further north. This was expected considering the calm conditions that existed under H1 (Figure 2.1), while stronger gradients in the vicinity of the frontal boundary led to more windiness further north. During 2-3 August, the

Rutgers data (Figure 2.7a) showed strong continuous winds below 2 km with little respite in the wind speed between with the LLJ and DW events. Furthermore, the LLJ and DW wind magnitudes were comparable, unlike the more intense wind speeds associated with the DW regime observed at HUBC. The two North Carolina sites exhibited very different wind speed patterns. During 2-3 August the Raleigh site (Figure 2.7c) showed moderate strength LLJs with wind speeds of 11-12 m s⁻¹, while the DW speed was merely 6 m s⁻¹ and virtually indistinguishable from the ambient winds. Raleigh was located far enough east such that it experienced an LLJ regime similar to the northern sites, also along the Fall Line, but the DW regime was very weak. On the other hand, Charlotte was located far enough west that southwesterly flow never intensified into an LLJ regime (Figure 2.7d). The Charlotte site had the weakest winds of all four locations. The arrival of the DW regime was marked by a zone of increased wind speeds (4-6 m s⁻¹) from the surface to 3 km AGL. These features were in contrast to the otherwise calm background conditions.

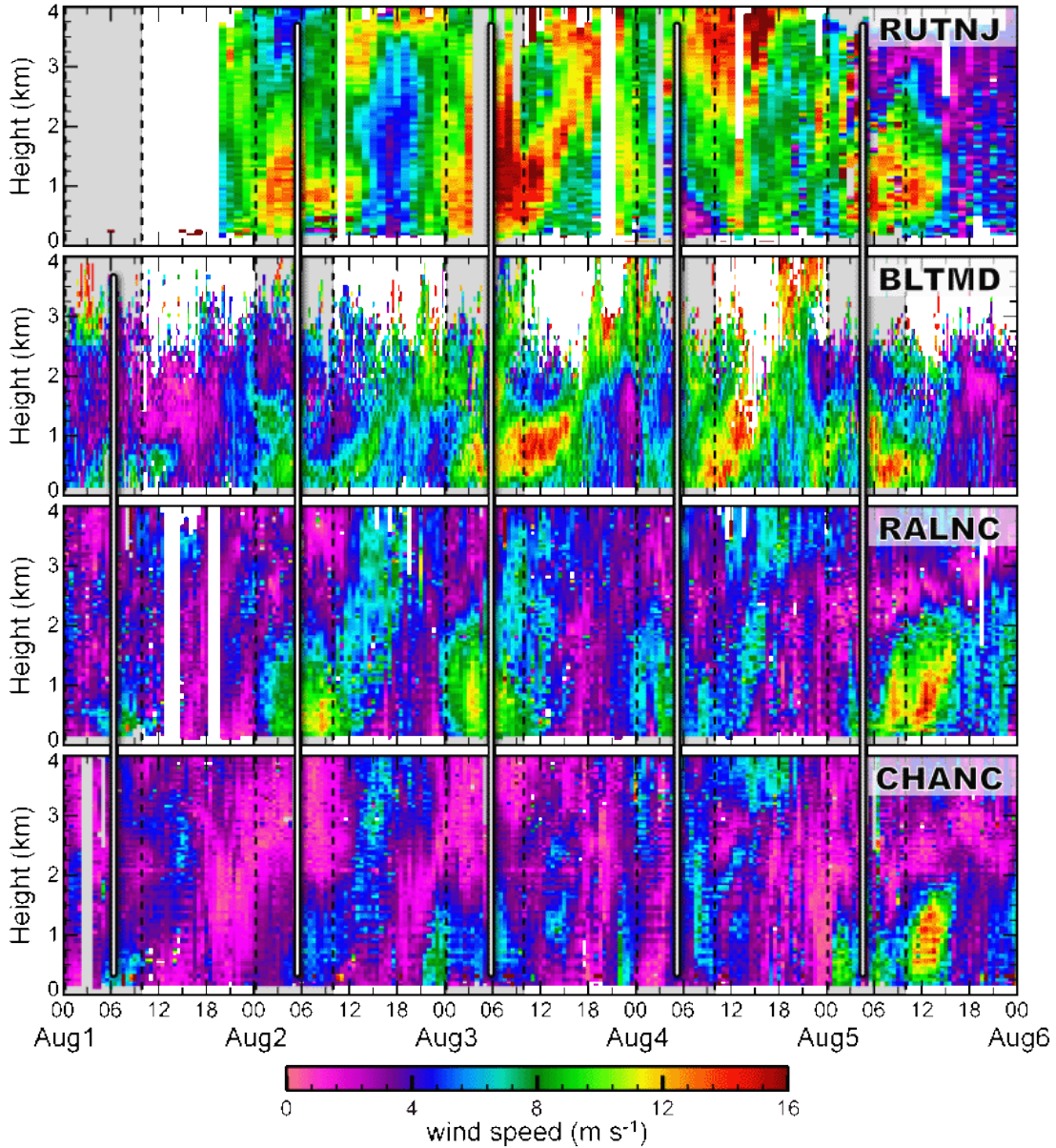


Figure 2.7: Same as Figure 2.6 except showing wind speed.

2.2.5 Regional WeatherBug network

Regional surface observations were used to help further investigate the nocturnal regimes. WeatherBug data from the Earth Networks company, based in Germantown, MD, offered high temporal resolution surface observations from hundreds of stations in the Mid-Atlantic region. Reporting stations were selected near

to north-south, west-east, and northwest-southeast transects to explore the propagation of nocturnal patterns in different directions. Figure 2.5 shows the station locations, labeled A-Q, that were used along the west-east transect.

All sites observed the daily pressure minima and maxima (not shown) similar to those observed at HUBC (Figure 2.4d). There was approximately an hour delay from the nocturnal minimum pressure recorded at Appalachian Mountain sites (A) to those located near the Atlantic Ocean (Q), separated by more than 400 km. This propagation speed would be too fast for most atmospheric waves, such as gravity waves. This evidence suggests that the twice daily pressure minima and maxima were the semidiurnal atmospheric tide (Whiteman; Bian 1996) and not caused by the LLJ or DW events.

Figure 2.8 shows wind from WeatherBug sites A-Q (Figure 2.5) for the nocturnal period of 2 August. We caution that not all WeatherBug sites demonstrate the nocturnal events equally as clear due to their individual geographic location or possible obstructions located nearby. The wind direction transition (α) from southwesterly to northwesterly begins at approximately 2300 UTC in the Piedmont Plateau (station F) and continues until 1200 UTC on Maryland's Eastern Shore (site P). Wind speeds after this transition remained relatively calm. Line β shows the propagation of a wind speed increase. It is believed that the wind speed increase was the DW flow moving eastward. This timing correlates very well with HUBC observations near site K. Wind data from the north-south transect located east of the Blue Ridge Mountains (not shown) revealed wind transitions that first appeared in the Potomac lowlands (Figure 2.5) and then fanned out eastward from there. This is

consistent with the behavior of drainage flows which follow the down-valley path of the least resistance (Sakiyama 1990), in this case, a notch in the Blue Ridge Mountains carved by the Potomac river.

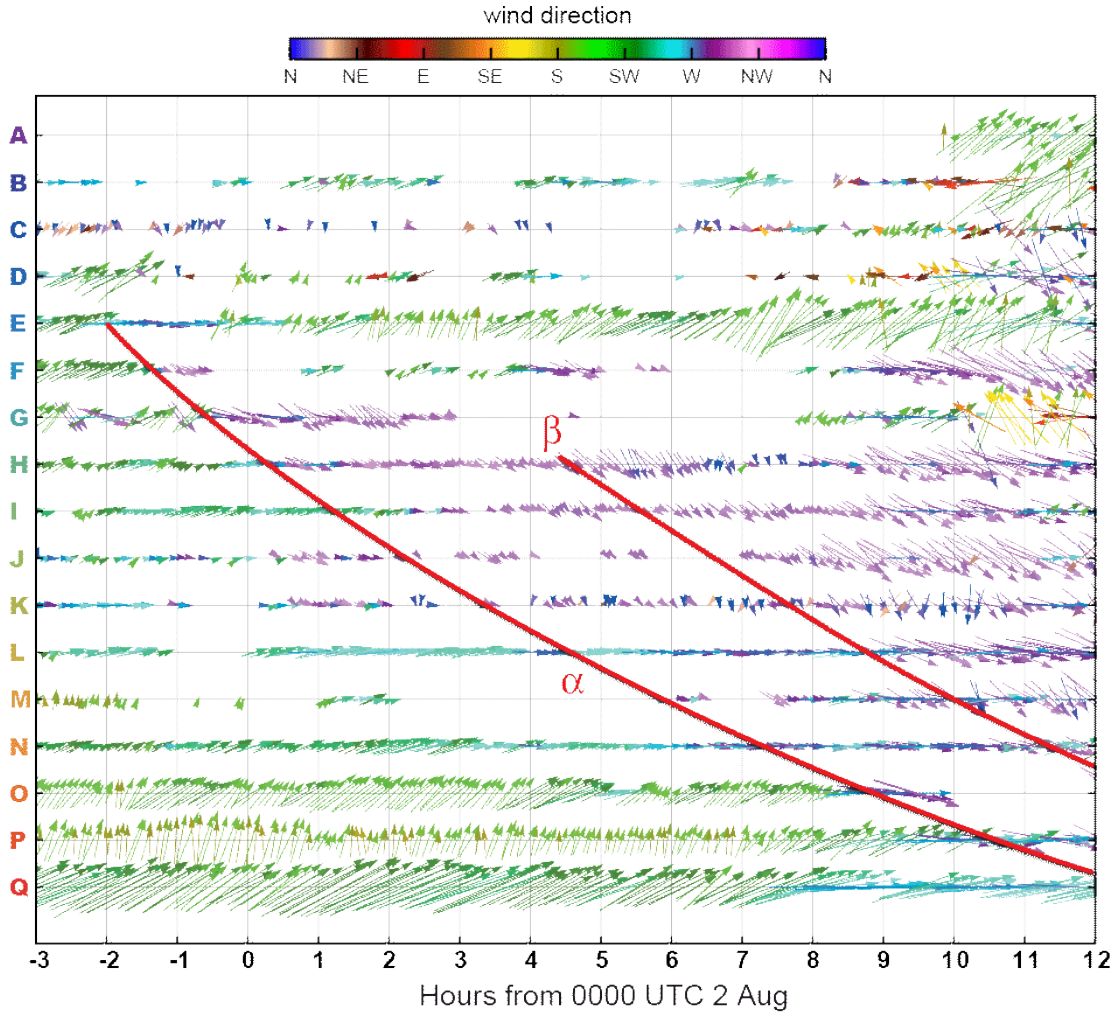


Figure 2.8: WeatherBug surface wind observations from 2100 UTC 1 Aug to 1200 UTC 2 Aug. Station sites are labeled A-Q and correspond to the locations in Figure 2.5. Vectors are oriented with the wind flow. Two red lines are superimposed to delineate the nocturnal transitions that propagated from west-to-east. Line α marks the change in wind direction and β marks the change in wind speed.

It is interesting to note that the DW event was most clearly observed by WeatherBug sites (Figure 2.5) around the northern Washington, DC region. It is suspected that the DW flowed down the east flank of the Blue Ridge Mountains and

then flattened along the surface moving eastward and moderating with distance. The region north of Washington, DC is located on a slight ridge directly downstream from the Blue Ridge Mountain notch and Potomac Lowland area where the strongest downslope flow would likely occur. Therefore, north of Washington, DC may have been the ideal surface location to experience the impact of the DW flow. It is further hypothesized that WeatherBug stations west of the Blue Ridge did not reveal any effect of the DW because those sites (located mostly in valleys) were isolated from the prevailing winds by the surrounding mountain ridges. This effect, when combined with nocturnal stability and the layered environment previously mentioned, allowed the DW to simply glide above the ribbed topography from the Appalachian Highlands down to the Blue Ridge Mountains without influencing surface observations below.

It should be emphasized that the relationship between surface and those a few hundred meters above can differ depending on atmospheric stability, stratification, nocturnal surface layer depth, or surface roughness.

2.3 Discussion

Measurements acquired during this case study provoke a closer examination of the classic PBL structure illustrated by Stull (1988) in Figure 2.9a. Stull's model assumes idealized conditions that do not account for the effects of terrain (Bader; McKee 1992; Kumar et al. 2012; Seaman et al. 2011), urban areas (Godowitch et al. 1985; Martilli 2002), coastal regions (Haman et al. 2012), or synoptic forcing (Gopalakrishnan et al. 1998; Krishna et al. 2003). This classic concept can be further modified by the occurrence of low-level flows such as LLJs, DWs, or other katabatic winds. The classic Stull model is best realized for clear, calm days/nights over flat

terrain without external forcing from significant disturbances. However, in the Mid-Atlantic region, there is a complex interaction between topography and thermal gradients that influence low-level flows. WAVES observations indicated more nocturnal phenomena that differ from the classic notion of the PBL evolution.

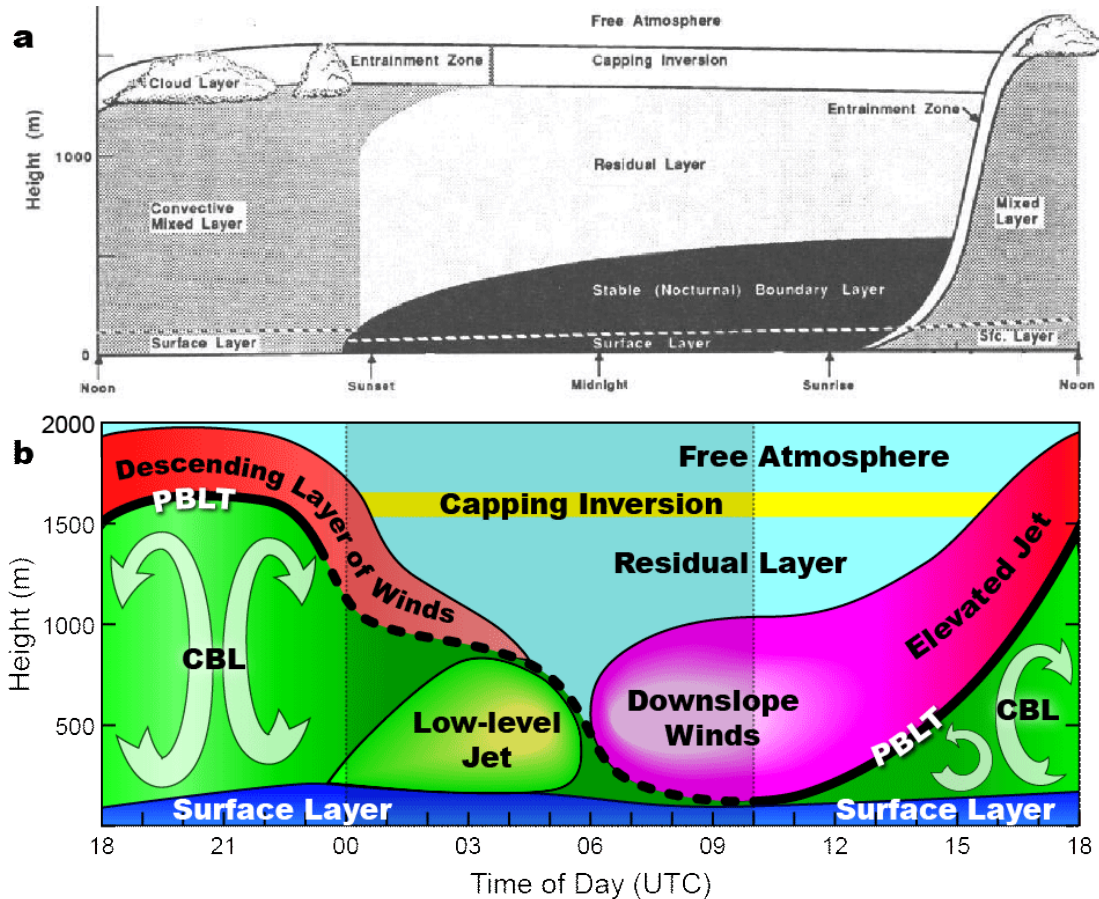


Figure 2.9: Diurnal evolution of (a) the classic boundary layer depicted by Stull (1988) and a (b) modified PBL evolution according to case study observations.

A modified depiction of the diurnal cycle is presented in Figure 2.9b, which is more reflective of the prefrontal observations during this case study. The modified diurnal cycle can be simplified into three stages: (I) daytime CBL development, (II) partial PBL collapse near sunset with an intensification of low-level flows that are

conducive for LLJ development, and (III) displacement by a different air mass described as a DW flow.

It is challenging to discern the evolutionary structure and height of nocturnal PBLs, or those that are decaying late in the day. During these times, vertical gradients which distinguish the PBL from the free atmosphere are more subtle compared to the starker contrasts that are usually observed during the daytime CBL. In the absence of a thermal time-series, which could better identify atmospheric layers based on temperature inversions, the PBL top (PBLT) was estimated by overlaying wind and lidar profiles and correlating the heights with strong gradients. For example, sharp contrasts between the ASR values within the CBL and the cleaner air above were useful for estimating the PBLT. Another gradient that frequently appeared was a noticeable difference in wind direction between the PBL and the free atmosphere. Often, wind speeds increased immediately above the PBL which further aided PBLT placement. Lastly, the wind profiler signal to noise ratio (SNR) was also used to help determine the PBLT. SNR data is related to beam refraction which occurs in regions with moisture or temperature gradients, such as inversion layers or entrainment zones. Locations where the PBLT is a dashed line (Figure 2.9b) indicate some height uncertainty between the data. Generally speaking, correct determination of nocturnal PBL height is an active area of research. However, periodic HUBC soundings agree with the PBLT placement in this case study.

Several differences between Figs. 9a and 9b can be identified. Among the most notable differences is the nocturnal structure. The first half of each night was marked by the LLJ regime, and the second half by the DW regime. Neither

phenomenon is accounted for in Stull's model nor in the classic understanding of nocturnal PBLs. Near sunset, the top of the CBL did not appear to decouple aloft and subsequently fade into a residual layer, but rather a layer of higher wind speeds descended during the early nighttime period. This led to a top-down erosion of the decaying PBL, which was slowed by the presence of the developing LLJ regime in the lowest 1 km. The LLJ regime maintained homogeneity in the lowest 1-km layer that was compositionally similar to stage I, but was significantly different from the air mass above. The bore-like appearance associated with DW arrivals presented a sharp contrast with the gradual upward growth of the stable boundary layer (SBL) depicted in Figure 2.9a. Each of these stages are discussed further below.

2.3.1 Stage I: Convective boundary layer

The growth of the CBL began with sunrise, shortly after 1000 UTC (0600 LDT) each day, and continued until about 1800 UTC. This period of CBL growth is denoted with a cyan line (Figure 2.10) above a layer of higher ASR values which rises from 400 m to 1.7 km. ASR values often peak near the top of the CBL due to the larger effective radius of particulates from hygroscopic growth in air with higher relative humidity. The air above the CBL tends to be cleaner due to diffusion by stronger winds aloft which usually advects particulates away from sources in lower atmosphere. Therefore, the ASR data shows a clear gradient marking the top of a growing or mature CBL. From 1800-2200 UTC the CBL maintained a maximum height around 1.7 km AGL. Very high ASR values (1500-2300 UTC) at the top of this layer indicated the presence of cumulus clouds. The afternoon CBL on 1-3 August was characterized by light west-southwest winds from 1700 UTC until dusk

(Figure 2.3c). The prefrontal mixing ratio within the PBL remained roughly uniform at 15-16 g kg⁻¹ (Figure 2.3a).

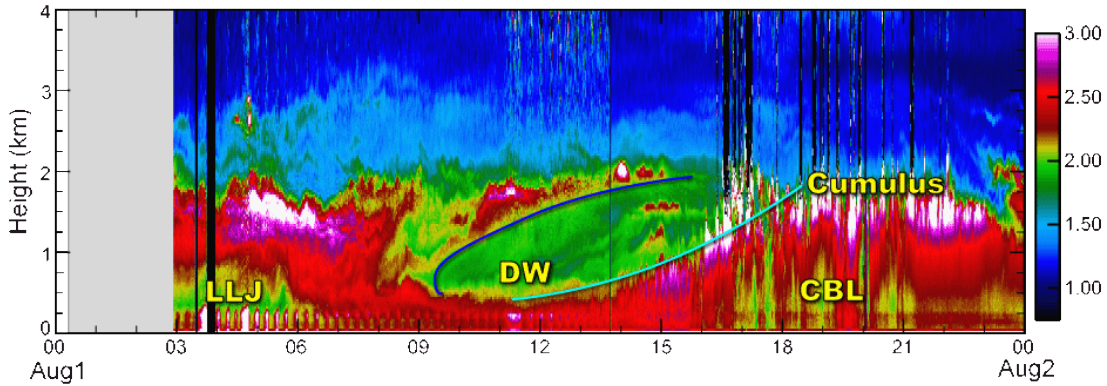


Figure 2.10: Enlargement of Figure 2.3b showing ASR data for 1 August. Important features are labeled. The blue line shows lifting by the DW, and the cyan line traces the top of the developing CBL.

2.3.2 Stage II: Nocturnal low-level jet regime

Figure 2.11 is an enlargement of ASR and wind data in Figure 2.3 from 1800 UTC 1 August to 1200 UTC 2 August. This day was representative of the prefrontal diurnal pattern, and provides a more detailed view of the nocturnal stages and transitions between them. The juxtapositional analysis of ASR, wind speed, and wind direction data provides a powerful diagnostic for inferring nocturnal structure and flow.

It is reasonable to place the initiation of the PBL collapse about 2 hours prior to sunset, or 2200 UTC. This is when the highest ASR values (Figure 2.11a) started decreasing in altitude. Scattered cumulus clouds, that were indicated by high ASR values at 1.7 km, began dissipating after 2300 UTC. Also at this time, a layer of higher wind speeds from the free atmosphere (2-3 km AGL) lowered in altitude, flowing just above the PBLT where it occupied the space left by a contracting PBL. Perhaps the best indicator of the waning PBL was the wind direction data (Figure

2.11b) which showed a descending transition (white line) that clearly divided northwesterly flow aloft from west-southwesterly flow below. The PBLT dropped from 1.7 to 1.0 km between 2200 and 0030 UTC. There was a pause in further descent of the PBLT until 0300 UTC. During this period, the sub-kilometer altitude wind speed intensified into the LLJ regime.

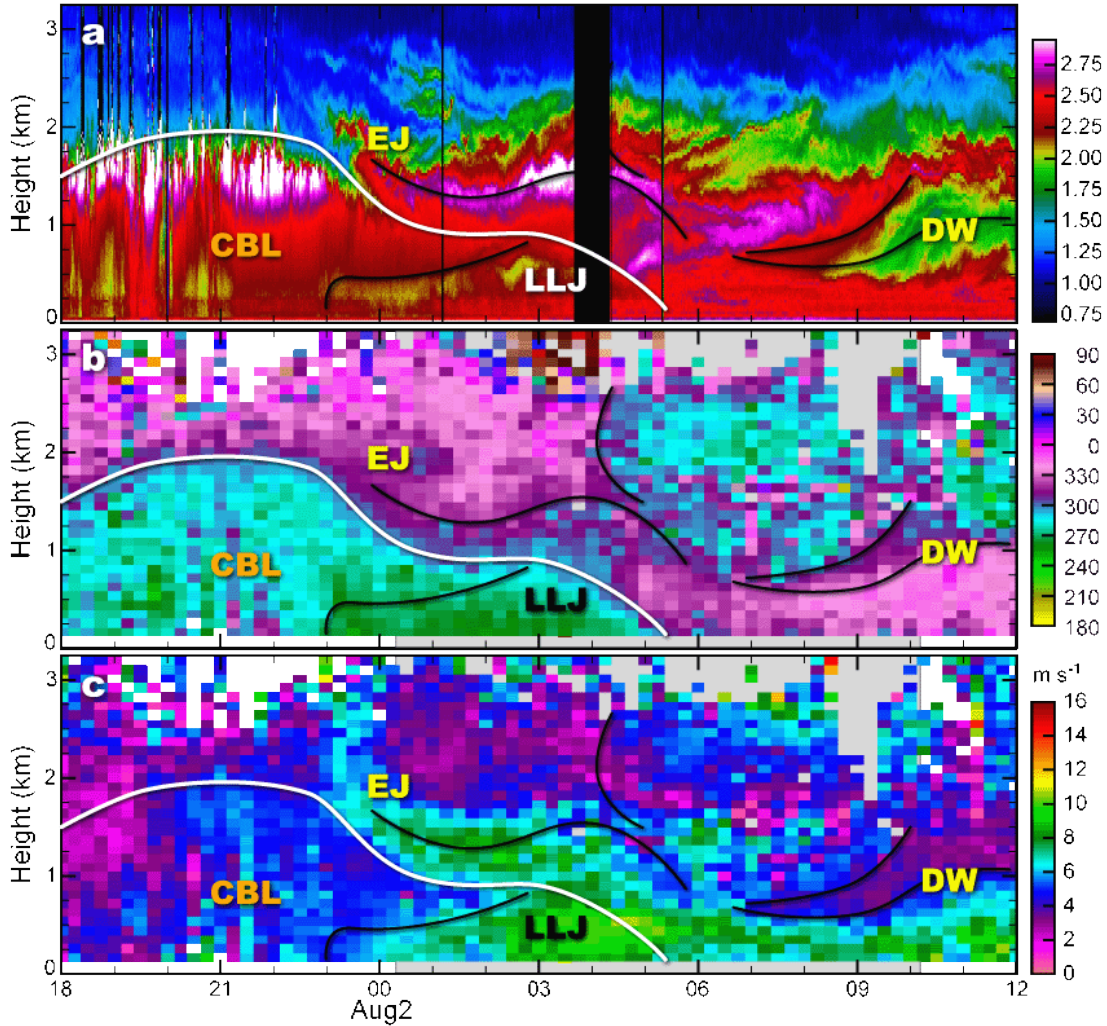


Figure 2.11: Enlargement of nocturnal phenomena from 1800 UTC 1 August to 1200 UTC 2 August. Panels show (a) ASR, wind (b) direction, and (c) speed. Collocated black lines are superimposed on each panel as visual aid to help identify common features between fields. White line is the hypothesized PBLT.

In order to draw a distinction between the LLJ, DW, or other regimes with low-level wind speed maxima, we narrow the LLJ definition by the following criteria.

(1) Wind direction being parallel to the terrain orientation is considered a primary indicator of a classic LLJ. (2) the temporal evolution of wind data throughout the evening hours is preferred to single vertical profiles, such as radiosondes or pilot balloons, which can overlook features capable of distinguishing LLJs from other phenomena. (3) Upon examining the time series data, the LLJ should originate below 1 km and appear decoupled from high wind speed features aloft. (4) Wind speed, direction, and other available observations, such as ASR, should be studied in conjunction with one another to assess the overall homogeneity of the air mass. Given the above criteria, the DW can be differentiated as a separate phenomenon from the LLJ.

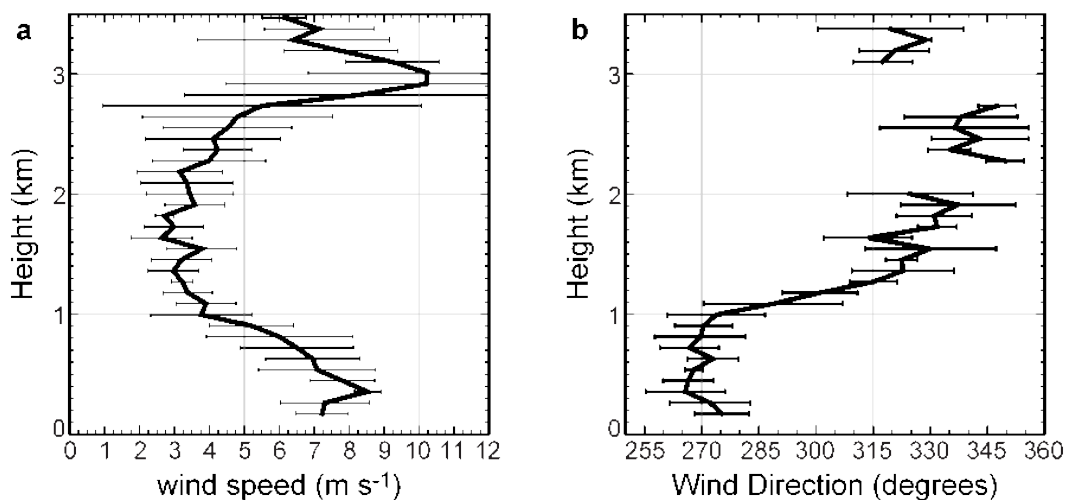


Figure 2.12: LLJ observed by Beltsville profiler showing (a) wind direction and (b) wind speed from 0430-0545 UTC 1 August.

Figure 2.12 shows a representative LLJ wind profile from 1 August at HUBC. This was the weakest LLJ regime out of the four prefrontal nights. The wind speed profile exhibited the classic nose characteristic peaking at 350 m AGL, with positive shear below and negative shear above (Figure 2.12b). The area of negative shear above the nose is the wind speed falloff region. On this night the wind direction

tended more westerly than southwesterly but shifted abruptly to the northwest above 1 km.

Overall, the LLJ regimes on 1-4 August had core wind speeds of 9, 11, 14, and 9 m s⁻¹ located at 350, 500, 500, and 400 m AGL, respectively. Wind speed falloff values above the LLJ nose averaged 5, 6, 6, and 4 m s⁻¹. Wind direction tended to have an increasingly southern component each night ahead of the cold front. The LLJs regimes in this case study sustained maximum wind speeds for 2-3 hours. The depth of the LLJ regime was shallow, below 1 km, and peak winds remained close to the surface.

2.3.3 Stage III: Downslope wind regime

The most striking features in the ASR fields were clean air slots that appeared in the first four days (labeled "D" in Figure 2.3b). They were somewhat less detectable but still present on 5 August after the cold frontal passage. These clearings appeared each day well before dawn between 0600-0800 UTC. They penetrated down to 500 m AGL on 1-2 August but extended to near ground level on 3-4 August (Figure 2.3b, Figure 2.11a). Furthermore, the clearings were correlated with a sharp change in wind direction out of the northwest and a simultaneous increase in wind speed that continued beyond dawn. The nights of 1-2 August showed much weaker DW wind speeds than 3-4 August. Furthermore, maximum wind speeds were located slightly below the ASR clearing on 1-2 August, but more towards the center of the clearings on 3-4 August.

We conjecture the onset of the DW eroded and displaced the LLJ regime. After the DW arrival, the PBLT appeared to have further decreased (white lines in

Figure 2.11c, d) based on the strong northwesterly wind near the surface. Soundings at 0655 UTC 1 August and 0644 UTC 3 August measured the temperature profile at the beginning of the DW events. A temperature inversion was located at roughly 150-200 m AGL for both days and is believed to be the approximate PBLT during the DW event of 2 August, too. This shallow layer provided some insulation from the effects of the DW regime, which were reflected by wind speed observations from the 31-m tower which never exceeded 3 m s^{-1} (Figure 2.4) compared to wind speeds over 12 m s^{-1} just above 200 m AGL (Figure 2.3).

2.3.4 Inertial oscillation

In addition to the three stages of the diurnal cycle during this case study, the lower atmosphere also experienced inertial oscillations. Blackadar (1957) and Holton (1967) were among the first researchers to link this with the development of the low-level jet. Blackadar showed the local tendency of the ageostrophic wind components

$$\frac{\partial}{\partial t}(u - u_g) = f(v - v_g) \quad \text{and} \quad \frac{\partial}{\partial t}(v - v_g) = -f(u - u_g)$$

could be combined with a complex variable and integrated to form the oscillating solution $W = W_0 e^{-ifW}$ where the period is $T = \pi / (\Omega \sin \phi)$ or approximately 19 hours at Beltsville's latitude. The variables u and v are the wind components where the subscript g designates them as geostrophic flow, f is the Coriolis force, Ω is the Earth's rotation, and ϕ is latitude. Figure 2.13 demonstrates a similar oscillation pattern but with more ellipticity consistent with Holton's case of a stable atmosphere over sloping terrain. This figure shows a hodograph of MDE wind profiler data illustrating the rotation of winds at three levels in the atmosphere (0.5, 1.0, and 1.5

km AGL) for the nighttime periods of 2 and 3 August. These inertial oscillations were interrupted by the passage of the DW before completing the precession. The wind transition of the DW has been marked by blue arrows.

The inertial oscillation was most pronounced at 500 m AGL (Figure 2.13a,b). This was consistent with all other observation data showing the LLJ core developed at this level. A slow rotation begins around 2100 UTC. After sunset, the turning of the winds accelerated and continued until 0800 UTC for 2 August and 0530 UTC for 3 August. At this point, the DW passed through Beltsville preventing further continuance of the oscillation. On 4 August (not shown) the oscillation was more distorted with much stronger DW winds. Furthermore, the oscillation had a shorter development time this night, directly correlated with the length of the LLJ regime. As previously mentioned, the duration of the LLJ was squeezed shorter each successive night the cold front drew closer to the Mid-Atlantic region. It is believed that the increased pressure gradients and stronger winds in the vicinity of the frontal boundary disrupted this inertial flow. Weak gradients are ideal for the oscillation and LLJ development. The night of 5 August (not shown) contained a distorted inertial oscillation in the wake of the cold front. Although a clockwise turning of wind still existed, it was not as obvious as previous nights. Interestingly, after 0300 UTC there was evidence of a disruptive event in the post frontal air mass, similar to the DW timing. It is believed that this corresponded to the inflow of the back door cold front, spotted in the radar refractivity mentioned previously.

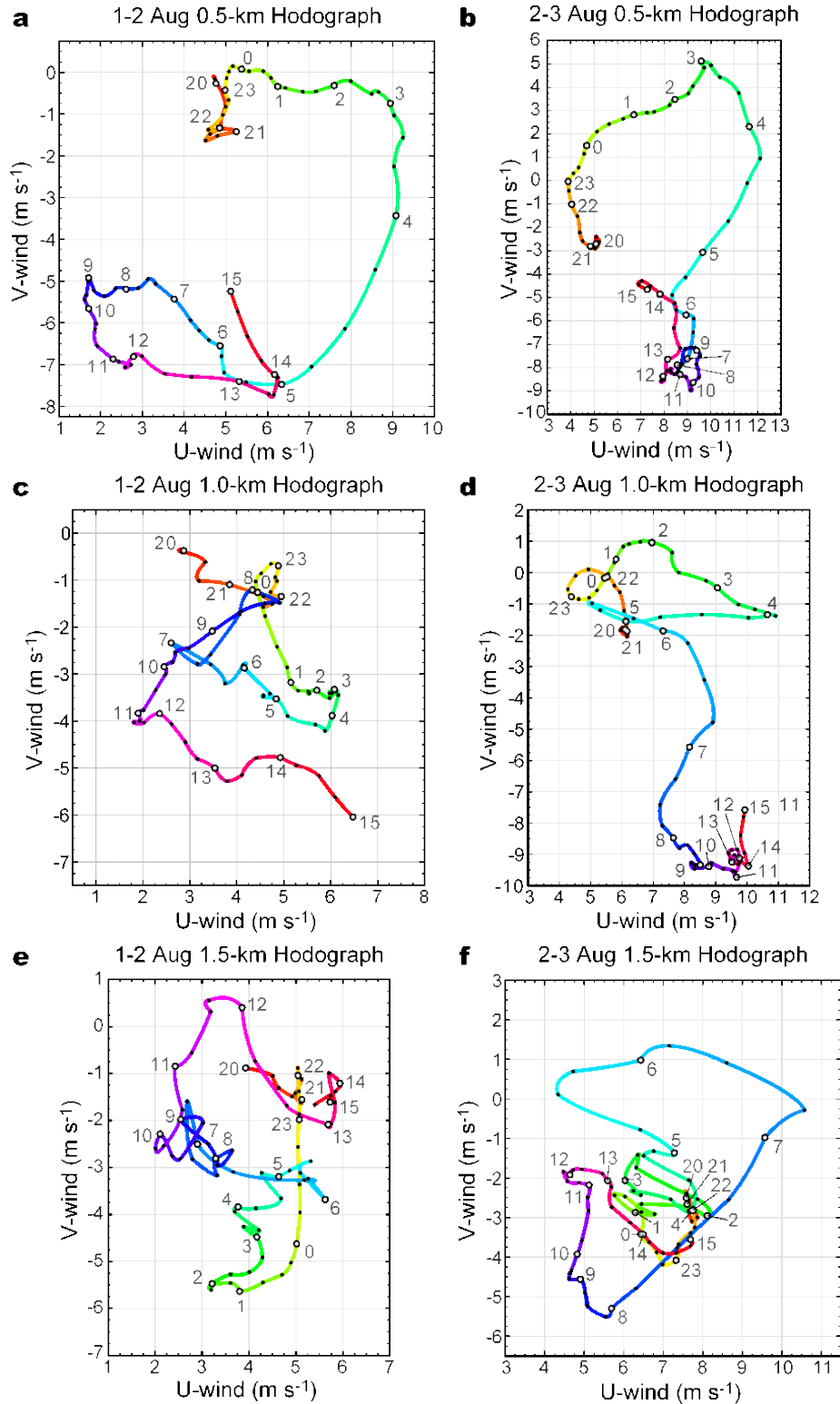


Figure 2.13: MDE wind profiler hodographs for the periods: (a,c,e) 2000 UTC 1 August to 1500 UTC 2 August, and (b,d,f) 2000 UTC 2 August to 1500 UTC 3 August. Hodographs are shown at three heights: (a,b) 0.5 km, (c,d) 1 km, and (e,f) 1.5 km.

At 1 km AGL (Figure 2.13c,d), a partial inertial oscillation was still evident, although greatly distorted compared to the 500 m level. The ellipticity of this oscillation had its major axis 90° out of phase with the 500 m level. Also, at 1 km the winds associated with the DW looked deceptively stronger than at 500 m. However, they were roughly comparable in magnitude. The difference is that the inertial oscillation was much smaller at 1 km, especially the meridional component. This led to a much more striking transition after the DW.

At 1.5 km (Figure 2.13e,f), the oscillation on 2 August was barely visible (Figure 2.13e). On 3 August, however, the oscillation was primarily evident from 0500-0800 UTC (Figure 2.13f). It correlated very well with the timing of the 500 and 1000 m levels DW transition. Since other observations indicated the DW event on 3 August was much stronger than on 2 August, it is possible lower layers of the atmosphere were lifted to 1.5 km, still retaining some rotational momentum and thereby delaying the oscillation observed at 1.5 km layer. Lifting of layers is consistent with lidar ASR (for example, Figure 2.9).

2.3.5 Prefrontal trough

During this case study a cold front with a prefrontal trough passed over the Mid-Atlantic region and was measured by WAVES instruments. Although these synoptic features significantly influenced the observed fields, evidence of the diurnal cycle persisted and was enhanced by the prefrontal trough.

There have been many publications discussing prefrontal troughs and wind shifts. Schultz (2005) provided a review of the observational evidence and theories behind these features. While prefrontal troughs do not accompany all cold fronts,

WAVES observations indicate one passed through HUBC 24 h in advance of the cold front. The HUBC 5-day surface pressure minimum occurred at 2100 UTC 3 August (Figure 2.4d). However, the exact timing of the trough's passage is uncertain because of the diurnal tide that is superimposed on the pressure trend, which could potentially offset the overall minimum pressure. A boundary associated with the prefrontal trough was estimated from the Rapid Update Cycle (RUC) analysis fields (Figure 2.2). The impact of the trough was to enhance the DW regime and change the wind direction during the daytime of 4 August.

One of the most striking features in the 1-5 August dataset was the DW event at 0600 UTC 4 August. ASR measurements (Figure 2.14) revealed a large bore-like curl in the lowest kilometer (0600-0730 UTC) resulting from air mass displacement, although a close examination of the data showed hints of displacement as early as 0400 UTC. Strong lifting is visually evident from 0700-1200 UTC between 0.5-2.5 km, marked by the arrows.

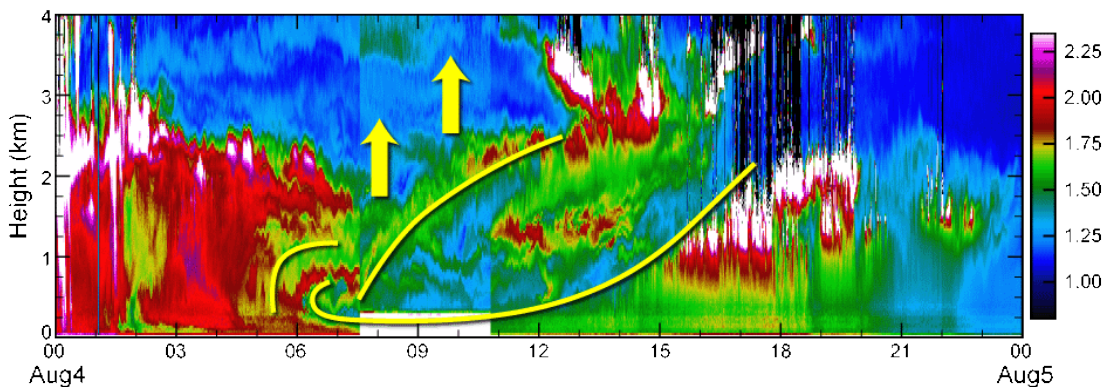


Figure 2.14: Enlargement of Figure 2.3b showing ASR data on 4 August. Yellow lines accentuate the DW air mass, with arrows indicating areas of lifting. The DW event was greatly enhanced by the prefrontal trough compared with previous days.

The exaggerated magnitude of the DW arrival distinguished 4 August from all other days in the case study. The DW regime on this day was coincident with the

tropospheric wind shift behind the prefrontal trough. The afternoon wind direction in the CBL never became southwesterly as it had done every preceding day (Figure 2.3d). Furthermore, the DW event of 4 August was not confined below 1.5 km AGL, as was typical on the preceding days, but rather it extended aloft and exhibited a vertical slant analogous to a frontal boundary. Lidar data revealed a decrease in WVMR within the lowest kilometer which was noticeably different from the other DW events.

2.3.6 Cold front

The passage of the cold front ("F" in Figure 2.3) occurred at 2230 UTC. Near surface wind speeds (Figure 2.3c) increased over 10 m s^{-1} and the wind direction (Figure 2.3d) changed from northwesterly to northeasterly. There was a sharp decrease in ASR from 2100-2300 UTC 4 August as the frontal nose passed over HUBC (Figure 2.3b).

The frontal boundary was evident by the crisp line in the satellite water vapor data that was crossing HUBC at 2245 UTC (Figure 2.15a). The front was oriented from southwestern Virginia to northeast Maryland and pushing southeastward, as indicated by the large blue arrows. The cold frontal boundary contained significant vertical shear between upper-level and lower-level flows which were 180° out of phase. Upper-level clouds experienced a transverse flow, relative to the front, that was associated with the warm conveyor belt (Figure 2.15a, orange arrow). However, the sequence of satellite infrared images (not shown) indicated that faint low-level clouds were moving southwestward, directly opposite to the clouds above. A sequence of base reflectivity images from 1930-2355 UTC at the Sterling, VA radar

site confirmed the presence of low-level southwestward motion (not shown). Subtle clear-air refractivity returns tracked density gradients associated with the surface outflow from a pool of cooler air to the north behind the frontal boundary. A snapshot at 2110 UTC is provided in Figure 2.15b showing the southwestward propagation of the advancing density gradients. HUBC wind direction during this time corroborates an increasingly easterly flow component below 1.8 km. Above that height, the wind direction remained northwesterly until the profiler data dropped out (~3 km AGL).

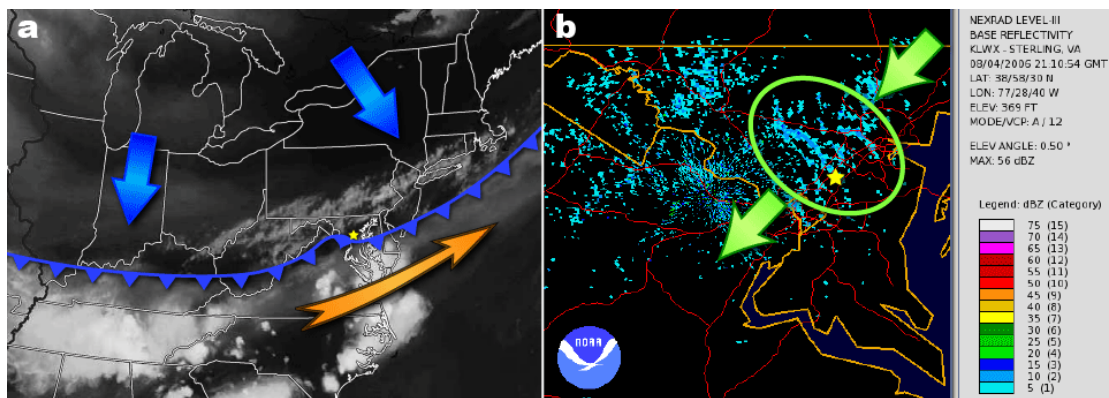


Figure 2.15: (a) Water vapor satellite image at 2245 UTC. Blue (orange) arrow(s) show the general motion of the frontal boundary (upper-level clouds). (b) The KLWX (Sterling, VA) base reflectivity at 2110 UTC shows refractive lines, in the circled area, which were moving opposite of the upper-level clouds.

The northeasterly low-level flow behind the frontal passage was consistent with the characteristics of a back-door cold front (Bosart et al. 1973; Hakim 1992), even though the upper-level orientation of the cold front appeared to be a normal "front door" cold front. It is hypothesized that this cool dense air moved southward down the lowlands of Susquehanna and Delaware river valleys, or more broadly, across the lower terrain of the Appalachian Mountains located to the north. Consequently this flow would arrive at HUBC first, from the northeast, before the postfrontal air could traverse the higher elevations directly to the west. After passing

through HUBC, the cool air continued moving southwestward, parallel to the Appalachian Mountains, across terrain with minimal surface friction. By 0000 UTC 6 August, the frontal orientation had become nearly west-to-east (Figure 2.1f) which supports the notion of a faster frontal propagation east of the Appalachian Mountains where surface friction is lower.

2.4 Summary

The WAVES field campaign began in June 2006 and continued until August, collecting coordinated measurements used for satellite validation and inter-instrument comparison. During the week of 1-5 August, the campaign began a continuous observation period anticipating several days with poor air quality that would end with a frontal passage. This data set captured intriguing cyclical low-level flows during the prefrontal period, a prefrontal trough, and the passage of the cold front, which composed the basis for this case study. The prefrontal trough and the cold front were two principal meteorological features of interest in this study. Not every cold front has an accompanying prefrontal trough, nor are the mechanisms behind their formation fully understood.

An important contribution of this study was the combined use of several research-grade measurements to help discern the structure and evolution of the LLJ, DW, prefrontal trough, and cold front. The collocation of complementary observation data enable a better diagnosis of low-level flows. WAVES observations showed the impact of the prefrontal trough on the overall wind field and its enhancement of nocturnal low-level flows. The low-level flow behind the passage of the dry cold

front behaved similarly to a back-door cold front. The cold front brought in significantly drier, cooler air in the following days.

Results also showed a distinct diurnal pattern during the prefrontal period of this case study, which can be categorized into 3 stages: (1) a CBL regime, (2) a LLJ regime, and a (3) a DW regime. The 3-stage regimes modify the classic view of the nocturnal boundary layer due to the geographically diverse surface characteristics of the Mid-Atlantic region. The CBL regime in stage I was not much different from Stull's depiction. Late morning periods were characterized by northwesterly flow with wind speeds that diminished and veered southwesterly by late afternoon. Stage II began near sunset when the PBL collapsed to half its height and sub-kilometer wind speeds intensified. This was classified as a LLJ regime because the flow was parallel to the mountains, and because of its similarity to the Great Plains LLJ. Stage III occurred halfway through the nighttime when stronger northwesterly winds displaced the LLJ regime.

This research has emphasized the importance of a holistic analytical approach to low-level wind observations, discriminating between low-level wind speed maxima based on air mass properties or origination. The wind speed profiles of the DW regime were very similar in appearance to those of LLJs. However, we have presented evidence that the DW was an invading air mass with flows orthogonal to the mountains. Therefore, the DW flow should be categorized separately from the classic notion of a "low-level jet" by taking into consideration wind direction and other observations that highlight air mass differentiation.

Because WAVES observations were obtained in time series at a few limited sites, it is not possible to examine three-dimensional structures of the nocturnal LLJ and DW regimes. Thus, in Chapter 3, we will investigate the temporal and spatial evolution of these low-level flows from numerical simulations. Some hypotheses raised in the present paper will also be validated.

Chapter 3: Numerical Simulations

High resolution model simulations, that were simultaneous with a period of intensive field observations from the WAVES campaign, were performed for 1-5 August 2006 over the Mid-Atlantic region. In chapter 2, observations were analyzed revealing a prominent diurnal cycle with two distinct nocturnal low-level wind regimes: (1) a nocturnal LLJ and (2) a hypothesized DW flow. In this chapter the focus is on examining the regional wind flow simulated by WRF during the LLJ and DW regimes, after first comparing WAVES observation profiles against the model. The modeling presented here goes beyond what can be deduced from single site measurements and thus provides a broader understanding of the meteorological context and offers explanations that WAVES observations alone cannot address.

The objectives of this chapter are to (a) assess WRF performance through verification with WAVES observation profiles; (b) determine the origin and evolution of the LLJ and DW events; and (c) highlight the basic mechanisms behind the low-level flows. The investigation of low-level flows in the Mid-Atlantic is not just important to the science of NWP, but also to the environment through air quality forecasting or wind energy solutions.

3.1 Experiment Design

Advanced research WRF is a rapidly developing community model, primarily supported through the National Center for Atmospheric Research, with an aim to meet the scientific needs of the weather prediction and simulation research. WRF was selected to simulate this case study because it is a fully non-hydrostatic mesoscale

model with multiple physics options, parameterizations, and other capabilities that allow customized atmospheric investigation within a flexible framework.

3.1.1 Control run

WRF was configured using (i) Goddard microphysics, (ii) RRTMG longwave and shortwave radiation schemes, (iii) Noah Land Surface Model, (iv) Urban Canopy Model, (v) Mellor-Yamada-Janjic (MYJ) PBL scheme, and (vi) no parameterization for cumulus. The model physics configurations (v) and (vi) were optimally determined from the sensitivity tests in Chapter 4. Figure 3.1a shows the locations of the outer domain (D1) and the nest domain (D2) with (x, y, z) dimensions of $429 \times 299 \times 60$ and $270 \times 249 \times 60$, respectively. D1 and D2 had uniform horizontal spacing of 4.5 and 1.5 km, respectively. Vertical levels in both domains were distributed approximately linearly in pressure, with a slightly higher concentration of levels near the surface. The geographic inputs for both domains were 30 arc-second topographic data and 30 m resolution urban intensity data from the 2001 National Land Cover Dataset (NLCD). Additionally, D2 uses the 2001 NLCD land use (LU) data instead of the default WRF LU data. Initial and boundary conditions were interpolated from the North American Regional Reanalysis (NARR) data, which produced slightly better results than the RUC or North American Mesoscale (NAM) data, as shown in Chapter 4.

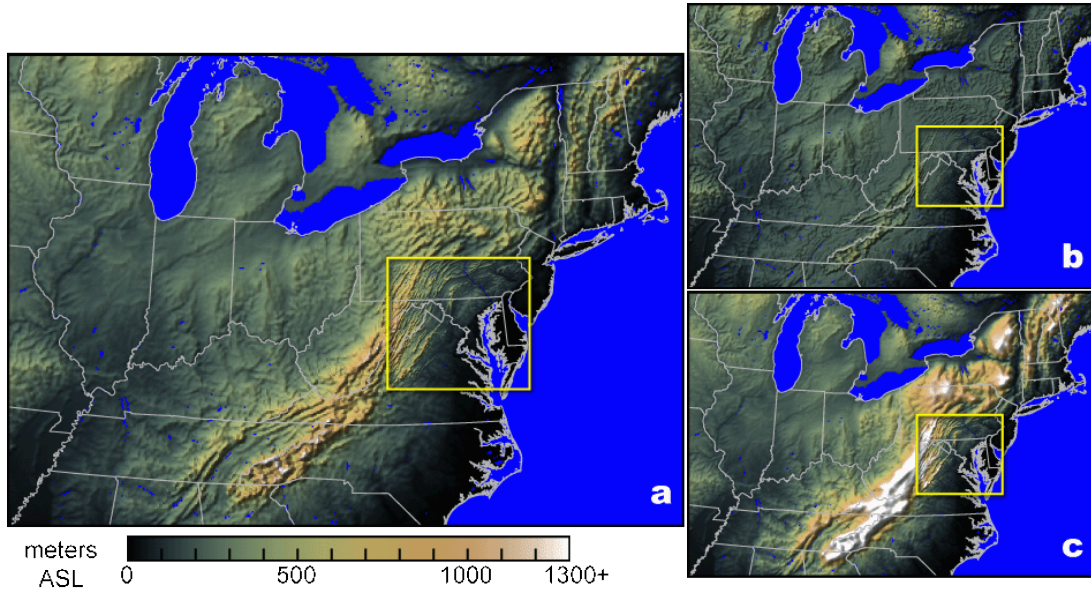


Figure 3.1: Locations of outer domain (D01) and nested domain (D02) outlined in yellow. WRF terrain elevation scaled by (a) 100% in run IN212, (b) 40% in run IN212L, and (c) 200% in run IN212H.

Three control simulations were run during the case study period to examine the low-level flows associated with the diurnal cycle. Runs IN112, IN212, and IN312 were initialized at 1200 UTC 1 August, 1200 UTC 2 August, and 1200 UTC 3 August, respectively. Each simulation ran 30 hours, except for IN312 which was extended to 48 hours in order to examine the frontal passage. Since one of the objectives is to accurately simulate the LLJ and DW events, revisiting the NARR reanalysis to obtain initial conditions every 24 hours was chosen as a better approach than using a single long run. This approach mitigated the tendency for the model to drift after extended simulation times. A 1200 UTC initialization time was chosen to allow sufficient time for model spinup and development of convective processes which could affect low-level flows after nightfall. Chapter 4 will demonstrate that selecting the 1200 UTC initialization time, followed by a 4-6 h spinup produced the best overall results.

3.1.2 Terrain height modification

Two additional experiments were conducted to explore the impact of the Appalachian Mountain height on regional circulations and low-level flows. Mountain heights were increased by 200% in run IN212H (Figure 3.1c). In this experiment, Gaussian smoothing was applied to elevation data in order to mitigate potential model instability generated through unrealistically steep slopes. In the second experiment, run IN212L, mountain elevations were reduced by 40% (Figure 3.1b). Gaussian smoothing was also applied to these elevations. The terrain height modification process was accomplished through an explicit selection of geography that isolated the Appalachian Mountains, then exaggerated those terrain elevations, followed by feathering the selection into the surrounding topography. This produced a smooth transition between the modified and unaltered terrain elevations and preserved the appearance of geographic features. Simulations IN212H and IN212L were designed for direct comparison with IN212 which used true elevation data.

The fine nest domain of these simulations is delineated by the yellow bounding boxes in the panels of Figure 3.1. The nest domain encompasses the Maryland region and is centered at the HUBC. This region is composed of a complex geography with seven major topographic categories and includes the additional interaction of continental and maritime air masses of the Chesapeake Bay and Atlantic Ocean. A more lengthy discussion regarding the unique geography of the Mid-Atlantic and an illustration are provided in Chapter 2.

3.2 Model Verification

3.2.1 Winds

WRF control simulations were compared with WAVES observation profiles to assess how well the model was able to reproduce the low-level flows measured at HUBC. Wind direction profiles from all three control runs were seamed together at 1800 UTC 2 and 3 August for comparison with WAVES observations from the MDE wind profiler (Figure 3.2). The side-by-side comparison of wind direction data shows many common features between the model and observations. The LLJ regimes are identified by the southwesterly flow (yellow-green shading) below 1 km from 0000-0400 UTC. The DW regimes are identified by periods with northwesterly flow (purple shading) below 1.5 km from 0700-1500 UTC. Overall, WRF demonstrated the ability to simulate the LLJ and DW regimes that were observed at HUBC. In particular, the timing and vertical distribution of these features were very similar.

The LLJ regime was further analyzed by averaging the observed and modeled wind speed and direction from 0100-0400 UTC 2-4 August. Since wind profiles from all three days were similar, a representative profile from 3 August is shown in Figure 3.3. The maximum observed mean wind speed in the LLJ regime (Figure 3.3a) was about 10 m s^{-1} located approximately 400 m above ground level (AGL). The model maximum mean wind speeds were in agreement with observations, although they were slightly faster by 0.75 m s^{-1} . The shape of the profile was the primary difference between the modeled and observed mean wind speeds. Observations showed a more rapid falloff to 6 m s^{-1} at 1.5 km AGL, which increased to a secondary maximum of 8.5 m s^{-1} at 2 km AGL. On the other hand, the model mean wind speed profile

showed a more linear and gradual decrease from the nose (peak winds) up to 3 km. The location and magnitude of the LLJ nose was reproduced fairly well by WRF, but the model did not represent the multiple inversion layers with different wind speeds as accurately due to the lack of vertical resolutions in the model initial conditions and model itself.

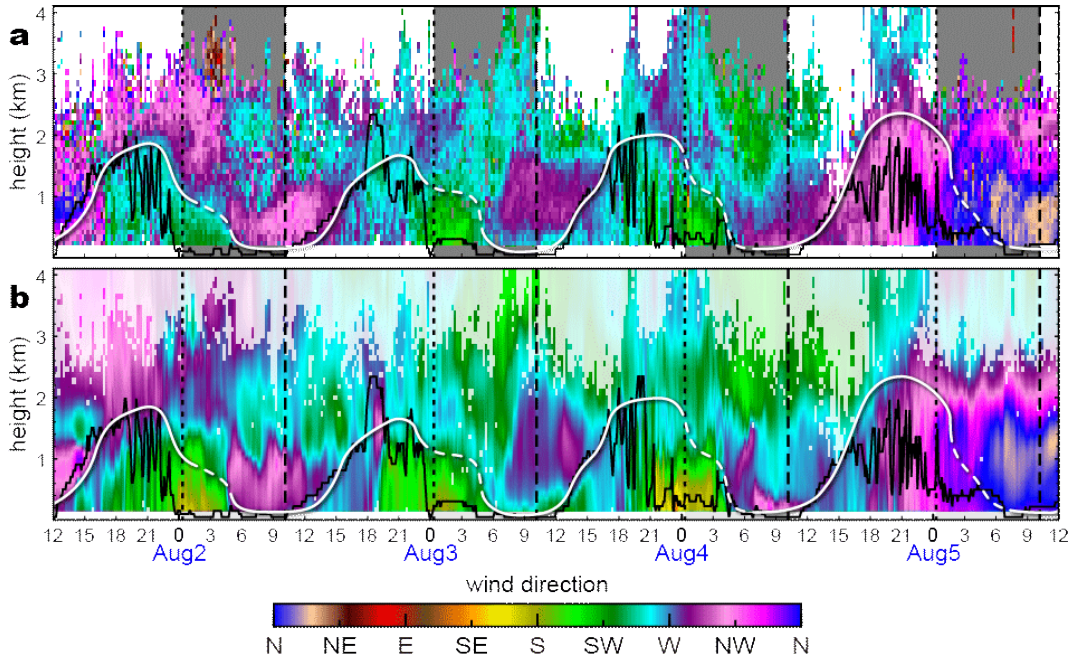


Figure 3.2: Observed (a) and control run (b) wind direction indicated by shading. Sunrise (dashed lines), sunset (dotted lines), nocturnal periods (gray) are indicated, Model (black line) and observed (white line) PBLT are superimposed on both panels.

The mean wind direction between the model and observations was also in close agreement for the LLJ regime (Figure 3.3b). Below 1 km AGL, winds are solidly southwesterly. WRF sub-kilometer winds have a slightly stronger southerly component than observations. In fact, the overall wind direction profile of the model appears to be rotated 10-20° counterclockwise from the observed mean wind direction profile. This is slightly more evident on the days of 2 and 4 August (not

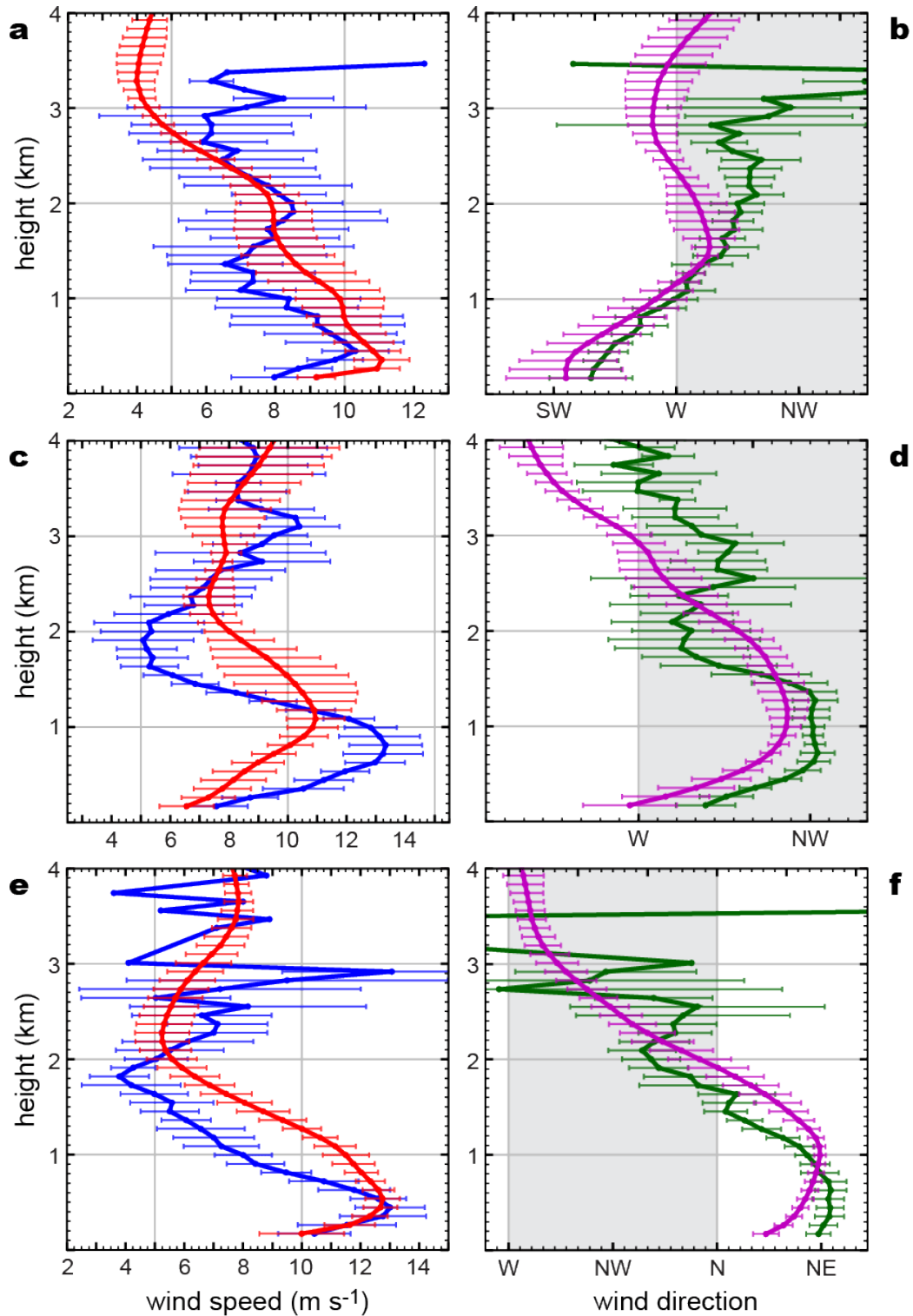


Figure 3.3: Mean LLJ profiles showing wind (a) speed (m s^{-1}) and (b) direction (degrees) from 0100-0400 UTC 3 Aug. Mean DW profiles showing wind (c) speed and (d) direction from 0800-1200 UTC 3 Aug. Mean post-frontal wind profiles showing wind (e) speed and (f) direction from 0800-1200 UTC 5 Aug. Wind observation profiles are plotted using blue/green lines, and model profiles use red/purple lines. Northwest quadrant of wind direction is shaded gray.

shown). The observed mean wind direction on 2-3 August was more northwesterly above 2 km whereas the model wind direction was more westerly.

The DW regime was also analyzed by averaging wind speed and direction from 0800-1200 UTC 2-4 August. Mean wind speed (Figure 3.3c) and direction (Figure 3.3d) from 3 August is representative of the DW regime. The observed mean wind speed reaches a maximum of almost 13.5 m s^{-1} around 800 m AGL, then decreases sharply to 5 m s^{-1} at 1.75 km. WRF underpredicts the sub-kilometer peak wind speeds, only reaching 11 m s^{-1} at 1 km AGL. The model mean wind speed falloff is also reduced to a 4 m s^{-1} difference compared to the observed 8.5 m s^{-1} difference. The model mean wind speed maxima on 2 and 4 August also fall short of observation values. Furthermore, the distance between the inflection points in the model mean wind speed data for all three days appears to be vertically stretched compared to the matched inflection points in the observation data. This is an indication that atmospheric layers within WRF are thicker than the observed layers.

The mean wind direction data below 1.5 km during the DW regime was northwesterly for both the model and observation data (Figure 3.3d). As before, the model mean wind direction appeared to be rotated $10\text{-}20^\circ$ counterclockwise relative to the observed values. It is also interesting to note the change in the mean wind direction between the LLJ and DW regimes above 2 km. During the LLJ regime, the wind direction was slightly northwesterly at these altitudes, whereas it was slightly southwesterly during the DW regime just a few hours later. This is the opposite pattern of the wind direction below 2 km. If a broad lifting of the sub-kilometer LLJ layer occurred, the effect would transfer some southwesterly momentum upward. The

change in wind direction above 2 km supports the theory that the advancing DW displaced the LLJ regime vertically and not just horizontally.

Figure 3.3e and f show the mean wind speed and direction from 0800-1200 UTC 5 August. Although this was not classified as a DW event, the observed mean wind speed (Figure 3.3e) had a similar profile with a maximum of 13 m s^{-1} at 500 m AGL that decreased to 4 m s^{-1} just below 2 km. WRF was able to reproduce a similar profile but could not reach the minimum falloff wind speed or the thinner layer of low-level winds. The mean wind direction profile (Figure 3.3f) had a similar shape to the DW profile, but was nearly 90° out of phase and characterized by strong low-level northeasterly winds instead. Increased directional shear was evident between 1-3 km compared to the same time and region of the DW event.

3.2.2 Mixing ratio

Figure 3.4 compares SRL mixing ratio and model values. WRF had an overall dry bias within the PBL (Figure 3.4c). The exception to this pattern was the daytime of 4 August, where the model showed a slightly moister PBL after the passage of the prefrontal trough. The observed air mass behind the prefrontal trough was dryer than the simulation accounted for. WRF typically showed a shallow layer with a slightly moist bias immediately above the PBL. This corresponded to the model's inability to reproduce the sharp decrease in moisture above the PBL, which was observed in lidar and sonde profiles. However, the free atmosphere above this varied from moist bias during the night of 2 August to a dry bias on the night of 4 August. It appears as though the observed 2-6 km moisture trend was increasing for observations ahead of the cold front, but not reflected in the model simulation. It is interesting to note the

model dry biases from 0.5-3.0 km that occurred each night around 0600 UTC (Figure 3.4c). The timing of these features corresponds to the DW events at HUBC. The model simulated DW events were dryer than the observed ones.

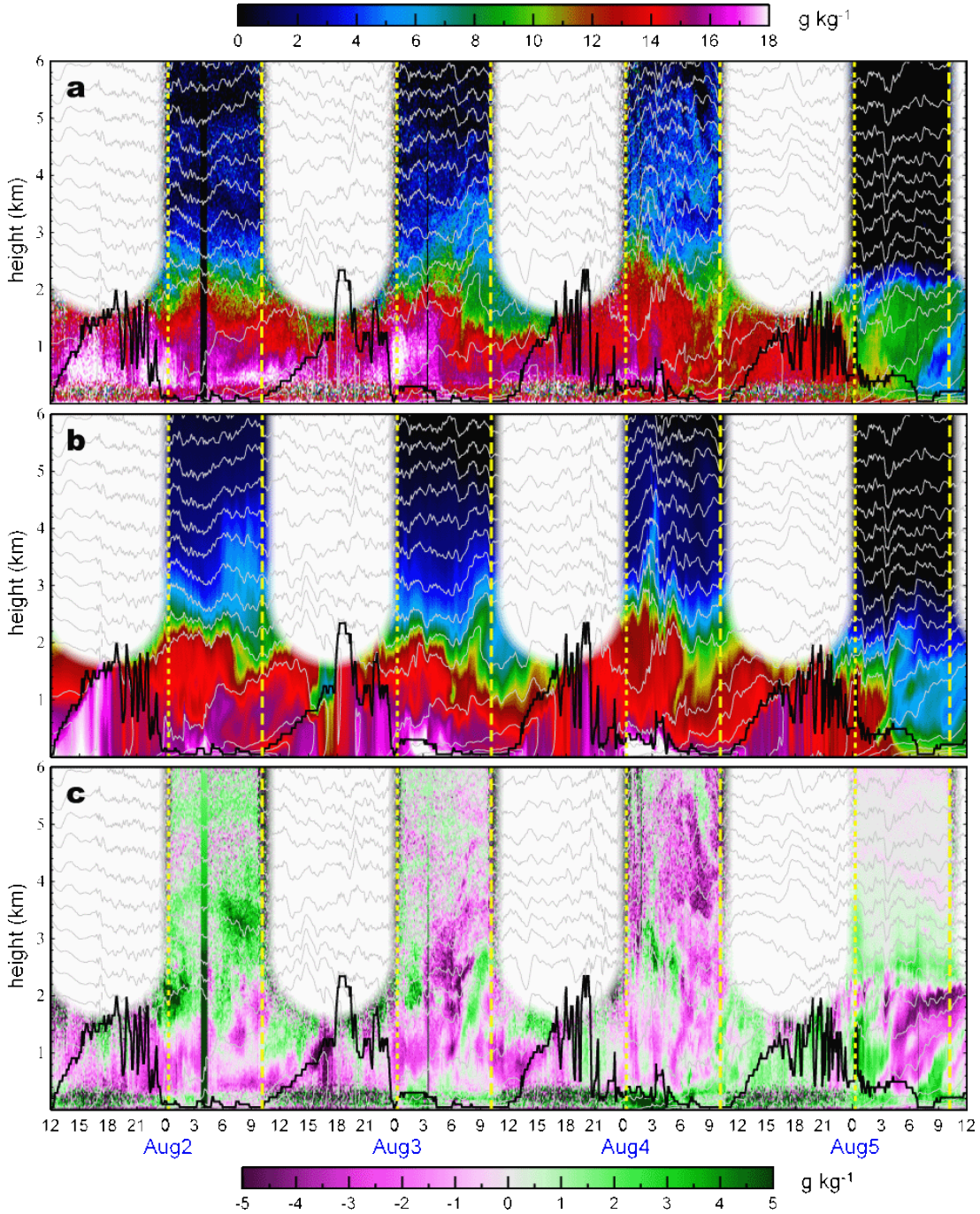


Figure 3.4: Observed (a) and control run (b) mixing ratio indicated by shading. Model error (c) from subtracting b from a. All units in g kg^{-1} . White areas mask out background noise during the daytime. Rest as in Figure 3.2.

3.2.3 Planetary boundary layer height

WRF estimates the planetary boundary layer height (PBLH) through feedback generated by one of several available boundary layer parameterization schemes. Sensitivity tests were conducted on this case study during the initial experimentation and it was found that the MYJ parameterization produced the best overall results from the model verification (Section 4.6). WRF-MYJ also represented the layers in the stratified prefrontal environment better than other PBL parameterizations.

The WRF-MYJ configuration estimates the PBLH to be where the turbulent kinetic energy (TKE) falls below a minimum threshold value ($0.005 \text{ m}^2\text{s}^{-2}$) but is not directly linked to temperature profiles (Shin; Hong 2011). This was evident by noting the oscillatory nature of the model PBLT between 0.5-2.0 km AGL from 1800-2300 UTC each afternoon (Figure 3.2). The seemingly whimsical vertical fluctuation of the model PBLT across a relatively invariant isentropic profile with respect to time demonstrates the weak linkage to temperature or atmospheric homogeneity in general. The terms which typically dominate and govern the TKE equation are the mechanical and buoyant production/consumption of kinetic energy. In the absence of significant vertical shear (mechanical production) within the model's lowest 1.5 km, it is plausible that this behavior may be connected to the buoyant term. Intermittent cloudiness will influence the amount of surface heating which drives late-afternoon convective thermals that affect the production and consumption of total TKE.

The model PBLT (Figure 3.2b) was not consistent with the hypothesized PBLT (Figure 3.2a; placement same as in Chapter 2) during the early nocturnal period from 2300-0600 UTC. WAVES observations indicated that the PBLT was

located between two distinct homogeneous air masses with different wind regimes and slowly lowered throughout the early nocturnal period. By comparison, the model PBLT dropped sharply between 2200 UTC and 0000 UTC and remained, for the most part, under 100 m AGL until the CBL formed again after daybreak. The exceptions to this pattern were periods during the LLJ regimes of 3-4 August and the early nighttime of 5 August when the model PBLT rose briefly to a height of 400-500 m. The reason for the higher model PBLH during these hours was predominantly due to mechanical (shear) production of TKE associated with the low-level wind speed maxima. On the contrary, the PBLT remained low during the entire night of 2 August because low-level flows were weaker. It is curious to note that model PBLT did not rise during any DW regimes, which were also accompanied by low-level wind speed maxima capable of increasing the TKE, and thus the PBLT.

Since a higher nose height would form a weaker gradient of vertical shear between the surface and the wind speed maximum above, it would generate less mechanical TKE. Therefore, it is believed that the low model PBLT was attributed to the higher nose altitudes associated with the DW wind speed profiles (Figure 3.3c) versus the lower noses in the LLJ profiles (Figure 3.3a).

In spite of the aforementioned model shortcomings in correctly simulating the observed PBLT during late-afternoon and nocturnal periods, it was in agreement with daily observations from 0800-1800 UTC. The WRF-MYJ TKE method for PBLT estimation correlated most closely with observations during the late nocturnal period when the PBL was at a minimum height and during the early daytime periods as the CBL was developing in a mostly sunny environment.

3.3 Analysis of Regional Flow

The overall model comparisons with WAVES observations showed positive results, especially as verified against HUBC profile measurements, such as the LLJ and DW features which are the primary foci of this investigation. This provides enough confidence for us to use the model results to understand the three-dimensional structures and evolution of various observational events.

3.3.1 Horizontal evolution

Figure 3.5 shows wind direction data on a horizontal plane located at 500 m ASL from the nest domain. This height was selected to best illustrate the low-level wind speed maximum and wind direction shift observed at HUBC as depicted in Figure 3.3. The prefrontal days of 2-4 August were found to be very similar upon examination. Therefore, the IN212 run, which simulated the events during the nighttime of 3 August, was chosen to represent the nocturnal phenomena that occurred each night.

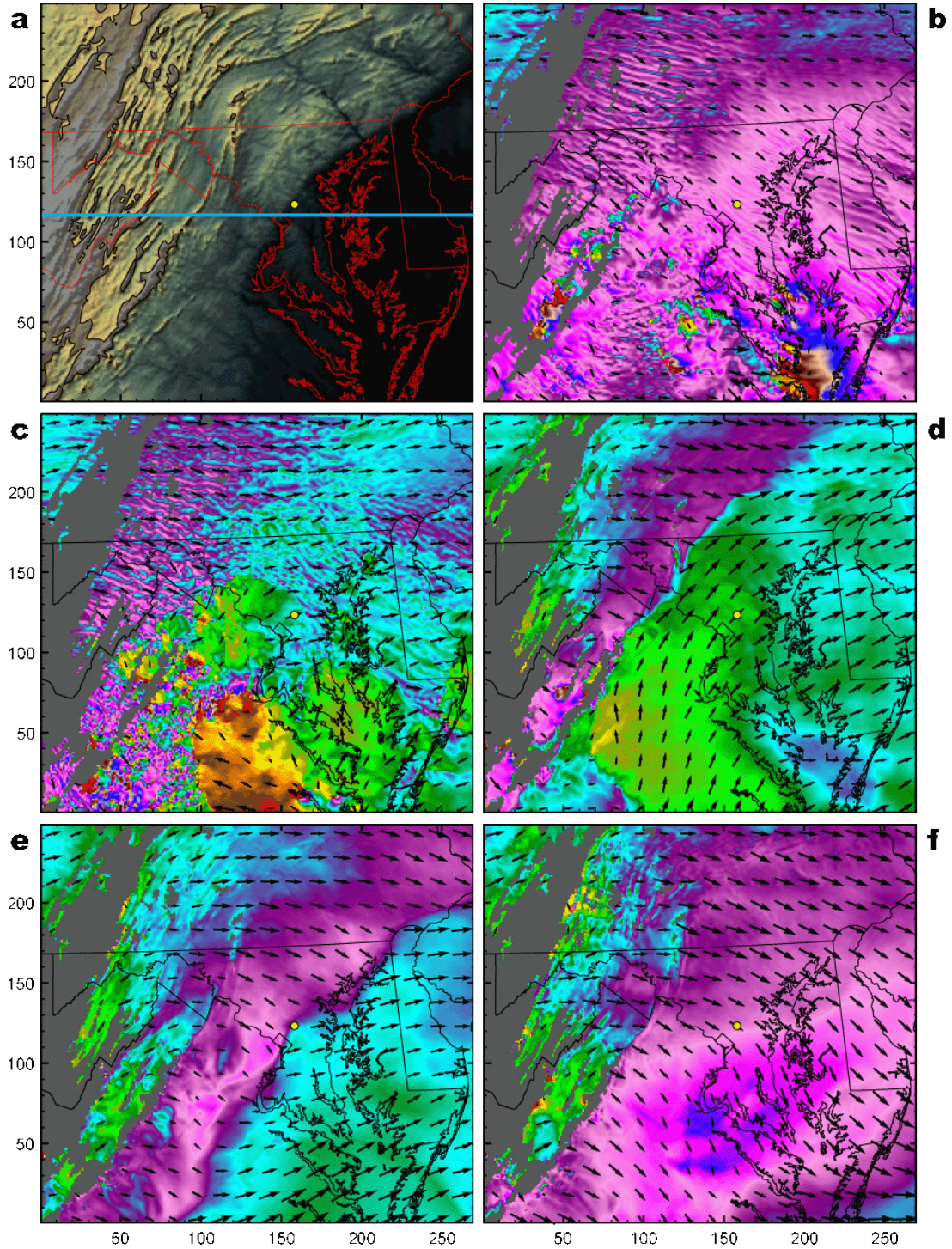


Figure 3.5: WRF wind direction at 500 m MSL. Gray areas indicate elevations exceeding the plane height, the yellow dot indicates the HUBC location, and terrain is shown in (a). Wind direction at times (b) 1730, (c) 2000, (d) 0100, (e) 0500, and (f) 0900 UTC show the diurnal transition of wind direction from northwesterly to southwesterly and back to northwesterly again. The blue line in panel (a) indicates the location of the vertical cross sections in Figure 3.6.

Figure 3.5a shows a snapshot at 2000 UTC (1600 LDT) in the afternoon when the wind field was transitioning from the northwesterly background flow to southwesterly wind. Throughout the late morning hours, the wind direction had been predominantly west-northwesterly (purple shading). After 1500 UTC, the developing CBL formed horizontal convective rolls (HCR) (Weckwerth et al. 1997) which emerged across the terrain. These HCRs, sometimes referred to as convective streets, had an axis oriented almost parallel to the prevailing northwesterly flow. They first appeared over areas where the surface heating was strongest, such as the eastern flank of the Blue Ridge Mountains, the Piedmont, and then the Eastern Shore. Regions located near water or within the Ridge and Valley region were slower to develop HCRs. The overall horizontal wind speed in the vicinity of the intensifying HCRs dropped from 5 m s^{-1} to near zero during 1500-2000 UTC. The calming horizontal winds were linked to increasing eddy viscosity generated by the HCR updraft and downdraft sectors. These convergent and divergent sectors along the HCR axis created rows of winds that were northwesterly and southwesterly and are easily identifiable in Figure 3.3a. Over time, the rows with southwesterly wind direction grew at the expense of the northwesterly rows. The HCRs appeared to facilitate a more rapid transition of the CBL to a southwesterly flow. The HCRs decayed quickly between 2200-2300 UTC and left a uniform southwesterly flow. For each of the three days on 2-4 August, the transition of the wind direction from northwest to southwest was most evident east of the Blue Ridge Mountains.

The transition of the wind direction from northwest to southwest progressed differently over open waters than on land. Over water, this transition occurred more

rapidly and there was little evidence of HCRs. The changing wind direction appeared to initiate near the mouth of the Chesapeake Bay. This location may be conducive to a rapid transition for a few reasons. First, these areas have the greatest ratio of water to land surface area. The effect may be a modulation of air temperatures over water which would modify local pressure gradients and thereby drive winds landward. This concept will be further discussed in the following sections. Secondly, the open water and coastal areas are relatively flat with minimal surface friction compared to the rougher terrain further inland. This may facilitate a more rapid response in the wind field to local environmental changes, such as pressure. Thirdly, the southern exposure of this region's location would experience any northbound air mass influx first. It is also true that this location is furthest removed from the influence of any lingering northwesterly flow associated with the morning DW regime.

Figure 3.5b shows the wind direction soon after sunset at 0100 UTC (2100 LDT). Daytime turbulent eddy viscosity had fully dissipated by this time and the wind speed (not shown) began intensifying out of the southwest. The flow pattern east of the Blue Ridge Mountains marks the developing LLJ regime. All three days show wind speeds increasing over the Piedmont Plateau and Fall Line first, then developing eastward across the Eastern Shore as the nighttime progressed. The western edge of the LLJ regime never extended past the Blue Ridge Mountains for 2-4 August. In fact, these mountains acted as a barrier upon which a sharp contrast in low-level wind direction was established, with northwesterly flow to the west and southwesterly flow to the east. This wind direction interface set up much further east

on 4 August due to a stronger DW regime after the passage of the prefrontal trough. The stronger DW event curtailed maturation of the LLJ regime.

The eastward progression of the DW over the HUBC site was captured in Figure 3.5c at 0500 UTC (0100 LDT). The sharp horizontal interface is evident between the northwesterly flow of the DW regime (purple shading) and the southwesterly flow of the LLJ regime (green shading). During the preceding hours, the interface progressed steadily southeastward away from the Blue Ridge Mountains, where it had originally formed. The model timing of the DW passage over HUBC agreed well with observation data. The shape of the horizontal wind direction interface varied slightly each night. On 3 August, the interface was characterized by a wavy appearance, as indicated by Figure 3.5c. A review of the image sequence (not shown) leading up to this time indicates that the more ragged appearance of the interface was produced by convective outflows earlier in the day. By comparison, the interface on 2 August was more linear and crisp, stemming from a late-day environment lacking significant convection and outflows, and hence, was relatively uniform. The nighttime events of 4 August were, perhaps, the most interesting of the three days. They corresponded with the passage of a prefrontal trough (earlier at 2100 UTC 3 August) that was followed by a wind shift which persisted across the Mid-Atlantic until the arrival of the cold front (2200 UTC 4 August). These synoptic events greatly amplified the DW regime on 4 August. Earlier that night, near sunset, the westernmost extent of the developing LLJ regime was offset about 40 km west of the Fall Line, but closely followed this geographic feature throughout the Mid-Atlantic region. This setup meant that the interface between the DW and LLJ regimes

were not parallel to the Blue Ridge Mountains but instead bulged eastward in Northern Virginia where the Fall Line was located. The initial transition to the DW regime at HUBC occurred earlier around 0400 UTC. Unlike the previous nights, however, a faster propagating low-level flow was observed moving southward, crossing the Maryland-Pennsylvania line at 0530 UTC. This unexpected air mass was linked to simulated (and observed) precipitation in north central Pennsylvania (Chapter 2, Figure 2.2c) where cooler air in the vicinity of the frontal boundary was tapped into and then forced southward in the form of thunderstorm outflows. The arrival of this outflow at HUBC was nearly coincident with the DW around 0700 UTC. The unusually strong DW appearance in HUBC observations on 4 August was this second reinforcing flow, which rendered a visually striking displacement curl in the lowest kilometer as the incumbent air mass was lifted and pushed away horizontally.

Figure 3.5d shows the Mid-Atlantic region an hour prior to dawn at 0900 UTC (0500 LDT) 3 August. The wind direction was predominantly northwesterly east of the Blue Ridge Mountains in the wake of the DW passage. This was also the case for the other two days at this time period. There were a few pockets of northerly flow amidst the prevailing northwesterly winds which were mainly located around the southern neck of the Potomac River, whereby the background flow curved to follow the lower terrain of the river valley. The regions west of the Blue Ridge Mountains remained relatively unchanged throughout the duration of these nocturnal events.

3.3.2 Vertical structure

With a better understanding of the spatial extent of the DW and LLJ events, the vertical structure and evolution of these features are explored in this section. Figure 3.6 shows the vertical structure (east-west) of the atmosphere from the period of maximum daytime heating to maximum DW on 3 August.

Higher equivalent potential temperature (θ_e) values were found east of the Blue Ridge Mountains (Figure 3.6a). Elevated levels were linked to areas near water bodies where evaporated moisture was abundant. Potential temperature (θ) contours exhibited the opposite pattern, with lower values located nearby or downwind of water bodies which were cooler than the surrounding land. The 500 m ASL distribution of temperature and density (not shown) generated a baroclinic field that is characteristic of sea breezes. Therefore, it is hypothesized that the low-level propagation tendency facilitated the westward expansion of southwesterly winds leading up to the LLJ regime. This is consistent with the evolution of the wind direction field which showed that the origins of the transitioning southwesterly flow were located near the western shores of the Chesapeake Bay and migrating westward with time. Not all model grid points near water exhibited an easterly wind component, but the wave-front propagation clearly moved from east-to-west even if the flow was transverse.

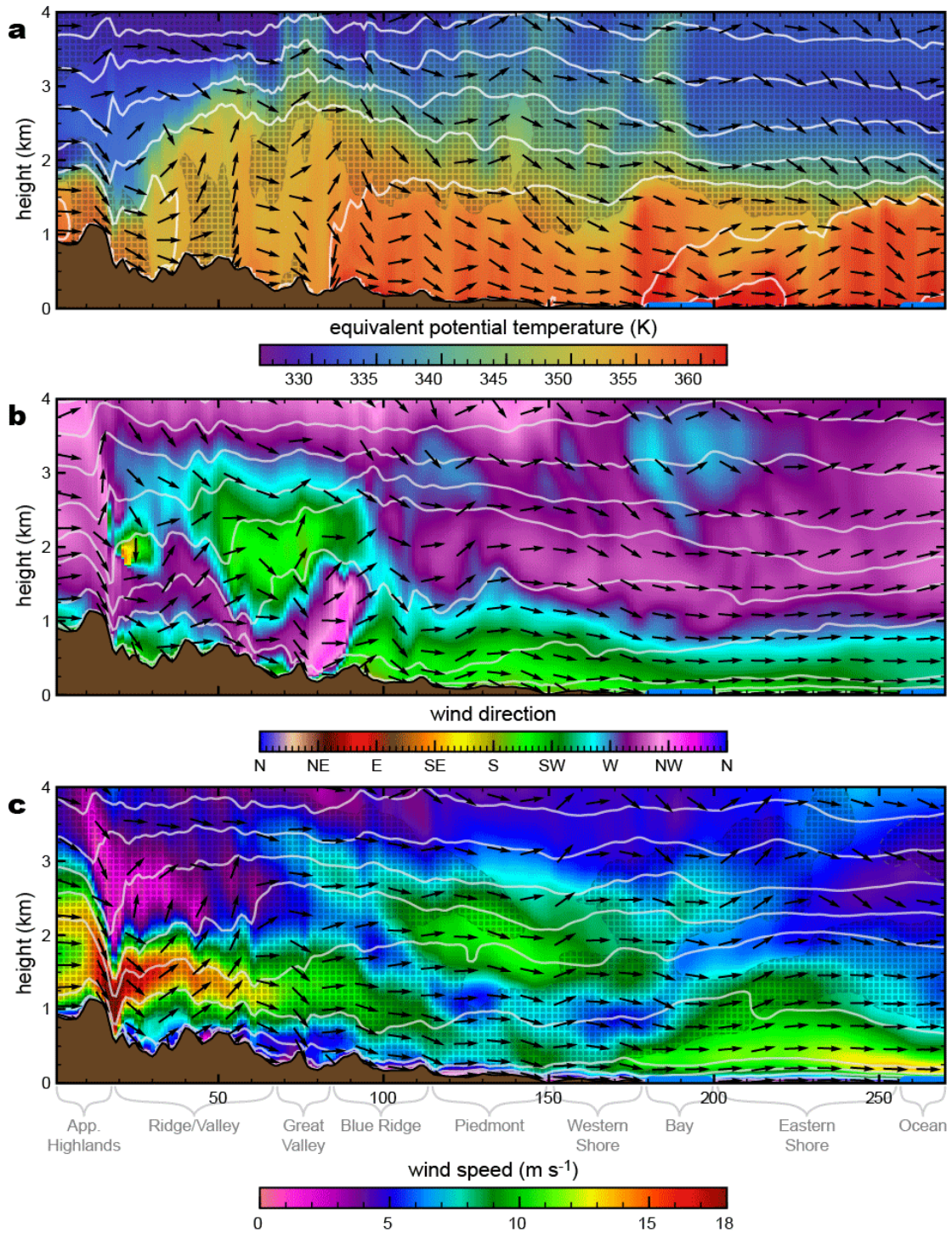


Figure 3.6: Vertical cross sections from D2 of run IN212 located along the cyan line marked in Figure 3.5a. Shaded areas show (a) θ_e at 2200 UTC 2 Aug, (b) WDIR at 0100 UTC 3 Aug, and (c) WSPD at 0600 UTC 3 Aug. Contours indicate θ spaced every 2 K with a white line every 10 K. Vectors represent U-W components of wind on a vertical plane. Solid brown is the surface terrain and the blue lines on top show the location of water bodies. Hatched pattern indicates areas with positive V-wind.

The regions to the west of the Blue Ridge Mountains were warmer and dryer than those to the east (Figure 3.6a). The Ridge and Valley and Great Valley regions showed a virtually uniform potential temperature profile up to 2.5 km ASL, indicative of a well mixed PBL that may have been enhanced by turbulent eddies forced by differential heating of orographic slopes and air motions over the terrain. This region also had the weakest horizontal winds of 1-4 m s⁻¹ which extended all the way up to 2.5 km. The effect of the viscous afternoon CBL was to nurture the development of low-level flows, such as the sea breeze phenomenon or the southwesterly winds, by shielding them from the shear of the strong northwesterly flow aloft.

Wind direction data are plotted in Figure 3.6b at 0100 UTC (2100 LDT) 3 August, roughly an hour after sunset. By this time, the vertical spacing of θ contours in the lower atmosphere began tightening over the Ridge and Valley region, which is indicative of increasing nocturnal stratification. The decaying PBL in the higher elevations no longer provided sufficient eddy viscosity to resist the impinging laminar flow, particularly down the eastern slopes of the Appalachian Highlands where there was a propensity for high wind speeds generated by a standing mountain wave, clearly seen in Figure 3.6c. The return of strong low-level flows near the surface was most evident by an intrusion of northwesterly flow (purple shading) located near the surface over the Ridge and Valley region. This tongue of northwesterly flow was the DW regime. An animation of the wind direction field reveals the eastward progression of the DW with a bore-like appearance and behavior. Prior to 0100 UTC 3 August, the leading edge of the DW was associated with cooler θ contours (not shown). After 0100 UTC, rapid radiational cooling within the mountain regions

obscured the horizontal temperature gradients that were associated with the DW head. The position of the DW head in Figure 3.6b can be compared with the horizontal plane in Figure 3.5b. The location of DW boundary at 0100 UTC was just west of the Blue Ridge Mountains. This feature continued progressing eastward with a stream of northwesterly wind flow in its wake.

A high speed jet of northwesterly air flow was trailing behind the DW head over the mountain terrain as evidenced in Figure 3.6c at 0600 UTC (0200 LDT) 3 August. Concurrently, high wind speeds associated with the LLJ regime were identified over the Eastern Shore. Surface wind speeds were relatively calm at the interface between the two regimes. An animation of wind speeds throughout this period shows the DW intensifying and expanding eastward until 1000 UTC (0600 LDT) 3 August. After this time, the DW wind speed intensity started to wane from west-to-east. CBL growth began after dawn and, over time, lifted the layer of high winds ovetop of the growing PBL beneath. This elevated jet was most evident over the CBL during the late morning period and diminished after 1500 UTC (1100 LDT).

3.4 Contributions to Nocturnal Downslope Winds

While the previous discussion diagnosed the evolution and structure of nocturnal low-level winds in the Mid-Atlantic during this case study, the origin of the DW was not discussed. The focus moving forward is to identify possible mechanisms behind the DW regime and its interplay with other regional circulations.

3.4.1 Cross-Appalachian wind flow

It is believed that the recurring nighttime DW was the result of leeside mountain waves that were formed by the cross-barrier wind flow over the Appalachian Mountains, but governed by the diurnal cycle of surface heating (turbulence) and cooling (stratification). During the daytime, the CBL kept the lower atmosphere relatively well-mixed with calm wind speeds. During this period, the mountain waves had a small amplitude and remained above 2 km. As the daytime surface heating waned, the atmosphere became more stable and the PBL collapsed. This was accompanied by a gradual descent and amplification of the lee wave, which led to increased wind speeds down the east flank of the mountains. These findings are consistent with the idealized simulations of Smith; Skillingstad (2011) which showed the reemergence of a downslope jet when transitioning from surface heating to cooling. Cooler and drier air, which was located near 2 km MSL above the Appalachian highlands, was advected into the lee waves and forced down the slopes as a jet until a hydraulic jump which appeared near the Blue Ridge Mountains. Over time, the effect of the DW was to displace and dilute, through turbulent mixing, the existing air mass east of the Appalachians. It is hypothesized this is the reason the DW appeared more diffuse and lofted (~0.8 km) compared with traditional drainage flows. However, without further experiments it is unclear to what extent katabatic forcing may have accelerated the winds.

3.4.2 Prefrontal LLJ

While mountain waves played a central role in the generation of the DW each night, not all nights showed the same core wind speeds. It is believed this is a result

of the upstream conditions (relative to the barrier). The following description of 3 August shows why the DW wind speeds increased ahead of the cold front and their relationship to the low-level winds in the Midwest.

The broader meteorological context of the 3 August nocturnal period is illustrated in Figure 3.7 showing a snapshot at 0500 UTC 3 August from the outer domain of run IN212. Panels d and e show the wind speed and direction, respectively, from a horizontal plane located at 600 m ASL. A sharp transition between northwesterly and southwesterly winds in the Midwest identified the location of the cold front (Figure 3.7d). A similar transition in wind direction was evident immediately east of the Appalachian Mountains, which was the advancing DW regime moving down the eastern flank of the mountains. This supports the claim that the DW event was not a local phenomenon, but evident up and down the Appalachian Mountain chain from New Jersey to Alabama. Ahead of the cold front was a stream of high speed southwesterly winds that exceeded 20 m s^{-1} (Figure 3.7e). This appeared like the Great Plains LLJ but was actually a prefrontal LLJ enhanced by the thermal wind ahead of the cold front boundary. A time series of the low-level wind speed in the Midwest shows that relatively calm conditions persisted throughout the afternoon but increased after sunset.

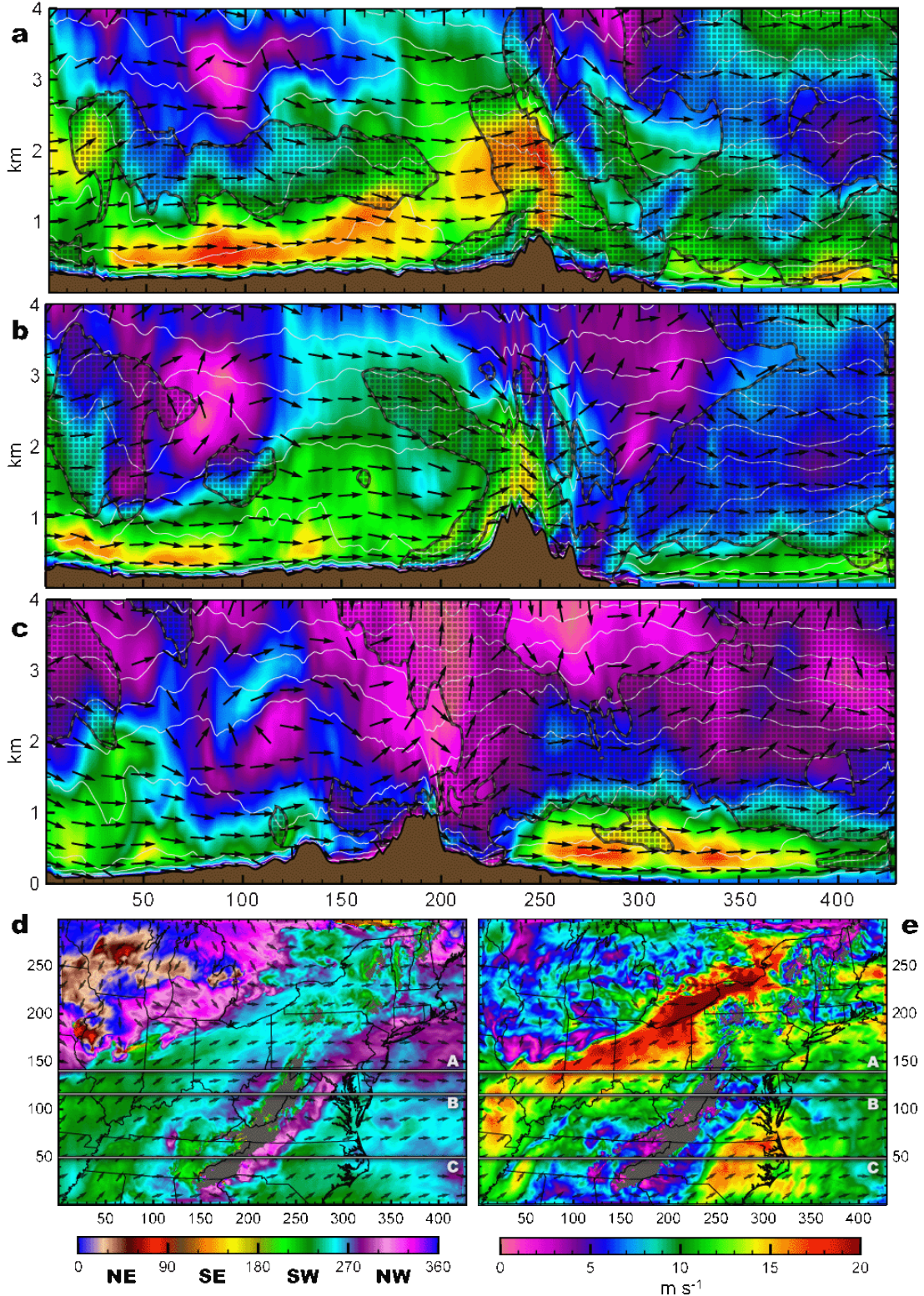


Figure 3.7: WRF output at 0500 UTC 3 August for D01. Horizontal 600 m MSL planes show (e) WSPD and (d) WDIR. Lines [A,B,C] in panels (d-e) show the locations of the vertical cross sections (a,b,c), respectively. WSPD (shading), θ (contours), and positive V-wind (hatching) is shown in panels (a-c).

Figure 3.7a-c show vertical cross-sections of wind speed from north to south, positioned according to the horizontal lines in Figure 3.7d,e. High wind speeds below 1.5 km are evident west of the Appalachian Mountains (Figure 3.7a-c). The horizontal plots reveal that the axis of the prefrontal LLJ was not parallel with the Appalachian Mountains but rather formed an acute angle with the mountains such that the prefrontal LLJ outflow impinged upon the western slopes. This orientation led to higher wind speeds on the western slopes of the Appalachians in locations further north (Figure 3.7a-c) which were closer to the LLJ axis. A large portion of the prefrontal LLJ outflow skirted the Appalachian Mountains and was channeled through the lower elevations across Lakes Erie and Ontario. However, a significant amount of the outflow was forced up the windward side of the mountains, crested, and then flowed down the eastern flanks. It is believed that this mass-flux across the mountains caused a low-level stream of air to flow down the east side of the mountains in the form of the DW.

WRF and satellite observations during the afternoon hours showed broad areas of convective cloud cover with isolated areas of precipitation along the western slopes of the Appalachian Mountains. Any areas of convective precipitation, which were triggered by orographic lifting in a conditionally unstable afternoon CBL, meant that ascending air underwent moist adiabatic processes that effectively dried the cresting air mass. Cloud cover waned after sunset but left a region of drier, denser air immediately east of the Appalachian Highlands. This airflow continued moving eastward over the crest and was vertically constricted by a standing mountain wave that forced subsidence down the eastern flank of the mountains (Figure 3.6) and

formed a well-defined DW regime. This low-level flow was propelled down the eastern flank by density and mass-flux from the Midwest LLJ outflow.

An examination of the θ evolution did not reveal any significant warming associated with lee subsidence. Even though the Appalachian Mountains have relatively low elevation profiles compared to many larger mountain ranges, it was expected that the vertical drop would be sufficient to increase the temperature by a few degrees following a dry adiabatic descent. It is hypothesized that this could be partially offset by stronger radiational cooling in higher elevations. This is based upon the model's total column precipitable water vapor field (not shown) which indicated very large differences, occasionally exceeding 30 mm, between the dry columns over the mountain regions and moist atmosphere over lower elevations, especially in locations east of the Blue Ridge Mountains situated near abundant water bodies. This relative pattern was semi-permanently located throughout the prefrontal period. Additionally, the mountain regions were mostly cloud free during the nighttime periods. It is expected that the effect of a reduced water vapor field above higher elevations would allow a more rapid cooling of near surface air than lower elevations, since water vapor is the atmosphere's principal greenhouse gas. It is believed that this disproportionate cooling rate could have modulated heat gained through subsidence as the DW progressed downward, resulting in katabatic flow without significant warming. A more detailed analysis of the DW thermodynamic properties would be needed to quantitatively confirm this hypothesis.

3.4.3 Potential vorticity

The nightly prefrontal flows occurred under a persistent high-pressure region that was situated over the southern Appalachian Mountains. The area of high pressure provided a background of anticyclonic flow that coaxed Midwestern air over the Appalachian Mountains into the Mid-Atlantic from the northwest. The high pressure region also created a layered environment that tended to confine the vertical extent of low-level flows. Assuming a mostly isentropic nocturnal flow, air traversing the Appalachian Mountains gains negative (positive) potential vorticity at the crest (lee side) regions according to Ertel's potential vorticity equation (Holton 2004):

$$1) PV = -g(\zeta_{\theta} + f) \frac{\delta\theta}{\delta p}$$

which when simplified to a homogeneous incompressible fluid becomes

$$2) PV = const = \frac{(\zeta + f)}{H}$$

where g is gravity, p is pressure, f is the Coriolis force, ζ_{θ} is relative vorticity following an isentropic surface, and H is the height of a column of air. It is seen from equation (2) that when a column of westward moving air is stretched (shortened) over the mountain leeside (crest), there must be a compensating increase (decrease) in relative vorticity leading to a southward (northward) displacement of a parcel's horizontal trajectory in order to conserve PV. Returning to the more realistic approximation of isentropic flow, the wide spacing between the potential temperature contours in the lowest 2 km to the east of the Appalachian Mountains (Figure 3.7a-c) indicates vertical stretching downstream of the mountain wave near the hydraulic jump which must also generate positive vorticity based on equation (1). The net result

produces a semi-permanent lee trough. The geostrophic flow around the lee trough is closely correlated with the northwesterly (southwesterly) winds to the west (east) of the lee trough axis, and facilitates the sharp change in wind direction at the interface between the DW and LLJ regimes.

3.4.4 Influence of mountain height

The height of the Appalachian Mountain barrier in runs IN212H and IN212L affected the low-level winds. Comparisons showed that the Midwest prefrontal LLJ outflow had greater difficulty traversing the steeper terrain in IN212H. As a result, the leading edge of the DW on the Appalachian's east side that was less linear and more distorted, reflecting a slower progression of winds across the taller peaks and a faster progression of the DW through mountain gaps and valleys. The DW wind direction showed a stronger northerly component than the control run. The vertical structure of the DW wind speed was shallower in runs with higher terrain compared with the control run, with values exceeding 20 m s^{-1} instead of 17 m s^{-1} , respectively. Unlike the other runs, IN212L did not exhibit a crisp wind direction boundary between the DW and LLJ regimes. Additionally, the DW wind direction in run IN212L was more westerly than the control run. The reduced mountain heights led to a broader area of high wind speeds associated with the prefrontal LLJ. However, run IN212H and the control run showed more intense wind speeds across Lake Erie where winds were channeled around the mountain barrier.

The mountain height also affected the LLJ regime east of the Appalachians. Run IN212H showed a much stronger Mid-Atlantic LLJ with core wind speeds reaching 20 m s^{-1} . By comparison, the wind speeds in run IN212L were only half that

strength. The run with higher mountain heights filled in the horizontal distribution of the Mid-Atlantic LLJ wind speed, eliminating the more gusty appearance characterizing the LLJ regime in the other two runs. The LLJ regime of IN212H was thicker with higher wind speeds than the other runs. This was the opposite relationship compared to the DW flow where thinner layers showed higher wind speeds.

3.5 Daytime Solenoidal Forcing

Many elements of the mountain-plains circulation discussed by Wolyn; McKee (1994) are realized in this case study, including the downslope jet (which we referred to as the DW regime), leeside convergence zone, the cold core, and migrating solenoid. Figure 3.8 shows WRF data from runs IN212H, IN212, and IN212L on the evening of 2 August at 2300 UTC. The coordinate system in these graphics was rotated so that the x-axis was aligned perpendicular to the Appalachian Mountain barrier. Therefore, the U-component of wind represents cross-barrier flow in the Mid-Atlantic. Figure 3.8 illustrates how barrier height affects the Mid-Atlantic solenoidal circulation.

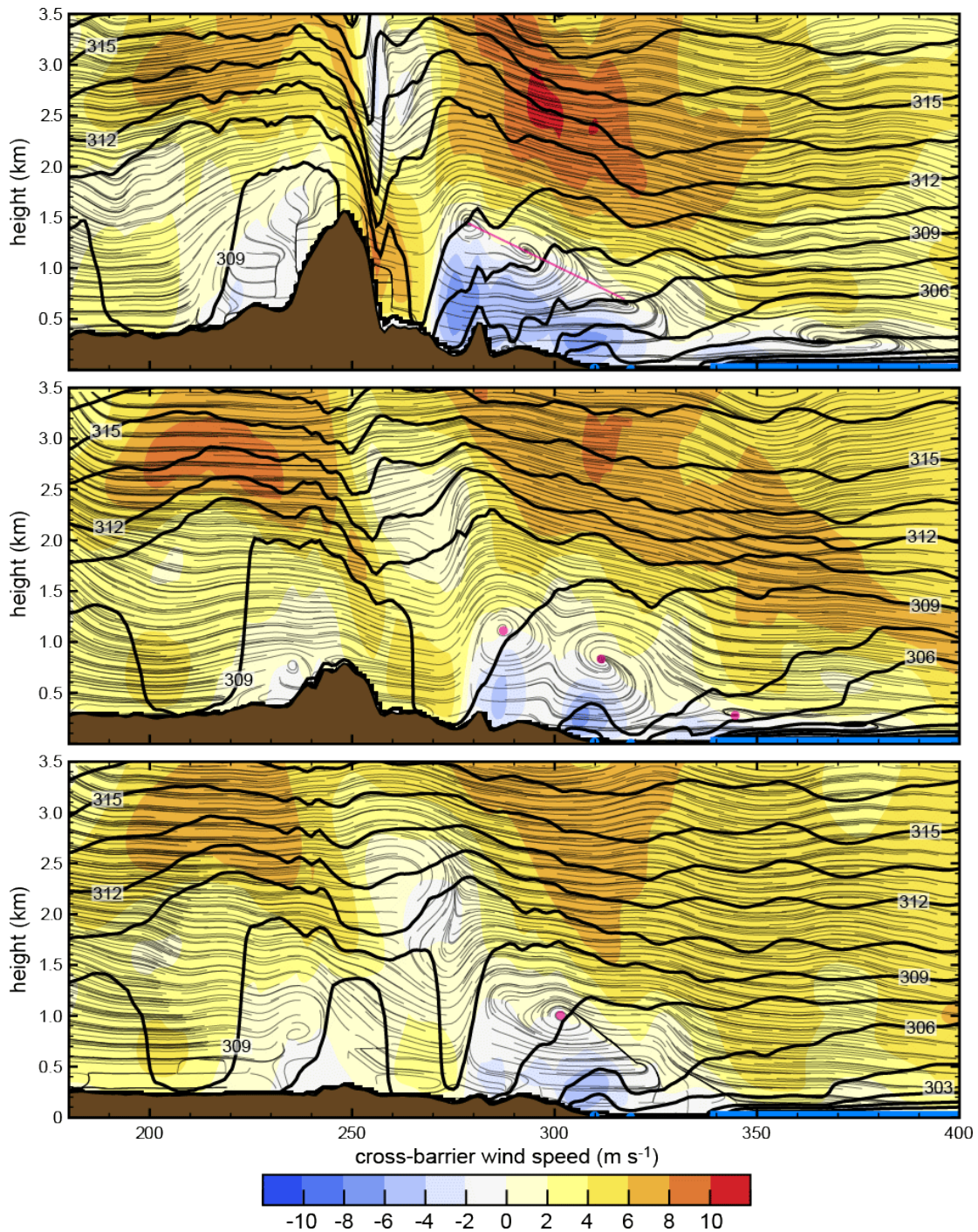


Figure 3.8: Panels (a-c) show model output from runs using 200% (Figure 3.1c), 100% (Figure 3.1a), and 40% (Figure 3.1b) Appalachian Mountain height. The simulation time is 2300 UTC 2 August. The x-axes extend from the Ohio-Indiana-Kentucky border to the Atlantic Ocean. Shading shows the cross-barrier wind speed whereby warm (cool) colors indicate positive (negative) west-to-east (east-to-west) flow over the mountains. Contours show θ and streamlines show the wind field on the vertical plane. Magenta dots (lines) reveal the centers (axis) of circulation about the leeside solenoids.

The overall solenoidal circulations are discerned by examining the wind fields in Figure 3.8. The circulation shape and center are different in all three runs. Figure 3.8b uses black dots to designate 3 distinct circulation centers in the control run. Run IN212L, with reduced terrain heights, shows a single main circulation center located on the Fall Line (Figure 3.8c). On the other hand, run IN212H, with increased terrain heights, shows a broader axis of rotation designated by a magenta line in Figure 3.8a. A comparison between the panels demonstrates that higher terrain elevations generated a more vigorous solenoidal circulation, as evidenced by the stronger toward-barrier (away-from-barrier) wind speeds below (above) the centers of circulation (Figure 3.8a). The U-wind magnitudes were greatly reduced in the run with flattened topography (Figure 3.8c). The leeside convergence zone was located in roughly the same location for all runs, which was immediately west of the Blue Ridge Mountains. Here, warm air from intense inland surface heating converged, ascended, and then deformed the isentropes into a cold core above 2 km. The cold core created a slightly higher pressure than its surroundings which, in combination with prevailing westerlies, generated an eastward flow aloft. Eventually this flow descended over the Eastern Shore. Cooler, denser surface air over watery regions drove a westward flow beneath the center of the solenoid.

The 3 smaller solenoids in the control run (Figure 3.8b) were located: east of the Blue Ridge Mountains, east of the Fall Line, and over the Eastern Shore. They each corresponded to toward-barrier surface wind speed maximums. Each successive solenoid contributed to the overall westward advection of cooler surface temperatures toward the Appalachians.

The solenoid produced by run IN212H (Figure 3.8a) did not have a distinct circulation center but rather showed a general circulation around an elongated axis. The axis slope was nearly parallel to the mean surface height. By comparison, the solenoid in run IN212L (Figure 3.8c) showed only one circulation. The center of this circulation developed above the Fall Line.

Solenoids in all 3 runs developed near strong temperature gradients over upslope terrain. These upslope regions were located along topographic boundaries between major geographic features in the Mid-Atlantic. In all runs, the solenoids migrated westward throughout the afternoon. The solenoidal circulations facilitated the transition of the PBL to a regime favorable for the LLJ, by directing the low-level winds toward the mountain barriers located to the northwest of the Mid-Atlantic. This expanded the pre-LLJ environment westward and reversed the Y-component of winds to be more southerly. The solenoidal circulations quickly dissolved after sunset, when daytime surface heating ceased. Without surface heating, the ascending branch of the circulation diminished and low-level toward-barrier winds vanished. Then, the overall PBL began to collapse. Concurrently, near 0100 UTC, the tongue of the DW had propagated down the Ridge and Valley region and arrived immediately west of the Blue Ridge Mountains, the same location as the disintegrating lee convergence zone. The decaying solenoidal circulation halted the westward progression of the LLJ regime, and permitted the erosion of the PBL by the DW propagating eastward. A time sequence of the model output for this period (not shown) revealed positive cross-barrier winds that abraded the solenoid from above, starting from the west. By 0300 UTC, any remaining toward-barrier winds had been greatly weakened and relegated

to the lowest 200 m AGL above the eastern coastal regions. By late night, the solenoidal circulations were completely eroded by cross-barrier winds associated with the DW regime, which dominated the lowest 2 km.

The development of the thermal field, which drove the Mid-Atlantic solenoid, occurred from different mechanisms than the Rocky Mountain-plains solenoid. In the Rockies, Wolyn; McKee (1994) argued that the eastern slopes were partially warmed by the subsidence of a downslope jet and by receiving high solar insolation directly upon dry soil during the morning hours. This generated a sensible surface heat flux which later organized into a thermal chimney over the mountains (Bossert 1997; Helfand; Schubert 1995; Jiang et al. 2007). Unlike the Rockies, the eastern slopes of the Appalachian Mountains have a more gradual slope with moister soil. These conditions, along with much lower mountain prominence, diminish any potential temperature gradients between the slopes and flatlands that would be comparable to the Rockies. Instead, the Mid-Atlantic temperature gradients were maintained by a surface heating differential. Coastal regions were well-modulated by the thermal momentum of nearby water bodies, while inland areas heated rapidly under mostly clear daytime skies that were compounded by the urban heat islands of the megalopolis. The surface heating contrast of land versus water was the primary reason for the amplified daytime temperature gradients between the slopes and flatlands, which led to the development of the Mid-Atlantic solenoid. The Mid-Atlantic solenoid typically reached maturity around 2300 UTC, when the maximum sensible heat differential existed. By comparison, the mountain-plains solenoid of the Rocky Mountains typically peaked earlier in the daytime, following the maximum

solar insolation on the eastern face of the mountains slopes. In essence, the Mid-Atlantic solenoid is conceptually a hybrid between a mountain-plains and sea breeze circulation.

3.6 Thermal forcing

3.6.1 Warm air anomaly

The thermal field in the lower atmosphere also influenced the low-level wind patterns. Figure 3.9a shows the model output at 1500 UTC 2 August over the Mid-Atlantic region. There was a trough positioned from coastal North Carolina up through the Northeast along the Atlantic shores. The height trough appears to be partially controlled by a warm temperature anomaly in the lower atmosphere (intersected by the 500 m ASL plane in Figure 3.9), and partially related to the leeside trough produced by flow conserving potential vorticity. The prevailing wind at this level was westerly. However, the high mountains in the eastern part of West Virginia partially blocked the westerly flow traversing the Appalachian Mountains. This produced a horizontal eddy-like feature located over west-central Virginia in the lee of the Blue Ridge. As a result, the eddy region was predisposed to a local buildup of heat later in the afternoon from the stagnant air and a weak wind field that did not ventilate as efficiently as the surrounding Piedmont regions to the north and south. At this time, the wind direction was northwesterly at HUBC, which was consistent with WAVES observations during the late morning hours.

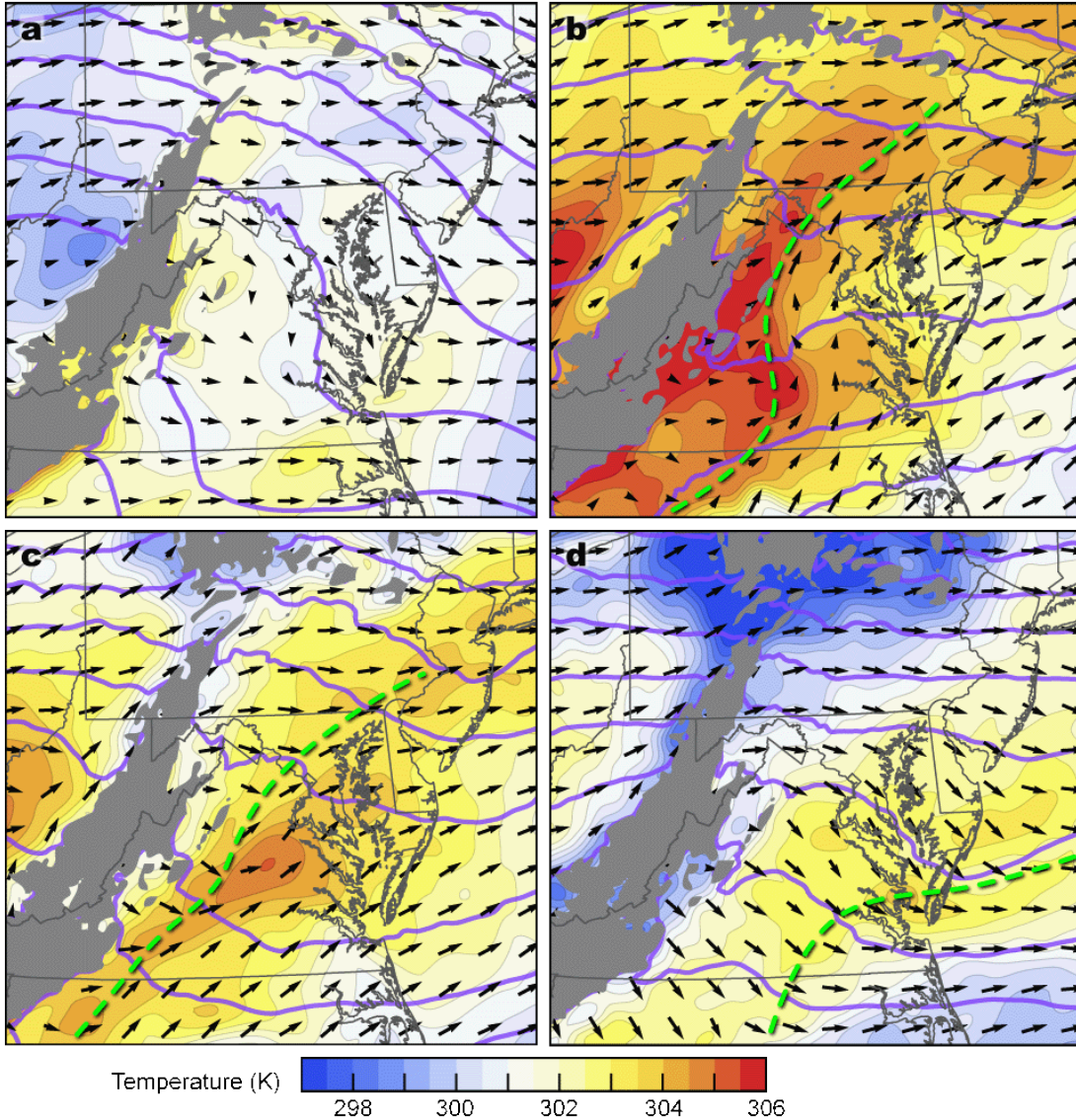


Figure 3.9: Horizontal planes at 500 m ASL which show temperature (shading), geopotential heights (contours), and wind vectors at (a) 1500 UTC 2 Aug, (b) 2300 UTC 2 Aug, (c) 0300 UTC 3 Aug, and (d) 1000 UTC 3 Aug. A green dashed line marks an abrupt change in wind direction, and usually correlated with the lee trough. Geopotential heights were smoothed using a Gaussian filter with a temporal window of 2 h and a spatial radius of 10 km to eliminate noise from high-frequency waves. Wind data were smoothed spatially using the same technique. No vertical smoothing was applied

By 2300 UTC 2 August, daytime surface heating had significantly raised the temperature on the 950 hPa plane (Figure 3.9b). The height trough migrated west toward the eastern flank of the Appalachian Mountains where the warmest areas were located. To the east of the wind-shift line, the flow was becoming southwesterly

preceding the LLJ regime. Earlier in the day, that region was characterized by slower horizontal wind speeds that allowed a strong ageostrophic (cross-isohypsic) flow. The slight southwest-northeast orientation of the isohypses to the east of the trough axis directed the ageostrophic wind component northward toward lower heights. This low-level pattern was the impetus for the LLJ regime over the coastal regions. To the west of the wind-shift line, the flow remained calm and disorganized across the Great Valley and portions of the Piedmont Plateau south of Pennsylvania.

Overall air temperatures at 950 hPa had begun cooling (Figure 3.9c) but there was a residual band of warm air, as indicated in Figure 3.9b, located along the trough axis. This warm band had advected eastward by the prevailing westerly flow, and the trough axis also tracked east, accordingly. The wind-shift line was located slightly to the east of, but parallel to, the Blue Ridge Mountains at 0300 UTC. Regions to the east of the wind-shift were strongly influencing by the LLJ winds, including the HUBC site. To the west of the wind-shift line, a strong northwesterly flow associated with the DW regime began displacing the warm anomaly, the isohypsic trough, and the LLJ regime off to the east.

Shortly before dawn the DW regime had propagated much further east so that the leading edge was positioned along the wind-shift line (Figure 3.9d). The airflow over much of the Piedmont Plateau was northwesterly and oriented orthogonal to the mountain barrier. Radiational cooling strongly influenced the air temperatures in the higher mountain elevations. The warm band could still be discerned at this time although it had a more muted appearance from continued cooling and dissipation. The band and trough were located much further east near the coast, almost in the same

position as in Figure 3.9a. What remained of the LLJ regime was relegated to the far southeast corner of Figure 3.9d and those winds had become increasingly westerly following the rotation about the inertial oscillation.

3.6.2 Thermal wind

The differential heating across the Mid-Atlantic region greatly impacted the low-level winds as illustrated by the time lapse of temperatures in Figure 3.10a. Maximum inland temperatures peaked around 2100 UTC and fell to a minimum around 1200 UTC the following morning. Tangents to the isotherm curves associated with these two temperature extremes (Figure 3.10a) have slopes with opposite signs, and appear to pivot about a region with a tight consensus among the isotherms located immediately above the water bodies. Compared to inland regions, the air above the coastal areas maintained more consistent temperatures around the clock through the thermal inertia of the Chesapeake Bay and Atlantic Ocean. The tilting of isotherms with time across the 950 hPa surface indicated a changing baroclinicity. This baroclinicity implies the existence of a thermal wind. The meridional component of the thermal wind (V_T) is estimated by

$$v_T = \frac{R}{f} \frac{\partial}{\partial x} (\Phi_1 - \Phi_0) \approx \frac{R}{f} \left(\frac{\partial \langle T \rangle}{\partial x} \right)_p \ln \left(\frac{p_0}{p_1} \right)$$

where layer thickness is proportional to the mean temperature $\langle T \rangle$. The isotherms during late afternoon and early nighttime (2000-0100 UTC) showed an overall negative slope, implying that the thermal gradient along the x-direction made the right hand side of the thermal wind equation negative; thus, V_T was generally directed southward. The isotherms during the late nocturnal period and morning hours (0300-

1200 UTC) showed an overall positive slope, implying V_T was directed northward. The result implies that the thermal wind assisted (hindered) the DW (LLJ) regime during the early nighttime period, and likewise, assisted (hindered) the LLJ (DW) regime during the late nocturnal period. It should be emphasized that these types of low-level flows are very loosely constrained to be isentropic and become even less valid during the daytime CBL. However, the main point is to assert the potential impact of low-level baroclinicity on flows.

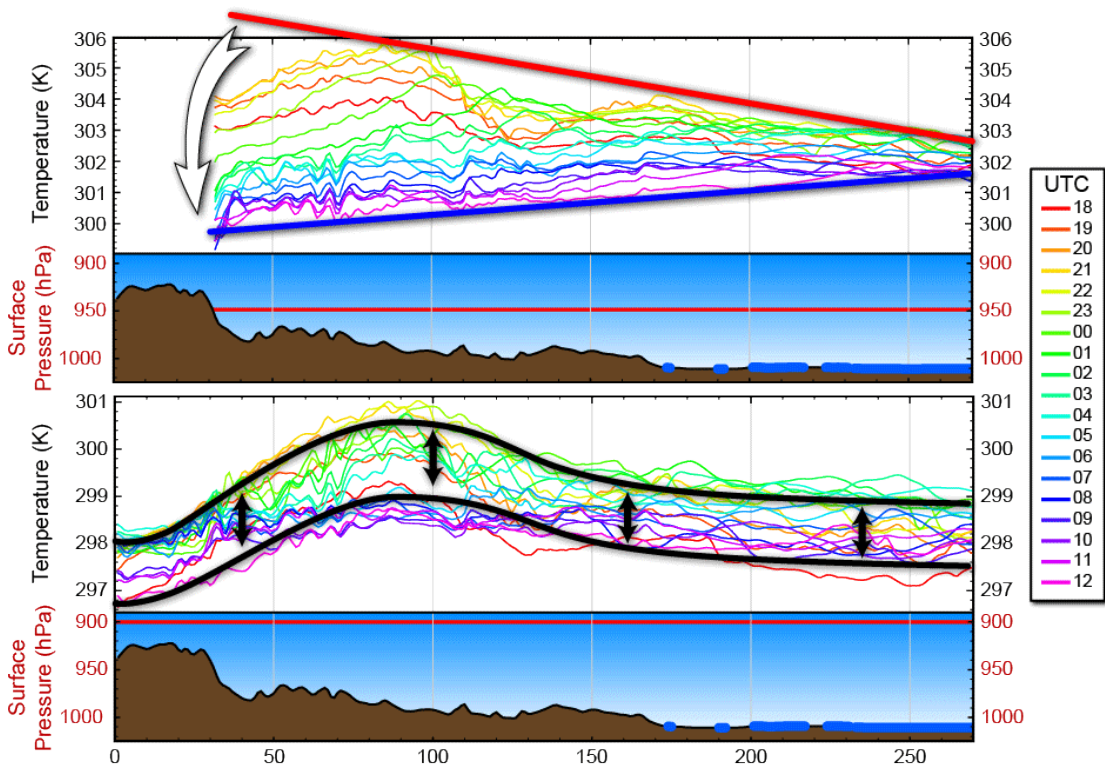


Figure 3.10: Top halves of each graphic show the diurnal temperature evolution at (a) 950 hPa and (b) 900 hPa along an east-west transect in D2 over Baltimore, MD. The legend shows the temperature curve at a given hour. The bottom halves of each graphic show the (a) 950 hPa and (b) 900 hPa horizontal planes in relation to surface pressure (brown terrain). In the top panel, the red (blue) line is a visual aid and approximates a tangent to the isotherms associated with period of maximum heating (cooling). The white arrow indicates tilting of the isotherms throughout the night. In the bottom panel, black lines provide a visual aid to illustrate a more uniform temperature field throughout the night at 900 hPa.

The influence of the thermal wind was more noticeable at the meso- γ scale (2-

20 km). For example, the steep negative slope in isotherms over the Blue Ridge Mountains (100-120 along x-axis, Figure 3.10a) that existed between 1800-0000 UTC produced thermal wind tendency directed to the south. Likewise, a positive slope in isotherms during the same time existed immediately east of the Blue Ridge Mountains (125-150 along x-axis, Figure 3.10a), producing a strong northward tendency in thermal wind. This corresponded to the west-facing upslope topography of the Piedmont. An animation of the 500 m ASL wind direction confirms the afternoon southwesterly wind flow developed first over this region with the assistance of the thermal wind. It is hypothesized that the thermal wind facilitated the abnormally sharp boundary in wind direction between the LLJ and DW regimes developed over the Blue Ridge Mountain range.

A similar pattern was observed over west-facing slopes of the Eastern Shore. While the terrain slope in the coastal region is minimal, a strong thermal gradient existed between the cool waters of the Chesapeake Bay and the daytime heating of the inland areas of the Eastern Shore. The result was a positively sloped isotherms which generated a southerly thermal wind. The result demonstrated that the western side of the Eastern Shore was also among the first regions to transition into a southwesterly wind regime during the afternoon. The thermal wind phenomenon offers a plausible explanation for early transition of afternoon wind direction observed over the Chesapeake Bay.

Figure 3.10b shows the temperature evolution at 900 hPa, roughly 1 km AGL at Beltsville. While the temperature data still show some spread in specific regions, overall, there is much more consistency with time. Air temperatures tended to rise

and fall more uniformly with decreasing pressure levels. The contrasting nature of this plot compared with Figure 3.10a demonstrates the increasing baroclinicity toward the surface, which in turn, generated strong, shallow low-level winds in Mid-Atlantic region.

3.7 Summary and Conclusions

This modeling study broadly examined low-level flows in the Mid-Atlantic region in response to intriguing and recurring nocturnal features present in the WAVES observation dataset. In Chapter 2, observational evidence was presented supporting the hypothesis that these features were associated with two distinct wind regimes, a LLJ and DW, respectively. However, a modeling study was needed to confirm their identity and provide a broader understanding of the meteorological context that could not be deduced from single site measurements alone. A major emphasis of this case study, which has not been widely discussed in previous literature, was the behavior of these nocturnal events and their close relationship to the local topography of the Mid-Atlantic region.

The first objective of this study was to verify the model results against the nocturnal features observed in the WAVES measurements. Results show that WRF could reproduce the low-level winds and reasonably simulate the LLJ and DW regimes. The modeled and observed maximum mean wind speed of the LLJ regime were comparable, but the model mean wind speed falloff above the jet's nose was typically smaller. For the DW regimes, WRF was unable to replicate the observed sub-kilometer peak wind speeds. The observed wind speed falloff above the DW core was double the simulation value. For both the LLJ and DW regimes, the wind

direction profile was rotated roughly 10-20° counterclockwise from observations. It is unclear what caused this somewhat consistent bias during all 5 days. The WRF-MYJ configuration estimated the PBLH based on a TKE threshold. This method worked well during the late nocturnal period and while the CBL was growing. However, this method did not produce a PBLH consistent with observations during the late afternoon and early nighttime periods, especially during the LLJ regime.

To simplify the modeling results, 3 August was chosen to be a representative day of the prefrontal period. The daily evolution of the wind field was illustrated by examining a horizontal 500 m plane at four different times throughout the day (Figure 3.5). Around 2000 UTC in the afternoon, the CBL began transitioning from a predominantly northwesterly flow to a southwesterly flow. This change first occurred over water and then over land. Reduced surface friction over open water bodies, temperature gradients, and HCRs were all mechanisms which had a role in facilitating the transition of wind direction. Intensification of the LLJ regime began near sunset. Shortly after, a well-defined boundary was established between the LLJ and DW regimes along the Blue Ridge Mountains. Throughout the remainder of the night, the DW advanced southeastward, sweeping the LLJ regime out to sea near dawn. This wind direction boundary typically passed over HUBC between 0500-0700 UTC. By dawn, the entire region was characterized by northwesterly flow in the wake of the DW.

Cross-sections showing the vertical structure and evolution of the DW and LLJ regimes were highlighted in Figure 3.6. The temperature and moisture differential between the mountains and coastal plains established the evening

environment. The LLJ regime originated over the coastal plain and developed from the surface upward, and then expanded westward toward the Blue Ridge Mountains. On the other hand, the DW regime was an external air mass that first appeared in the Appalachian Mountains. The head of the DW propagated eastward and a jet of northwesterly wind flow followed.

An examination of the broader meteorological context showed a link between the prefrontal LLJ in the Midwest and the DW regime (Figure 3.7). It is hypothesized that outflow from the prefrontal LLJ impinged upon the Appalachian Mountain barrier, was forced up the windward side, crested, and then flowed down the eastern flanks of the mountains as a DW event. The increasing mass-flux of the prefrontal LLJ outflow, as the cold front was approaching the Appalachian Mountains, greatly intensified the Mid-Atlantic DW events for 3-4 August. The timing of the DW appearance in the high mountain regions coincided with evening periods when the eddy viscosity of the daytime CBL diminished, which reduced the resistance to low-level laminar flow over the mountains. As the upslope air crested, lee-mountain waves accelerated a stream of air down the east slopes according to mountain flow hydraulics. It is hypothesized that a much thinner water vapor canopy over the mountain highlands, based on the precipitable water vapor field, allowed more efficient radiational cooling and thus produced a katabatic contribution to the DW. Effectively, this offset heat gained through subsidence resulting in an imperceptible temperature difference by the time the DW arrived in the Piedmont region.

To the east of the Appalachian Mountains, a daytime solenoidal circulation influenced Mid-Atlantic low-level winds (Figure 3.8). The Mid-Atlantic solenoid had

hybrid characteristics common to both mountain-plains and sea breeze circulations. This generated a low-level toward-barrier flow that originated from the cooler coastal plain region and was maximized near sunset. The toward-barrier flow had a meridional component that when decoupled from the decaying solenoid, continued past sunset in the form of an inertial oscillation which developed into the LLJ regime. Multiple solenoidal circulation centers developed on east-facing slopes along transitions between major geographic features.

The height of the Appalachian Mountain barrier had a significant impact on low-level winds. Higher mountain elevations intensified the leeside solenoid but impeded outflow from the prefrontal LLJ. Similarly, the higher terrain greatly enhanced the Mid-Atlantic LLJ by generating a more uniform wind speed field with higher values within a deeper layer. The Appalachian Mountain topography had little impact on the intensity of the Prefrontal LLJ and merely redirected outflow. The DW was shallower than the control run with higher wind speeds and a more northerly wind component. The experiment with flattened mountains showed a very weak and shallow Mid-Atlantic LLJ. The DW was weaker, more disorganized, and showed a more blurred boundary between the LLJ and DW regimes. The DW regime was also characterized by a more westerly wind flow control run.

The daily cycle of the thermal field (Figure 3.9) began with inland warming, especially within the Ridge and Valley and Great Valley regions that were more geographically isolated from the cooling effects of water bodies and also more inhibited by poor low-level ventilation. The warm air anomaly deformed the geopotential height field into a trough which conformed to the wind field. The

boundary between the northwesterly and southwesterly winds was typically aligned with the trough axis. As the nighttime period progressed, the anomalies in temperature, geopotential height, and wind advected eastward. By dawn, the trough was situated near the Atlantic coastline, reflecting the late morning temperature differential between the warm waters and the cool mountains. As daytime heating progressed, the trough retrograded against the prevailing westerlies back to the mountain regions, once again. The oscillating behavior of this trough strongly influenced the low-level wind pattern across the Mid-Atlantic. The thermal wind over sloping terrain is also believed to affect low-level flows (Figure 3.10). Examples were presented showing this relationship at the meso- γ scale.

Chapter 4: Model Sensitivity Studies

The focus of this chapter is on the sensitivity of the Advanced Research Weather Research and Forecasting (WRF-ARW) model to different physical schemes during the 1-5 August case study. Numerical modeling beyond observational analysis is inevitably necessary for a more complete understanding of and to provide context for the nocturnal phenomenon observed during WAVES 2006, as described in Chapter 2. It is difficult for concentrated observations at a single location, or even a few locations, to determine with any certainty exactly what dynamics were occurring. The coarse resolutions of operational datasets during that period were insufficient for resolving the fine scale observations. Therefore, higher resolution modeling was needed.

The Advanced Weather Research and Forecasting (WRF-ARW) model is a rapidly developing community model supported by the National Center for Atmospheric Research (NCAR), tailored to meet the needs of the numerical weather prediction research community. It is a full non-hydrostatic mesoscale model with multiple dynamic cores, parameterizations, physics, and other capabilities that allow customized atmospheric investigation within a flexible framework (Skamarock et al. 2008). However, with the availability of many model options comes the possibility of vastly different forecasts. It is common practice to perform sensitivity studies to help analyze and optimize model performance for a specific weather regime (Gallus; Bresch 2006) or case study. In order to most accurately model the events of the WAVES 2006 case study, sensitivity tests were conducted to evaluate WRF's performance across four areas to which the model was believed to be most sensitive:

initial conditions, cumulus parameterization, planetary boundary layer schemes, and initialization time.

It is well known that regional models are sensitive to initial (IC) and boundary conditions (BC) (Clark et al. 2008; Zhang; Fritsch 1986). Global and regional datasets that are used to interpolate initial state information to the modeling domain may contain, and subsequently pass along, biases and deficiencies. Additionally, if the source data are too coarse then it may be difficult or impossible, even for high resolution models, to evolve the same fine scale features present in observed flows (Etherton; Santos 2008). Consequently, the ability to track and capture the interaction of these features with the ambient environment can resolve primary forcing mechanisms responsible for convective triggering (Lilly 1990). Therefore it is, important to choose a dataset that best represents the initial state of the atmosphere.

Cumulus (CU) parameterizations of sub-grid convective processes are fundamental for precipitation forecasts in domains where cloud scales are less than grid scales. While numerous studies have indicated fully explicit treatment of convective processes using resolutions of 4 km or less generally perform better than larger grid scales using parameterizations (Clark et al. 2009; Done et al. 2004; Roberts; Lean 2008), these schemes remain necessary for any grid with coarse spatial resolutions, including outer domains which may contain high resolution nests. Unfortunately, parameterizations have been linked to timing and propagation errors (Davis et al. 2006; Davis et al. 2003; Zhang; Fritsch 1986) and limiting the period of optimal forecast skill (Wang; Seaman 1997; Zhang; Fritsch 1986). Obviously, different parameterizations use different approaches to resolve the same sub-grid

black box problem, each with strengths, weaknesses, and optimal conditions. The overall objective of this sensitivity study was to determine the optimal parameterization that best simulated the case study observations.

PBL parameterizations are crucial to simulating turbulent convective eddies that are smaller than the vertical resolution of the model. These parameterizations critically describe momentum, heat, and moisture fluxes between the surface layer and the free atmosphere. Similar to CU parameterizations, various PBL schemes use different approaches toward a solution, thereby introducing model error. It is argued these parameterizations are a major source of model uncertainty (Hu et al. 2010; Pleim 2007) that can alter circulations in the larger scale forecasts (Hacker; Snyder 2005). In an effort to accurately represent the environment of the case study that includes convection within a stable regime, we conducted PBL sensitivity tests similar to other authors (Hu et al. 2010; Jankov et al. 2005; Nielsen-Gammon et al. 2010).

Models are often initiated at 0000 and 1200 UTC following the convention of many operational environments. However, these time constraints may not allow an optimal elapsed time for model spinup of convective processes (Etherton; Santos 2008). It seems reasonable that better simulation of daily convection should reference a lull in the local diurnal cycle, such as sunrise, when estimating an appropriate period for optimal model spinup that best captures observed convection, rather than simply starting based on a convenient arbitrary universal time. Obviously this becomes trickier when considering domains that span multiple time zones. However, for high resolution regional modeling that focuses on a particular convective area, this

is a valid consideration. This was the justification for conducting an initialization time sensitivity test for our case study. Five different initialization times throughout the morning and afternoon, spanning the times with greatest convective impact, were explored.

WRF verification was performed using the Model Evaluation Tools (MET) package using the WRF post processing software. MET can be configured to interrogate a dataset to develop a robust set of statistics to evaluate performance. Continuous and dichotomous (yes/no) statistics for point, gridded, and object observations were computed. Point observations were compared against distance weighted grid values using various neighborhood widths. Several observation sources were used in the verification process. At Beltsville, relative humidity (RH), temperature, pressure, and PW data from Suominet and the 31-m flux tower base and top were used. Additionally, 31-m tower winds and upward shortwave and longwave radiation fluxes from ground-based instruments were compared. The zonal (U-wind) and meridional (V-wind) components of wind profiles from the MDE profiler and WVMMR profiles from the SRL lidar were ingested. For observations outside of Beltsville, NOAA Meteorological Assimilation Data Ingest System (MADIS) data was used. This included automated aircraft reports and profiles (ACARS), Multi-Agency Profiler (MAP) and NOAA Profiler Network (NPN), radiosonde, and surface observations from which wind, dew point temperature, temperature, pressure, PW, and RH were sampled. Lastly, precipitation was verified using the National Center for Environmental Prediction (NCEP) Stage IV data.

4.1 Experiment Design

An 8 km Lambert Conformal domain was set up across the eastern U.S. that extended east from Illinois to the Atlantic Ocean and from New England south to North Carolina. The grid was placed to best capture the evolving cold front while assuring the Mid-Atlantic region remained in focus. Please refer to the red outline in Figure 4.8 for exact boundaries. The domain (D1) had (x, y, z) dimensions of 230 x 150 x 40 with a uniform horizontal spacing of 8.0 km and vertical levels distributed approximately linear in pressure. All sensitivity runs were conducted using this domain. Runs were initialized at 1800 UTC 2 August and ran 54 hours until 0000 UTC 5 August. Run duration and termination times varied for the initialization time sensitivity study. This timeframe was selected in order to perform sensitivity studies on the Mid-Atlantic prefrontal environment, containing the WAVES nocturnal phenomenon we were trying to replicate through modeling. The experiment was intended to target the most sensitive aspects of modeling this case study with WRF, using key areas (discussed above) believed to lead to maximum forecast divergence for assessing the range of model uncertainty.

4.2 Sensitivity to Model Initial Conditions

For the initial condition sensitivity tests, verifications were performed using runs initialized with NARR, North American Mesoscale (NAM), and RUC analysis data. All runs were identical except for the interpolated initial and boundary conditions. Details are shown in Table 4.1. All three initial and boundary condition data sources incorporate similar observations in generating their analysis.

In addition to the configuration in Table 4.1, WRF physics and dynamics included (i) Goddard microphysics (Tao et al. 1989), (ii) RRTM longwave radiation, (iii) Dudhia shortwave radiation, (iv) Noah Land Surface Model, (v) Urban Canopy Model, (vi) Mellor-Yamada-Janjic PBL scheme, and (vii) no CU parameterization.

Run	IC	IC Grid	WRF Grid	IC/BC Levels	WRF Levels	BC	BC Freq.
1	NARR	32 km	8 km	30	40	NARR	3 hr
2	NAM	40 km	8 km	40	40	NAM	6 hr
3	RUC	20 km	8 km	38	40	RUC	1 hr

Table 4.1: WRF Configuration for IC Sensitivity Tests

4.2.1 Upper-air verification

Overall, the IC sensitivity runs did not demonstrate significant differences in upper air verification (aircraft and radiosonde measurements, surface to 100 mb). All fields showed minimal disagreement with a surprising coherency in the error trends of all three runs. For example, the mean error (ME) from 64,658 ACARS temperature reports was less than 0.153 K averaged across the full 54-hour forecast (Figure 4.1). As a side note, the mean error statistic is referred to more frequently than root mean square error (RMSE) throughout these sensitivity tests because knowledge of positive and negative biases are desired as well. The 90% confidence envelope was usually within +/- 0.1 K of the ME. The ME trend remained centered along the zero x-axis, without drifting toward positive or negative biases. This suggests that for this case study, WRF internal dynamics may be more significant than perturbations introduced from differences in initial and boundary conditions. Therefore, forecasts during this case study were inferred to be relatively non-divergent.

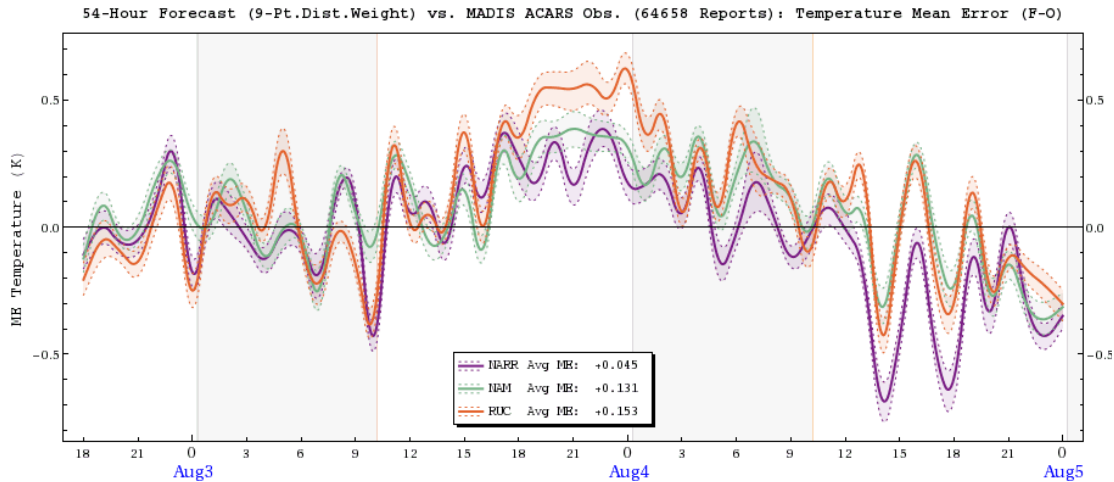


Figure 4.1: ACARS Temperature Mean Error for IC Sensitivity Tests.

4.2.2 Surface verification

Surface observations showed stronger differences between the three IC runs compared to the upper air mean error. The corresponding 54-hour average mean error of surface temperature using 58,990 reports was about twice as large with significantly noisier data (note scale in Figure 4.2). All three runs had a positive and negative temperature bias for the afternoon and nighttime, respectively. Surface moisture was also more variable. All three runs revealed a slightly dry bias (-0.5 g kg^{-1}) near dawn that rose to a moist bias (1.0 g kg^{-1}) before dusk (Figure 4.3). The RUC run exhibited significantly less WVMR ME compared to the other two. PW ME corroborated a similar trend with moist daytime and dry nighttime PBL biases (Figure 4.4). That pattern was reversed for pressure ME (Figure 4.5), showing a positive bias (100-200 Pa) between 0600-1000 UTC and dropping sharply around 1400 UTC to a negative bias (-50 Pa) for the duration of the afternoon until dusk. NARR and RUC runs performed slightly better than NAM.

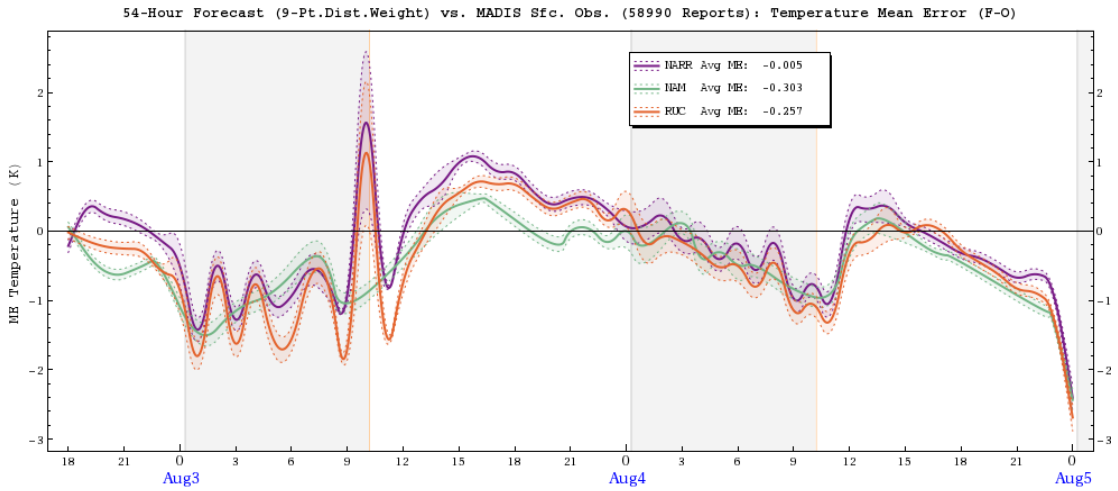


Figure 4.2: SFC Temperature Mean Error for IC Sensitivity Tests.

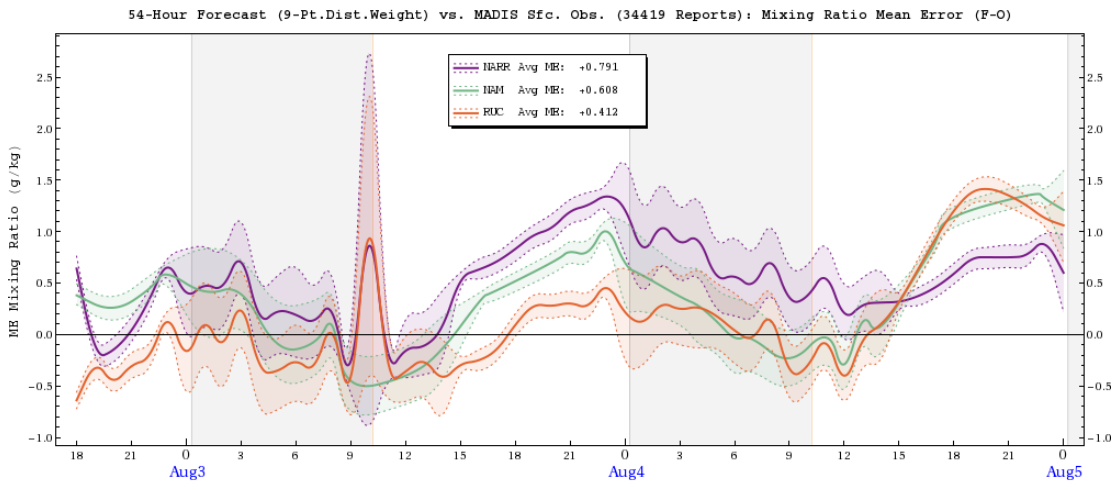


Figure 4.3: SFC Mixing Ratio Mean Error for IC Sensitivity Tests.

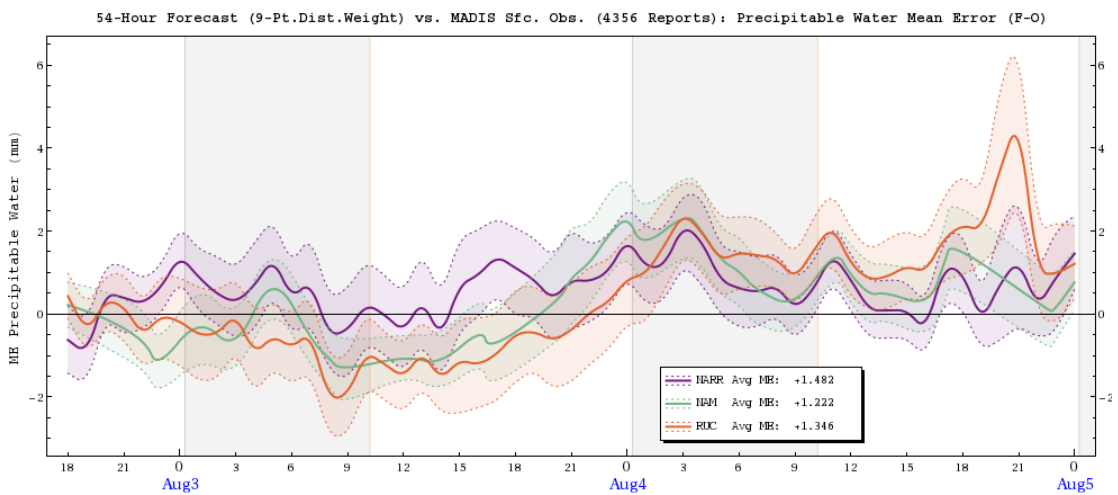


Figure 4.4: SFC Precipitable Water Mean Error for IC Sensitivity Tests.

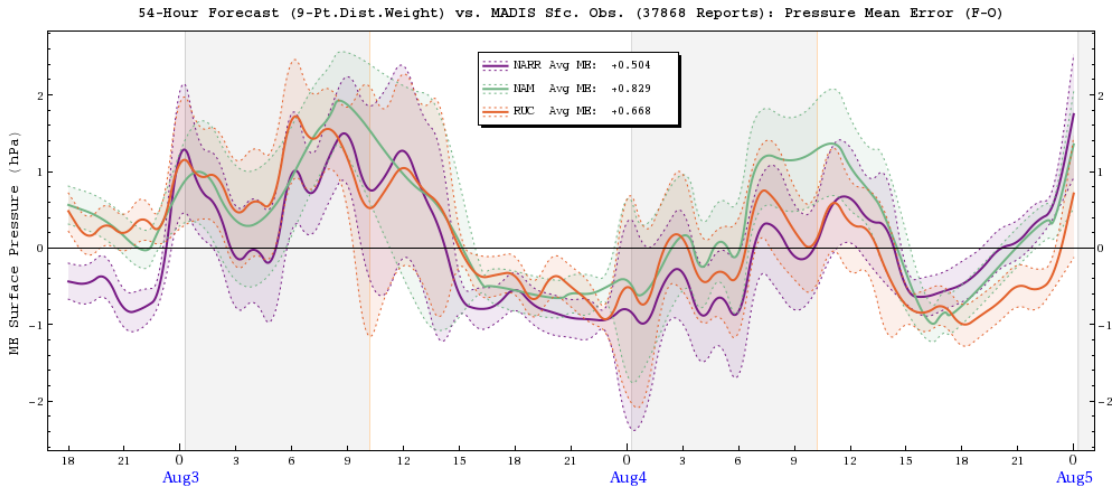


Figure 4.5: SFC Pressure Mean Error for IC Sensitivity Tests.

4.2.3 WAVES verification

The Scanning Raman Lidar at Beltsville was continuously measuring WVMR for the 5-day period. To prepare the data for verification, a mask was generated based on the ASR and WVMR channels to remove any questionable measurements, mostly clouds and high background noise associated with daytime conditions. After applying the mask, Beltsville radiosonde profiles were used to generate an interpolating function relating pressure to geopotential height, assumed as a proxy for geometric height. This was used to remap 0-10 km AGL lidar data, in 30-m vertical bins, to a pressure vertical coordinate that could be ingested by MET. Lidar WVMR ME among the three runs showed substantial divergence during the daytime, but converged closely to zero at night. The WVMR RMSE was smaller during the nighttime periods (Figure 4.6). This was likely due to reduced nocturnal profile noise, allowing the inclusion of more high altitude data points with less variability.

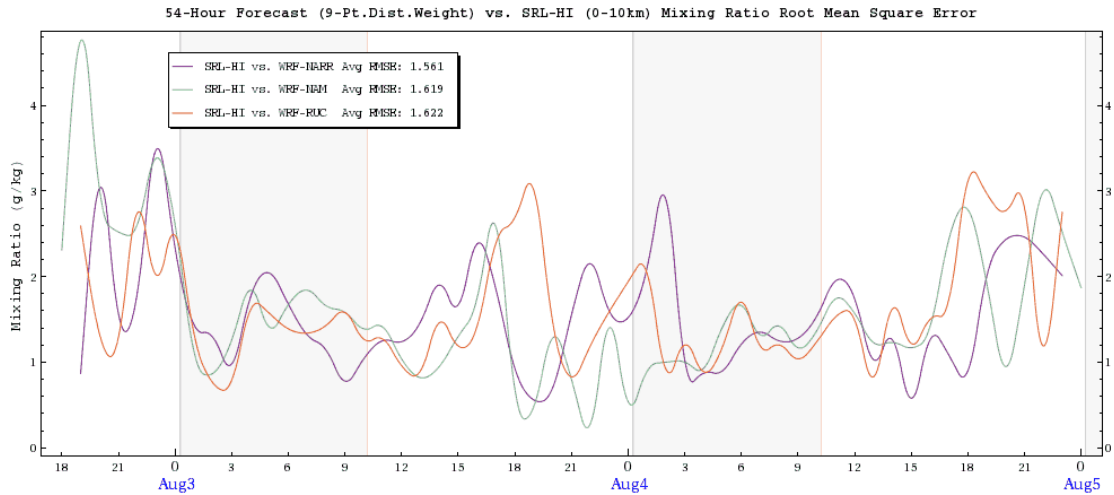


Figure 4.6: SRL Mixing Ratio RMSE for IC Sensitivity Tests.

4.3 Sensitivity to Model Cumulus Schemes

The cumulus parameterization in WRF is used to help estimate convective processes through direct interaction with the model’s microphysics scheme. It includes parameterizations for triggering cloud development, updraft, downdraft, entrainment, detrainment, and compensating vertical redistribution processes, such as subsidence. Since many assumptions handle columns which completely contain a cloud, CU schemes are not valid for all scales. In general, grid spacing greater than 10 km should utilize a CU, and spacing less than 3 km are too fine. A grid spacing of 8 km was used in these sensitivity tests where scale separation becomes the major determinant in the effectiveness of a CU scheme.

This case study during early August required simulation of an eastward moving frontal boundary, and so representing convective processes was imperative. During this time, there was a fair amount of convective activity that moved into, or occurred under, a region of stable subsidence dominating the southeast U.S. weather. This regime included splintering of convective cells and popup thunderstorms, both

of which operate on small scales. The uncertainty regarding the potential effectiveness of CU schemes justified conducting these sensitivity tests. Four runs were performed using KF: Kain-Fritsch Eta (Kain 2004), BMJ: Betts-Miller-Janjic (Janjić 1994, 2000), GD: Grell-Devenyi (Grell; Dévényi 2002), and G3: Grell-3D schemes. The fifth was a control run using no CU scheme (NO).

Aside from the 5 CU scheme options listed above, the physics and dynamics remained the same as in the IC test: (i) Goddard microphysics, (ii) RRTM longwave radiation, (iii) Dudhia shortwave radiation, (iv) Noah Land Surface Model, (v) Urban Canopy Model, and (vi) Mellor-Yamada-Janjic PBL scheme. The initial and boundary conditions for this run use the NARR data (Table 4.1).

4.3.1 Upper-air verification

Upper air comparisons using 64,658 ACARS reports during the 54-hour forecasts did not reveal major differences among CU schemes, nor any large ME. This is somewhat expected since aircraft usually avoid the same convective regions most affected by CU parameterizations. Furthermore, as previously mentioned, upper air observations are further removed from strong gradients associated with surface fluxes. However, all results using CU schemes showed significant coherent undulations each night near 0600 UTC in the WVMR ($\pm 2 \text{ g kg}^{-1}$) and DWPT ($\pm 5 \text{ K}$) mean error curves. The timing is such that oscillation is suspected to correlate with large scale wave perturbations that may be related to the DW formation discussed in Chapter 3. Coincidentally, U-wind exhibited similar oscillatory characteristics at that time. The ACARS temperature trend tracked closely with observations until the dawn

of 5 August when a -0.5 K bias developed. This indicated the model's underestimation of upper-air temperatures in the post-frontal air mass.

4.3.2 Surface verification

There were more differences among CU members verified against MADIS surface observations than in the upper air. The surface moisture ME trend bifurcated into two groups (Figure 4.7). The KF, G3, and GD group exacerbated the moist afternoon bias evident in the IC sensitivity tests, while the BMJ and runs using no cumulus parameterization (NO) runs showed better agreement with observations. Even the 90% confidence interval of the BMJ and NO runs seldom exceeded $\pm 0.5 \text{ g kg}^{-1}$. Ironically, PW moisture comparisons (not shown) did not bifurcate. The best performing schemes were the G3 and GD and the worst were the NO and BMJ. This demonstrates that the overall precipitable water column among the five runs was similar even though CU precipitation or subsequent PBL processes may have caused different surface moisture observations. Temperature, pressure, and winds among CU runs showed very similar trends to those discussed in the IC section.

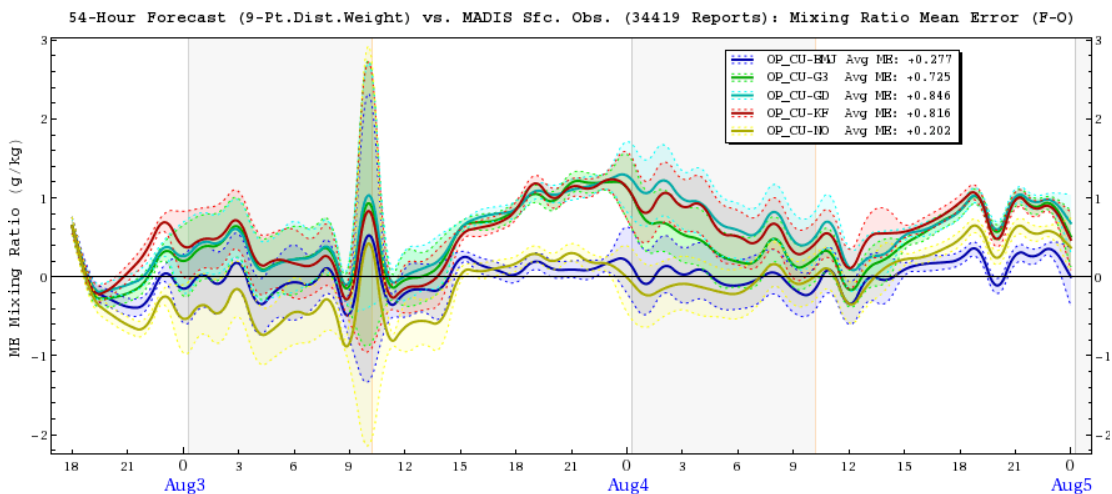


Figure 4.7: SFC Mixing Ratio for Cumulus Sensitivity Tests.

The run with no CU scheme was selected to probe the spatial distribution of surface WVMR anomalies, since it performed better compared to observations. All contributing stations were plotted hourly on a map designating their geographic location with a disk shaded according to their ME values, scaled to $\pm 2.0 \text{ g kg}^{-1}$. Reports located in the vicinity of any model or observed precipitation were ignored because of the potential for strong biases in surface WVMR in regions with precipitation forecast misses and false alarms. Rather, the focus was to investigate patterns in rain-free regions. At 1800 UTC 2 August, all major eastern cities (Baltimore, Washington, DC, Philadelphia, New York, Boston, and Norfolk) showed a moist bias (Figure 4.8a). The Appalachian Mountain rural regions also showed similar moist biases; while stations located west of Illinois, behind the cold front boundary, had dry biases. As the day progressed toward evening, inland cities trended toward a dry bias (Figure 4.8b), while cities such as Boston, New York, and Norfolk remained moist. Unfortunately, surface observation data became much sparser during overnight hours, as many surface stations did not report. However, there were still enough sites online to visually interpolate a rebound of urban moisture overnight. By 1500 UTC 3 August, a host of surface observations came online again. During the afternoon there was once again a drying of the greater Piedmont and coastal regions east of the Appalachian Mountains, although there was less drying in the immediate urban centers than the previous day, 2 August. Concurrently, there was a smattering of positive and negative moisture biases within the rural Appalachian Highlands with no discernible pattern; most likely this was strongly influenced by isolating geography. The drying pattern repeated again for the Baltimore-Washington region

during the afternoon hours of 4 August. An early afternoon initial drying trend was detected in the northeastern cities, but quickly moistened through nearby late afternoon convection and storm blow-off along the frontal boundary.

The discovery of the drying anomaly provoked a corresponding examination of spatial distributions of temperature. The temperature trend within urban environments along the East Coast showed a large afternoon warm bias in the model (Figure 4.8c). This occurred on 2 and 3 August. However, by 2300 UTC 3 August, most of the temperatures along the East Coast displayed a cool bias. This was attributed to storm outflow from areas of false model precipitation that stretched up the Ohio River Valley, across central Pennsylvania, and into northern New Jersey. On 4 August, the afternoon warming persisted again, this time with less convection disrupting the trend. By 1800 UTC, the urban warm anomaly peaked and was evident along the I-95 urban corridor. The remainder of the northeast, outside the urban centers, was cooler than observations. The gradient of afternoon temperatures between urban and rural regions was at least 3.0-5.0 K stronger than observations, especially near Boston. Likewise, model urban surface pressure is consistently higher than observations for all three days (Figure 4.8d). This is undoubtedly linked to the higher surface temperature through the ideal gas law.

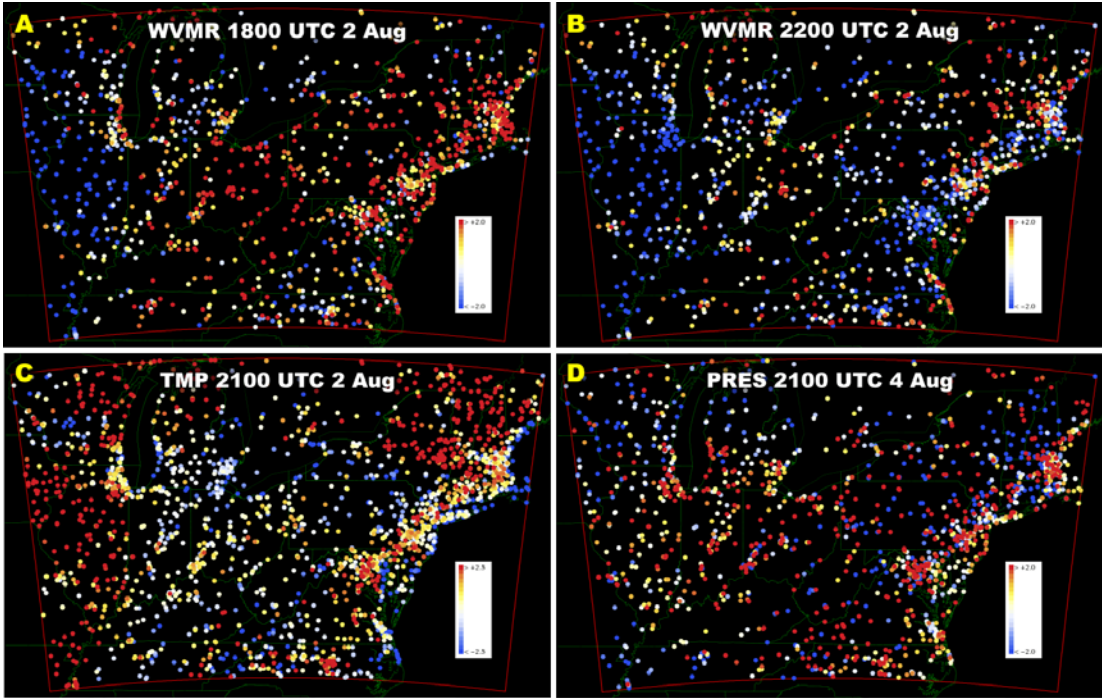


Figure 4.8: SFC ME anomalies showing (a) WVMR at 1800 UTC 2 August, (b) WVMR at 2200 UTC 2 August, (c) TMP at 2100 UTC 2 August, and (d) PRES at 2100 UTC 4 August.

4.3.3 Precipitation verification

Accumulated precipitation is one of the most fundamental model quantities to verify when evaluating CU parameterizations or broader model performance within convective regimes. However, deriving meaningful skill scores and assessment metrics for this is nontrivial. For example, “double penalty” errors arise when there is slight timing or spatial displacement in precipitation features even if models realistically portrayed the convective feature (Ebert 2008). A number of methods have been proposed to deal with precipitation metrics ranging from subjective to objective (Done et al. 2004; Weisman et al. 2008) and neighborhood-based to object-based (Davis et al. 2006; Ebert; McBride 2000; Roberts; Lean 2008). In this paper, objective statistics were generated using the neighborhood method and the Method

for Object-based Diagnosis and Evaluation (MODE). Additionally, visual subjective analysis was performed. Model verification began by interpolating NCEP Stage IV accumulated precipitation (standard 240 grid with ~4.7 km resolution) to the WRF domain using a budget method. Ten precipitation accumulation thresholds were employed, ranging from 0.0 to 5.0 inches weighted towards the lower values, to discriminate grid point hits (where observation and forecast agree) and misses (where observation and forecast disagree). Statistics were calculated for the grid point of interest as well as neighboring grid point squares with widths 3, 5, 9, and 13, corresponding to 8, 24, 80, and 168 neighboring cells. Several different statistical measures and confidence intervals were examined.

The Gilbert Skill Score (GSS), otherwise known as the equitable threat score, is an objective metric frequently relied upon for assessing precipitation forecasts. This is a dichotomous statistic that addresses how well a forecast "hit" matches an observed "hit" while accounting for the chance of random correctness. It ranges from -1/3 to 1, with 1 as a perfect score.

$$GSS = \frac{hits - hits_{random}}{hits + misses + falseAlarms - hits_{random}}$$

$$\text{where } hits_{random} = \frac{(hits + misses)(hits + falseAlarms)}{total}$$

Figure 4.9 shows the GSS for 6-hourly accumulated precipitation with a 90% confidence interval for all 5 CU parameterizations across the 54-hour forecast, using a 0.10 inch precipitation threshold. It is evident that convective model precipitation did not conform very closely to observations. Based on this statistic, the BMJ parameterization appears to perform best. The run using no CU parameterization is

ranked second, followed by G3, KF, and the trailing GD scheme. GSS variability associated with the NO run is higher than the others. It was evident that using neighborhood values generally provided a better score until a cluster of 25 grid points was reached, spatially translating to a distance of 20 km in each direction. After that, scores degraded for all CU schemes. In this case study, statistics computed using small neighborhoods is generally better than one-to-one comparisons. The same statistics were computed for 3-hourly and 1-hour accumulated precipitation. The GSS score declined significantly with shorter accumulation periods. Furthermore, using more neighboring cells for statistics during shorter accumulation periods proved worse than one-to-one grid cell comparisons, reversing the trend noted in the 6-hour GSS score. Neighborhood statistics are beneficial for higher skill scores up to a critical radius, which is determined by the accumulation period.

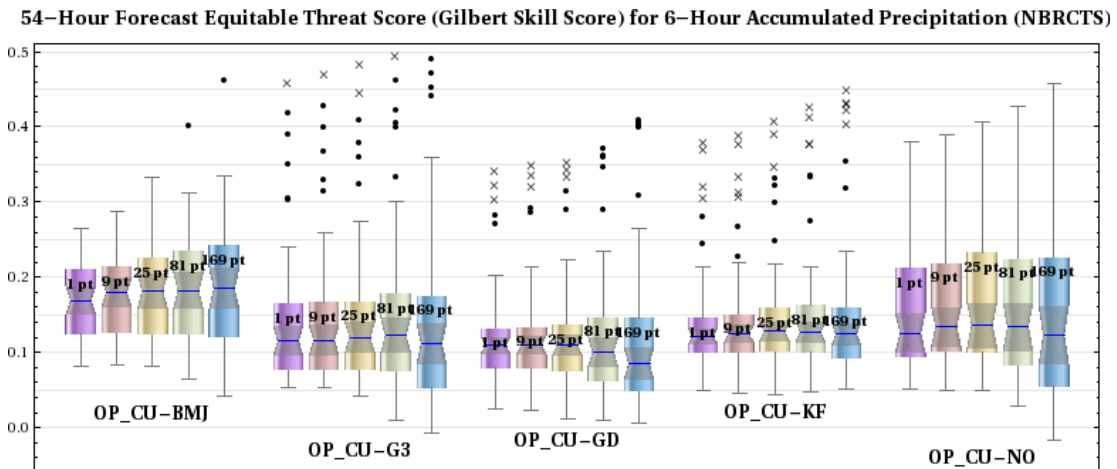


Figure 4.9: GSS for 6-hr precipitation (neighborhood statistics).

Low overall GSS scores provoked a visual examination of precipitation distribution associated with the 5 CU parameterization runs. For this, precipitation objects were defined using MET’s MODE tool which applied a smoothing convolution operator, based on a radius of influence, and then applied a threshold to

generate identification masks. Objects and larger object groups are defined in this way for both forecast and observed precipitation fields. Then, objects are matched and merged using a “fuzzy-logic” engine. Standard statistics are calculated on object and group pairs in addition to many other attributes, such as area, axis angle, centroid, curvature, and complexity. Figure 4.10 shows an example of precipitation objects generated with at least 1.50 mm accumulated 1-hour precipitation. Subjectively tracking these objects over the 54-hour forecast, the G3, GD, and KF schemes appeared to quickly spinup precipitation along the frontal boundary during the afternoon of 2 August. BMJ and NO runs were noticeably more conservative. By 2100 UTC, most runs showed clusters of precipitation along the frontal boundary in the Great Lakes region even if the object were slightly translated from the correct observation location. At 0300 UTC 3 August, the G3, GD, and KF runs have well-simulated a line of convection along the frontal boundary. The run using no CU has broken areas of precipitation, and BMJ has very little. At 0500 UTC, the line began to disintegrate and all runs, except BMJ, had precipitation areas placed quite well. During the quiescent early morning period, all runs tapered off precipitation, except the G3 and GD schemes which erroneously developed convection in the upslope region of West Virginia. Midday 3 August showed well-placed areas of precipitation in all runs. However, as the afternoon progressed, the G3, GD, and KF schemes generated inordinately large areas of precipitation across northern Ohio and Indiana, along the Ohio River Valley and West Virginia, and through northern Pennsylvania into New York. Figure 4.10 shows a clear example illustrating the tendency for the G3 schemes too overproduce precipitation across broad areas, especially triggering

along windward slopes. This demonstrates that the parameterization either does a poor job clustering convective cells and removing instability elsewhere or it facilitates unrealistically efficient coalescence processes, or both. The BMJ and NO runs were much closer to observations. By 0000 UTC 4 August, all runs had generated a line of precipitation, whereas observation showed virtually all precipitation had decayed. During the early morning hours a few spotty areas of observed precipitation resurged as the forecast precipitation was fading. By 0700 UTC, all runs agreed well with observations once again. During the afternoon of 5 August, all runs over predicted the areas of precipitation again, although the NO run did not develop precipitation in the northeast like the others. Over the 54-hour simulation, the G3, GD, and KF schemes clearly erred on readily developing widespread precipitation, the BMJ scheme consistently underestimated precipitation until the end, and the run using no CU parameterization generally compared better with observations, both in placement and spatial coverage.

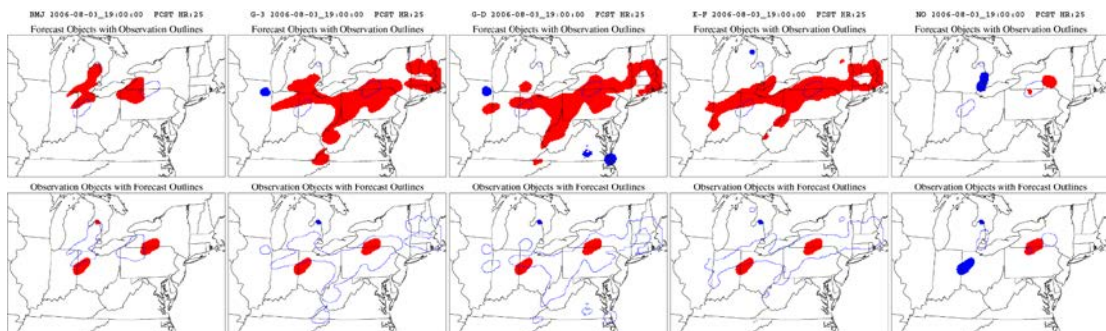


Figure 4.10: Cumulus Sensitivity comparison of MODE 1-hr precipitation objects at 1900 UTC 3 August.

The temporal progression of precipitation statistics for 1-, 3-, and 6-hourly objects was also examined. Object accuracy was consistently above 80% for all runs for all accumulation periods. However, the accuracy metric is misleading since it

includes very high false alarm ratios, which peak close to 1.0 during late afternoon maximum convection. The false alarm ratio usually drops below 0.2 during the nocturnal stable early morning hours. Therefore, the Critical Success Index (CSI) and the GSS are much better metrics for assessing precipitation forecast skill. The CSI statistic is very similar to GSS, but without accounting for "random" correct hits. Intriguingly, the BMJ CSI time series was below 0.2 for the first half of the simulation and rose toward 0.4 for the second half (Figure 4.11b). This was attributed to the schemes' inability to generate precipitation during the afternoons of 2-3 August. The afternoon had noticeably less convection, and so the accuracy of BMJ rose. The CSI time series for the G3 (Figure 4.11a), GD (Figure 4.11c), and KF (Figure 4.11e) runs were all similar. There was decent agreement with observations throughout the early morning hours of 3 August with a CSI exceeding 0.5, due to sparse convection. However, from the daytime hours of 3 August until the end of the simulation, the CSI oscillated between 0.0 and 0.2, with minima during the afternoon of 3 August and the morning of 4 August. The time series of the run with no CU scheme (Figure 4.11d) was similar to the G3 run, except CSI values during the afternoon of 3 August were closer to 3.0, and around dawn of 4 August they reached 4.0. The GSS scores had a similar trend to the CSI, with a slightly lower skill score. In summary, the run with the highest precipitation scores for all times was the NO run.

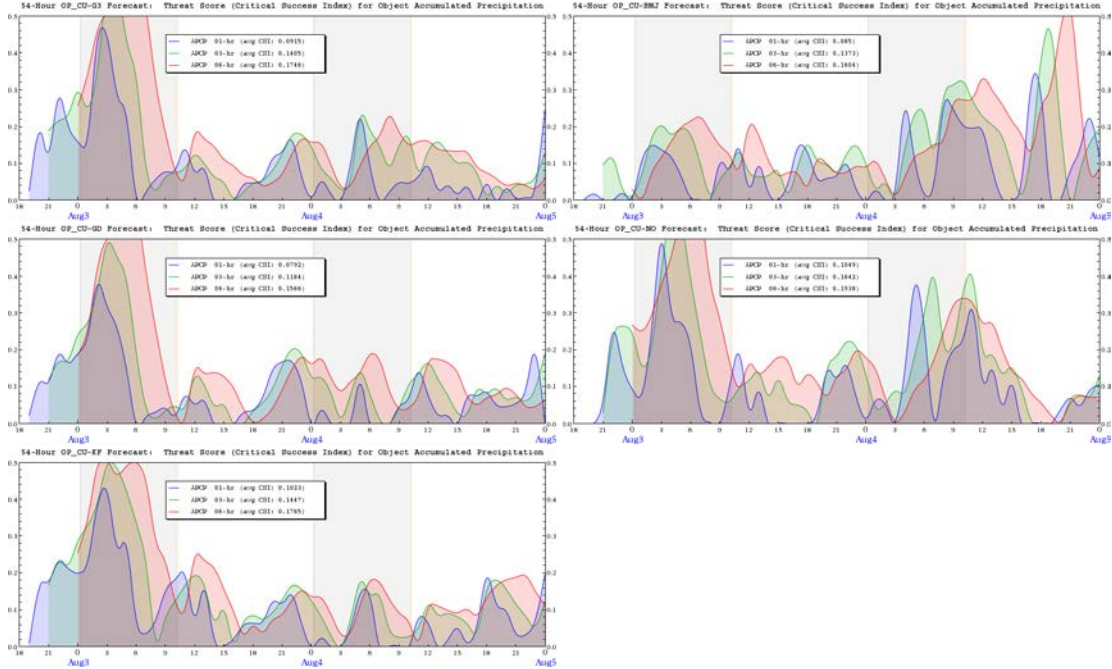


Figure 4.11: Cumulus Sensitivity CSI for MODE objects for (a) Grell-3D, (b) Betts-Miller-Janjic, (c) Grell-Devenyi, (d) No-cumulus scheme, and (e) Kain-Fritsch.

4.4 Sensitivity to Model Planetary Boundary Layer Parameterizations

It is believed that PBL processes played a large role in this case study. In particular, Mid-Atlantic observations revealed dynamic sub-kilometer atmospheric processes would obviously be strongly influenced by PBL parameterizations. The basic function of all WRF PBL schemes are to distribute heat, moisture, and momentum fluxes between the surface layer and the free atmosphere. There are two basic PBL parameterization approaches: (1) diagnostic schemes that prescribe diffusion coefficients which are used to specify a profile, or (2) Turbulent Kinetic Energy (TKE) schemes that relate diffusion coefficients to length scale and a prognostic kinetic energy equation to determine the profile. Within those categories there are many other differentiated details, such as vertical column local versus non-local closure (direct neighbor versus neighborhood grid cell interaction). As such,

there are advantages and disadvantages associated with each approach. Therefore, a sensitivity study was conducted to examine the performance of 8 different PBL parameterizations: ACM2: Asymmetric Convective Model (Pleim 2007), BOULAC: Bougeault-Lacarrère (Bougeault; Lacarrere 1989), MRF: Medium Range Forecast (Hong; Pan 1996), MYJ: Mellor-Yamada-Janjic (Janjić 1994), MYNN2: Mellor-Yamada Nakanishi and Niino Level 2.5 (Nakanishi; Niino 2006), MYNN3: Mellor-Yamada Nakanishi and Niino Level 3 (Nakanishi; Niino 2006), QNSE: Quasi-Normal Scale Elimination (Sukoriansky et al. 2005), and YSU: Yonsei University (Hong et al. 2006).

In addition to the 8 PBL parameterizations listed above, the Global Forecast System (GFS) scheme was also tested, even though it was intended for use with the WRF-NMM core. Not surprisingly the results were very poor. From here on out the PBL sensitivity test will be considered to have 8 members, without the GFS run. All other physics and dynamics remained the same as previous runs: (i) Goddard microphysics, (ii) RRTM longwave radiation, (iii) Dudhia shortwave radiation, (iv) Noah Land Surface Model, (v) Urban Canopy Model, and (vi) no CU scheme. The initial and boundary conditions for this run use the NARR data (Table 4.1).

4.4.1 Upper-air verification

There is very little difference among PBL runs verified against upper air observations. All runs capture the same model oscillations seen through observation verification. Good agreement among the 8 runs at this altitude is not surprising since PBL processes are, for the most part, far removed from these observations. For temperature comparisons, the MRF run had the lowest averaged 54-hour ME of -

0.011 K, while QNSE had the highest of -0.137 K. MRF outperformed the others with respect to mixing ratio as well, with an averaged ME of +0.186 g kg⁻¹. The YSU scheme had the largest moisture error with a +0.329 g kg⁻¹. All runs tracked together closely for upper air wind comparisons. From model initialization to 0000 UTC 4 August, there was a positive trend in U-wind ME, increasing from near 0 to 1.25 m s⁻¹. Then it returned to no bias for the remainder of the simulation. V-wind showed a negative trend from initialization time to midday 4 August. The increasing overestimation of westerly and northerly flow may have been associated with increasing grid area of postfrontal air entering the domain, which continued until the frontal progression was disrupted and impeded by the Appalachian Mountain barrier on 4 August.

4.4.2 Surface verification

The multi-agency and NOAA wind profiler network verifications contained more error and member spread than the aircraft observations, since their primary use is for sampling PBL winds located near the surface. The data from both MAP and NPN networks exhibited similar ME patterns reflected in the aircraft data. The U-wind ME ranged between +2.2 and -1.4 m s⁻¹, and V-wind ME between ± 2.8 m s⁻¹. For the nocturnal period of 3 August, all PBL runs over- and under-estimated the U-wind component at dusk and dawn, respectively. V-wind ME showed an oscillatory behavior coinciding with the timing of the LLJ and DW events. The early morning hours of 4 August were characterized by significant underestimation of V-wind.

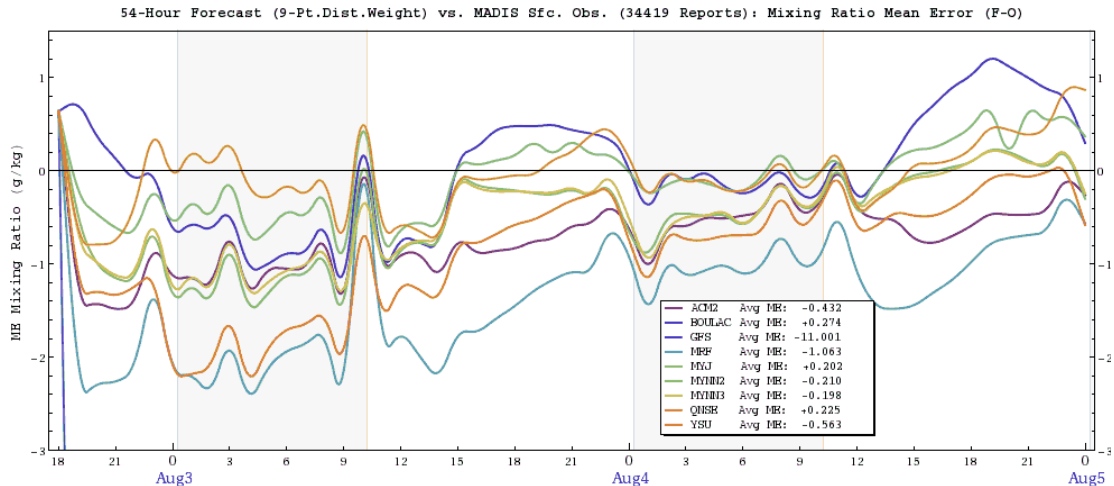


Figure 4.12: SFC Mixing Ratio for PBL Sensitivity Tests.

Comparisons with MADIS surface observations showed significant differences among the 8 PBL runs. Surface mixing ratio, verified using 34,419 reports, showed a spread in ME curves ranging between +1.2 and -2.4 g kg⁻¹ during the 54-hour forecast (Figure 4.12). Overall, MYNN3 and MYJ schemes perform best with values of -0.198 and +0.202 g kg⁻¹, respectively. MRF was significantly worse with an average ME of -1.063 g kg⁻¹. Overall, most runs showed a dry bias for the duration of the forecast. The spread in moisture among PBL members was larger shortly after initiation but converged substantially by 1000 UTC 4 August. This period coincided with convective activity across the domain, and so it is possible rainfall was acting to moisten the surface and mitigate the dry bias. Surface temperature among the PBL runs also showed a significant spread in ME ranging from +2.2 to -1.6 K throughout the forecast (Figure 4.13). The spread was largest during nocturnal periods and narrowest during the afternoon. All PBL schemes performed much better during periods of daytime mixing, but need significant improvement for periods of stable nocturnal temperatures. At one end of the spectrum of members, the YSU run had a persistent warm bias. At the other, the QNSE run was

consistently cool. The best performing member with lowest average ME was the MYJ scheme with a mere -0.039 K. The worst was YSU schemes with +0.846 K. All runs consistently showed a significant positive bias in surface wind speed (WSPD) above 2 m s^{-1} , while the spread was at most 1.4 m s^{-1} . It is suspected that overall surface roughness should be increased to bring down wind speeds.

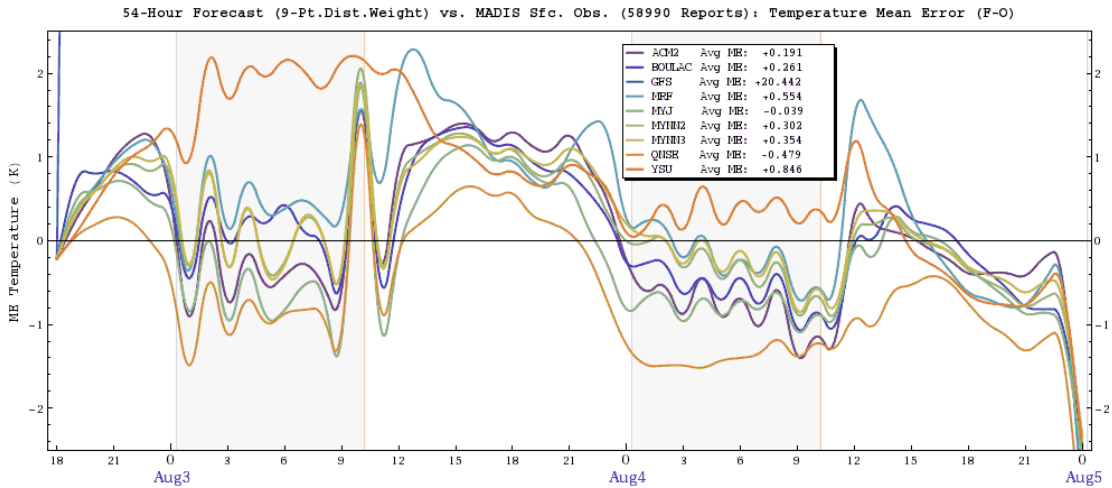


Figure 4.13: SFC Temperature for PBL Sensitivity Tests.

4.4.3 WAVES verification

Surface observations at Beltsville were used in model verification, as well. Temperature ME trends over the forecast period show large nocturnal divergence within PBL schemes, spanning up to 6.0 K, and daytime convergence in closer agreement to within 1.0 K (Figure 4.14). ME temperature curves between the surface and 31-m were quite similar, as expected. However, there were slightly larger nighttime spreads in 31-m temperatures. Tower data did not reflect a corresponding spread in temperature observations, so there must be another explanation. It is suspected that WRF does not properly simulate surface conditions just after sunset. This theory has merit based on noting the spikes in temperature ME that occur near

dusk. Profiler and surface measurements at Beltsville show there was an increase in surface WSPD almost concurrent with nightfall, and usually a corresponding sharp change in wind direction (WDIR) as well. This increased wind would generate turbulent mixing and thereby slow the rate of radiational cooling at the surface. No PBL runs were able to accurately replicate this daily phenomenon. Additionally, the 31-m wind data showed a sharp change in WDIR, and often WSPD, within the first hour of daylight. This can be observed by noting the smaller spikes in the ME statistics near dawn. Taking a second look at the domain-wide MADIS surface temperature data, there were clear spikes in ME data both entering and exiting the nocturnal period. It cannot be said with certainty that this was the same mechanism hypothesized at Beltsville. Nevertheless, it is a curiosity that spikes in ME surface data were present in temperature, humidity, and wind fields across the entire domain.

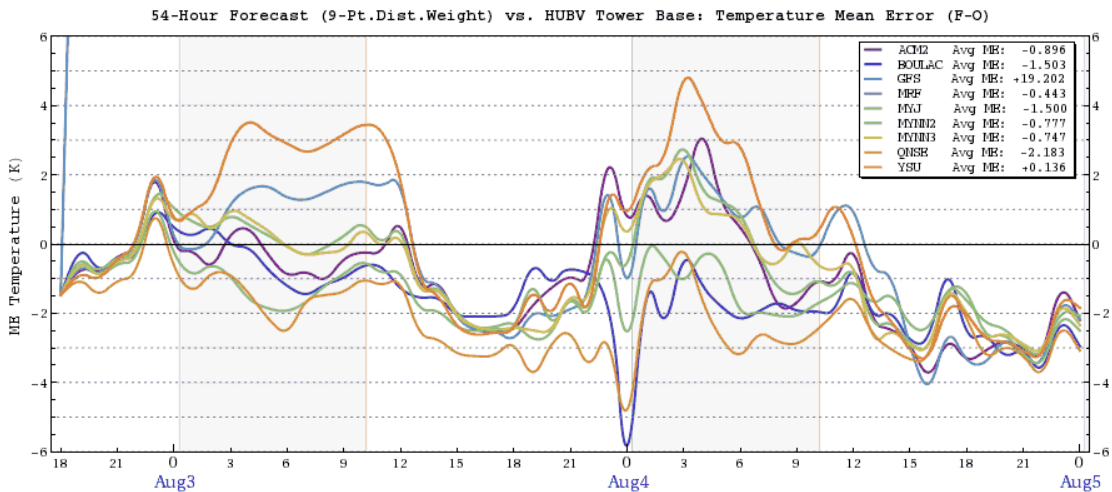


Figure 4.14: Beltsville Temperature for PBL Sensitivity Tests.

There were other interesting trends in Beltsville surface observations. Daytime surface temperature ME showed a -2.5 K cool bias. The relative humidity ME was very similar to the temperature trend just discussed, with a very large nocturnal spread among PBL members spanning up to 35% by night and collapsing back to 5%

by midday (Figure 4.15). There was a persistent dry bias both for day and night. The RH curve bifurcated during the early morning hours of 4 August. The BOULAC, MYJ, and QNSE schemes clustered around zero ME, while the other schemes dip into a -25% dry bias. The three best performing were TKE PBL schemes, which coincidentally occurred during more breezy overnight periods. The other group was composed of members (ACM2, MRF, and YSU) that did not account for kinetic energy, with the exception of the MYNN2 and 3 schemes. It was unclear why those two higher order TKE schemes, which additionally include sub-grid processes, did not perform as well. Upwelling long wave radiation measurements also varied up to 40 W m^{-2} , and most often with a positive model bias. The time average ME for QNSE was best with a small -0.553 W m^{-2} . BOULAC and MYJ schemes followed with values near $+7 \text{ W m}^{-2}$. ACM2, MRF and YSU were the worst performers with the latter having a $+20.246 \text{ W m}^{-2}$ overall bias for the forecast period. Upon examining upwelling short wave ME, there was less time averaged difference, in part because nocturnal ME was always zero. However, there were a few instances with large divergence among PBL members; those times were 1800-2000 UTC and 1700-1900 UTC for 3 and 4 August, respectively. Those anomalies correlated with spikes in the LW ME values but did not appear to have any lasting impact. The overall best performing PBL members at correctly simulating atmospheric conditions measured at Beltsville were the TKE schemes; in particular MYJ and QNSE were very good across all surface observations.

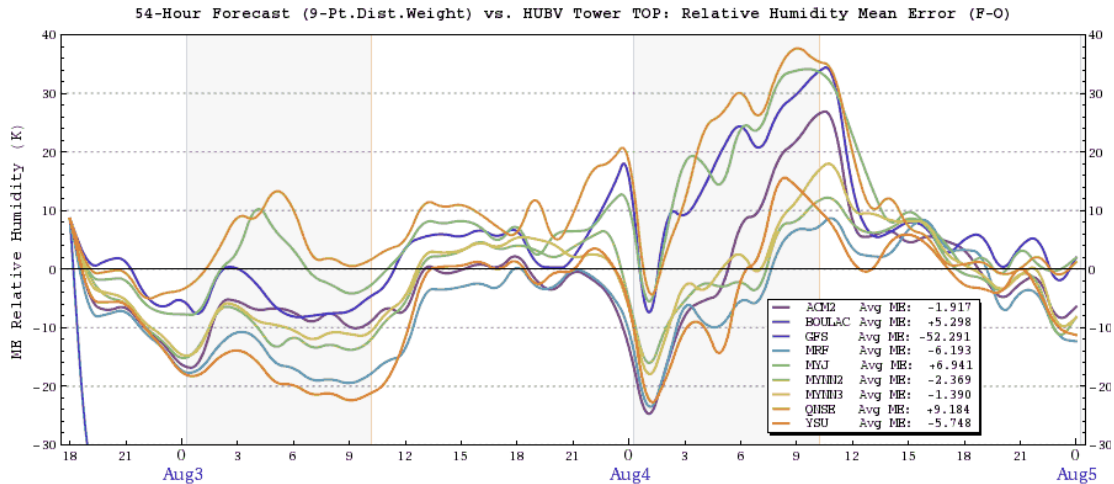


Figure 4.15: Beltsville Relative Humidity for PBL Sensitivity Tests.

Now this research will highlight some unconventional surface observation verification. MET statistics for SRL data were analyzed as a single column as well as the following pressure levels (Figure 4.16): from 600-1020 hPa, WVMR data was divided into 50 hPa layers, from 400-600 hPa data was separated into 100 hPa layers, and lastly, the top layer was 250-400 hPa. Using this approach it was possible to better understand the vertical distribution of moisture within the model. Averaged 54-hour ME values for the overall 1020-250 hPa column show MYJ performs best with a median ME near zero. BOULAC and QNSE also performed well. ACM2, YSU, and MRF performed poorly. Breaking down the verification by pressure levels, there was an evident dry bias in the atmosphere below 850 hPa and from 850-650 hPa there was a moist bias. This trend was manifested by all PBL schemes. The highest RMSE, near 2 g kg^{-1} , was associated with 750-800 hPa where low-level cumulus tended to develop. From there, error magnitude reduced above and below similar to the falloff of a bell curve. The lowest errors were found at the highest altitudes, which contain the least moisture leading to small errors. There was a consistent dry trend in the lower atmosphere among all surface observations. WRF appears to smooth over

vertical moisture gradients near the PBL top and above. Whether this is a result of microphysics inefficiency or blending of stratified layers is beyond the scope of this paper. The column WVMR RMSE curve (not shown) mostly remained under 2 g kg^{-1} throughout the forecast period, with the exception of the morning daylight hours of 3 August where it approached 3 g kg^{-1} . After that, there was a sharp change in the afternoon with RMSE values dropping to near 1 g kg^{-1} .

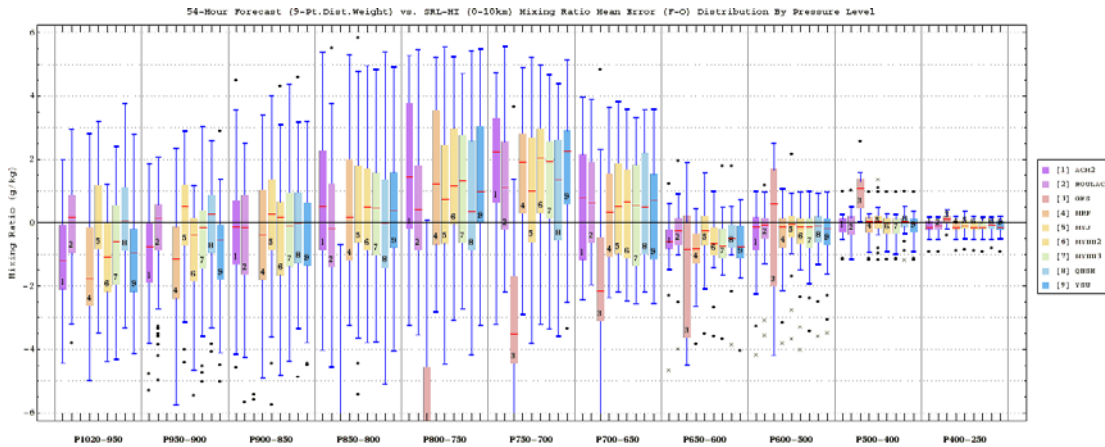


Figure 4.16: SRL mean Error by height for PBL Sensitivity Tests.

A similar process was used in the statistical analysis of Beltsville sonde data. Observations were placed into pressure bins for level-by-level verification. From 500 hPa down to the surface layers were 100 hPa thick. Above that, three layers spanned 300-500, 300-200, and 200-100 hPa. The mixing ratio measured by sonde data revealed the same dry trend in the PBL and a moist bias between 700-800 hPa. Temperature data had fairly good agreement with observations with median ME values within 1 K for all levels. Overall, there was a slightly cool bias below 500 hPa and a warm bias above. In the final column analysis, the average ME was close to zero. The MYJ scheme had a slight lead, but there were no significant differences among the PBL schemes. The U-wind ME data showed fairly good agreement with

observations below 700 hPa, but ME increased with altitude thereafter. The final column analysis places all median ME values between 0-0.5 m s⁻¹. V-wind ME is much larger with greater variability. The lowest errors occur in the midlevel 500-700 hPa with larger ME above and below. Generally speaking, there were no PBL schemes with superior performance based on sonde verification. All values were in the same vicinity. Mixing ratio appeared to be the most challenging variable for WRF to accurately represent. All fields indicated a discontinuity between levels around 700-750 hPa, indicating a distinction between boundary layer and free atmosphere processes.

4.4.4 Precipitation verification

Precipitation analysis for the PBL runs was conducted the same way as described in the CU sensitivity study. For precipitation objects, a subjective visual comparison was done first. Precipitation objects from those schemes were simultaneously compared and ranked according to their comparison to actual precipitation objects. The author's opinion is that MYJ was most accurate, followed by MYNN2, MYNN3, YSU, QNSE, ACM2, BOULAC, and MRF. Turning toward a less subjective computational method, the BOULAC, MYJ, and YSU schemes had the highest GSS scores for 1-hour accumulated precipitation. For 3-hour accumulation, MYJ and BOULAC performed best, and for 6-hour accumulation (Figure 4.17), BOULAC and YSU had the highest scores. Overall, the BOULAC and MYJ schemes were consistently high ranking. Temporally, the highest GSS score occurred between 0000-0600 UTC 3 August and 0600-1500 UTC 4 August. MYJ almost reached 0.6 during that period, and MRF trailed with a low score rarely

exceeding 0.2. The 54-hour forecast of 1-hour accumulated precipitation statistics show that including increasingly more neighborhood data degraded the overall forecast skill. Including 9 grid points was beneficial, but using 169 points showed almost no skill. There was a significant loss of skill between patches comprised of 25 points versus patches of 81 points, or alternatively, a width distances between 40 and 72 km. Using a 3-hour accumulation, the GSS skill increased about 230%. For this metric, using a patch 9-point patch was better than single cell-to-cell comparisons. However, there was a negative benefit to computing statistics on larger patch sizes. Using a 6-hour accumulation, GSS score increased roughly by 140%. This accumulation period shows skill improvement using 25-point patches for the best performing schemes. Not all schemes showed improvement using this area. Regardless of sample sizes and accumulation intervals, the issue most relevant to the sensitivity study was the consistently higher skill scores of the BOULAC and MYJ schemes at representing correct precipitation. It is interesting that visually the BOULAC scheme was rated second to last. Determining precipitation skill numerically may be repeatable, but may not capture similarities spotted by the naked eye.

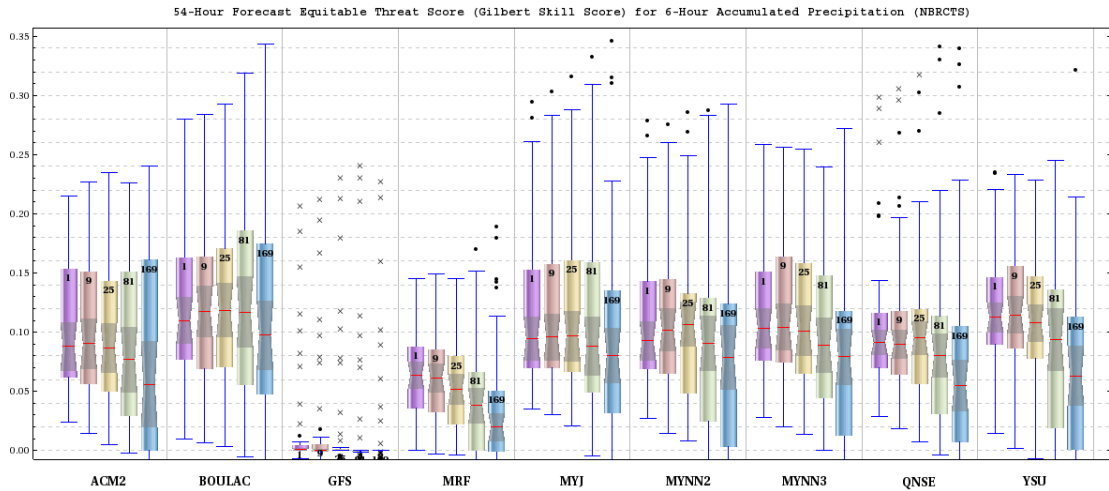


Figure 4.17: GSS for 6-hr precipitation for PBL sensitivity tests.

4.5 Results Discussion

The major finding of the initial condition sensitivity tests was that there was little difference between runs initialized with NARR, NAM, and RUC initial and boundary conditions. All performed reasonably well against verification metrics. NAM mean error comparisons were often smoother and less oscillatory in nature compared to NARR and RUC. On the other hand, NARR and RUC runs frequently showed slightly better agreement with observations. Since the mean error of all three initial condition runs coherently trended in the same direction with time, with only small disagreements on bias magnitudes, it is an indicator that WRF was less sensitive to perturbations in initial conditions than internal dynamics creating systemic model error. This also implies that forecasts during this case study were relatively non-divergent.

The results of the cumulus sensitivity testing for the 8 km grid showed much better results without any parameterization. The performance of the G3, GD, and KF schemes were very similar. All three schemes had a tendency to generate

precipitation quickly, sometimes within the first hour. All three schemes overproduced precipitation across broad areas, especially the windward slopes. The BMJ schemes performed very poorly for the first 24-hours, but then simulated the precipitation better than the G3, GD, and KF schemes. The BMJ is an adjustment parameterization that relaxes toward a post-convective well-mixed profile. This may explain why it performed poorly during periods of deep convection and better with little precipitation. The other three schemes use mass-flux parameterizations. It is presumed these schemes were too sensitive, readily triggered deep convection, and did not provide effective CU closures to remove convective available potential energy over time thereby slowing subsequent cloud growth. The BMJ, KF, and G3 schemes all account for shallow convection, but it appears that the BMJ scheme was most effective at limiting precipitation in accordance with observations. Observations showed significant frontal cloudiness, but areas of high radar reflectivity and rainfall were scattered under a broad subsidence region and quickly decayed when daytime heating ceased. Observations also indicate precipitation was triggered near regions of orographic lift or in the vicinity of frontal boundary. Profiles show that there was not much convective available potential energy and significant convective inhibition, especially over the Mid-Atlantic. It is interesting that a coarse grid scale of 8 km outperformed cumulus parameterizations that theoretically account for more detailed processes. The results point to the fact that summertime convection within quasi-stable air masses at that scale are better resolved using normal model dynamics without CU parameterization enhancements and triggers. These forecast differences

highlight the benefit of using a model physics ensemble approach which can assign precipitation probability drawing from different condition sensitive parameterizations.

Overall, it is concluded the MYJ parameterization performed best during this case study. This conclusion was based upon the combined overall performance across all observation types, fields, times, and altitudes. Generally, TKE schemes outperformed non-TKE parameterization using only 40 vertical levels. Thus, the BOULAC and QNSE schemes also performed well. Coincidentally, these three schemes are all local 1.5-order TKE closure schemes that simulate mixing in the convective and stable boundary layers and are argued to be weakly linked with the surface layer (Shin; Hong 2011). However, the MYJ scheme was mainly intended for stable and slightly unstable flows (Mellor; Yamada 1982) due to the fact that local closure is least valid under regimes dominated by large eddies, such as convection, where local gradient values are no longer valid for turbulent fluxes (Hu et al. 2010). Therefore, it is not surprising that these schemes did well in this weather regime. Data profiles show an extremely layered atmosphere under general subsidence of a high pressure in the southeast U.S. This layering was also consequential to correctly simulating nocturnal low-level flows that are typically thinner in depth. What is somewhat surprising is that MYJ performed better in terms of correctly matching precipitation than schemes considering nonlocal fluxes explicitly (ACM2) or implicitly (YSU). These findings are contrary to the results of Hu et al. (2010) who found the MYJ performed worse than schemes with nonlocal closure. Correctly simulating moisture profiles in the lowest 5 km was difficult for every PBL scheme.

Even MYJ could not represent the true multi-layered nature of the atmosphere and excessively smoothed humidity and wind profiles in the PBL.

The initialization time sensitivity tests (Appendix A) showed mixed results. However, it was established that the best simulated convective events were initialized 5-6 hours prior. If spinup times were shorter, then precipitation had not developed to maturity. If spinup times were longer, then there was too much divergence in the placement and shape of modeled precipitation verses observed. Beyond the first 24 forecast hours, WRF converged to similar solutions even if observations were significantly different, illustrating deficiencies in the model. Overall, the T12 run simulated the afternoon convection slightly better than the other initialization times.

The verification of WRF accumulated rainfall demonstrates this weather regime was difficult for accurate quantitative precipitation forecasts (QPF) among the available CU parameterizations in WRF. Furthermore, there were different approaches to verifying precipitation. Whether verification statistics are calculated using one-to-one grid cells, neighborhood methods, or an object-matching approach, the results will differ. Choosing an appropriate accumulation interval is important. Longer intervals will typically show better forecast skill since probability of precipitation at a given location increased with longer sampling periods. In this case study, using visual object comparison of 1-, 3-, and 6-hourly side-by-side visual runs provided the best insight in understanding WRF's QPF performance. We conclude it is much easier for the naked eye to determine if observation and forecast objects are similar in shape, scope, and location. It is more challenging for automated "fuzzy-

logic” engines to arrive at the same conclusion. The downside to a visual approach is the tedious nature of the process and the subjective determination of forecast quality.

Generally speaking, all sensitivity tests show significantly less error associated with upper air observations compared with those at the surface. The fact that surface error is higher, and in some cases more than doubling, is likely related to the model parameterizations for cumulus and the planetary boundary layer. Upper air dynamics, in this case study, are more simplistic compared with complex surface interaction. This led to very good model performance in the free troposphere, which also had an advantage of smoother initial fields that were often optimized through assimilation of the same observations. It is obvious from the data there is more uncertainty regarding surface initial condition, such as heat, moisture, roughness, and vegetation. All runs showed a dry bias in the lower boundary layer and a moist bias near the PBL top. Surface observations also showed a dry bias along with overestimated wind speeds. Large oscillations can be noted coincident with the LLJ and DW regimes.

High-resolution National Land Cover Dataset (NLCD) 2001 urban land-use information was used to drive the three-category Urban Canopy Model (UCM) for all runs. It is possible that this may have allowed warmer surface temperatures during the day, but cannot explain the cool bias for nighttime surface temperatures. Furthermore, the UCM influence is limited geographically to only urban areas. It is likely that temperature and moisture are linked, causing an overestimation of moisture during the day. It is unclear what mechanisms may be driving the cool dry bias for overnight

periods. Regardless, this helps explain the positive pressure bias toward morning and the negative bias in late afternoon.

Chapter 5: Summary and Future Work

The purpose of this study was to analyze and understand the mechanisms behind the 1-5 August WAVES 2006 observations and present an explanation for the intriguing features observed in the dataset. A major contribution of this research was the synthesis of several collocated complementary research-grade measurements, that when combined, provided a powerful analytical tool for discerning the structure and evolution of the lower atmosphere. Meteorological features, such as the cold front and prefrontal trough, were identified with the additional revelation of a pronounced diurnal cycle that contained the LLJ and DW regimes. Another major contribution to this study was the documentation of the horizontal and vertical evolution of the LLJ and DW regimes within the Mid-Atlantic during this case study. This research highlighted several causation mechanisms for these low-level flows and provided linkages to other influential circulations, such as the Prefrontal LLJ. Lastly, the results in this paper assessed WRF's performance in representing this case study as it related to key physics and initial condition parameters to which the model was sensitive.

The WAVES field campaign was introduced in Chapter 1. The observations acquired during WAVES impelled an investigation of this case study. Field campaigns typically amass large amounts of data. Often there is insufficient manpower for comprehensive analysis of field data. The implication is that some data can be subjected to a cursory review or be overlooked altogether, which leads to unfound science. This case study underscores the potential benefits of an in-depth

study from a small portion of a data-rich field campaign. Chapter 1 also reviewed important concepts relevant to the circulations found in the Mid-Atlantic region.

Chapter 2 discussed the details of the various WAVES observations and how they were key to discovering the pronounced diurnal cycle with three distinct stages. The evolution of the PBL differed significantly from the classical notion of the nocturnal PBL presented by Stull (1988). Stage I was characterized by the growth of the CBL throughout the daytime, which rose to ~1.8 km, and winds which turned southwesterly later in the day. Stage II was defined by intensification of southwesterly flow into a LLJ regime. It was argued that true PBLH during this regime likely remained above the LLJ around 1 km. Stage III was marked by the entrance of DW from the northwest. This air mass was accompanied by stronger winds that cleared the lowest kilometer of the atmosphere. In the wake of the DW, a stream of high speed sub-kilometer flow persisted until dawn, at which point it became an elevated jet riding on top of a developing CBL. Observations from the profiler indicated that the sub-kilometer atmosphere was significantly influenced by inertial oscillations but diminished quickly with height. A prefrontal trough was identified on 4 August, which had many characteristics that were similar to the prefrontal troughs described by Schultz (2005). This led to a change in the wind pattern for 4 August. On 5 August, the weak summertime cold front arrived in the Mid-Atlantic. Even though the orientation of the front in the mid-troposphere was southwest-to-northeast, observations indicated the postfrontal low-level flow behaved analogously to a backdoor cold front by entering the region from the northeast. The postfrontal air in the subsequent days was noticeably cooler and less humid.

Chapter 3 focused on modeling this case study and investigating the low-level circulations that generated the intriguing observation patterns. The clean air slots that appeared in the ASR data were shown to be the result of downslope winds. A regional investigation showed the DW was enhanced by outflow from the prefrontal LLJ, which was forced up the windward side of the Appalachian Mountains, crested, and was accelerated down the east flank of the mountains by the hydraulics of lee mountain waves with a katabatic contribution. Experiments conducted using various Appalachian Mountain heights impacted the LLJ and DW regimes. A solenoidal circulation was established on the east slopes of the Appalachians. The solenoid formed over temperature gradients between inland surface heating and cooler coastal areas that were thermally regulated by large water bodies. This Mid-Atlantic solenoidal circulation had similar characteristics to both mountain-plains and sea breeze circulations. This circulation developed a low-level toward-barrier flow over the Piedmont and coastal areas by late afternoon, with air ascending over the Blue Ridge Mountains. The solenoidal circulation was greatly intensified with higher mountains. Model results indicated daytime surface heating deformed the geopotential height field into a deeper lee-trough. The geopotential height anomaly subsequently influenced the low-level wind field. Nighttime advection moved the thermal anomaly eastward, along with the respective trough and wind shift. Diurnal heating the following day caused the warm air anomaly to retrograde westward toward the mountain regions against the prevailing flow. The oscillating trough greatly impacted low-level wind flow patterns within the Mid-Atlantic. The thermal wind over sloping terrain was also demonstrated to affect low-level flows. A

significant contribution of this research was highlighting the role of topography in determining local circulations. The Appalachian Mountains and surrounding geography provided a major forcing mechanism during weak synoptic conditions.

Chapter 4 highlighted the importance of conducting sensitivity tests in order to determine the optimal model parameters that enabled an accurate simulation of the fine scale observations of this case study. It was believed that the four parameters to which the model was most sensitive to were: (1) initial conditions, (2) cumulus schemes, (3) PBL parameterizations, and (4) initialization time (Appendix A). In order of importance, parameters (2), (4), (3), and (1), respectively, were found to have the greatest impact. The major findings were that WRF was unable to accurately reproduce the convective areas along the Appalachian Mountains and Mid-Atlantic region during 3-4 August. Much of the convection occurred under the influence of a high pressure area, whereby triggering mechanisms appeared to be responsible for convection initiation. Model improvement is needed for simulation of orographic precipitation in neutral and mildly unstable environments that have significant convective inhibition. In general, all cumulus parameterizations over-predicted precipitation using the 8 km grid spacing. In locations where model rainfall was correctly forecasted, the intensity was often under-predicted. Results highlighted the inability of WRF to properly organize convective clusters into a coherent system. The ideal spinup time for precipitation in this case study was 5-6 hours. Immediately following the spinup period, WRF precipitation was reasonably well simulated. However, precipitation skill was quickly lost a few hours after spinup, at which time forecast accuracy became lower than simulations more recently initialized. Simulated

convection areas often diverged significantly from observations and appeared to remain in their own "model universe". A theme echoed throughout these studies was the convergence of sensitivity members to a common forecast, regardless of initialization time, data, or parameterizations. This convergence could also have resulted from coarse resolution initial condition datasets that contained deficiencies. Additionally, fields that were verified against thousands of observations showed coherent oscillations in mean error among different runs. This could imply a systemic shortcoming in the NWP, its parameterizations, or phenomena not properly captured by the initial condition fields. These peculiarities may be attributed to transient internal gravity waves. Regardless, more research would be required to narrow down the potential sources of error. The sensitivity studies also revealed a systematic dry bias in the PBL compared to lidar and sonde observations. Lastly, the PBL parameterizations which used the prognostic TKE equation produced the best overall results. However, these schemes still fell short in replicating a realistic PBLH during late afternoon and nighttime periods.

In conclusion, the overarching contribution of this dissertation is a better understanding of low-level flow dynamics in the Mid-Atlantic during weak synoptic summertime forcing. Improved understanding of nocturnal dynamics are of foremost interest to the air quality modeling community. Both displacement of a nocturnal air mass and the dispersion of pollutants in the lower atmosphere have significant ramifications for air quality forecasts. For example, these phenomena could potentially impact the ozone forecast for the following day by reducing near-surface ozone concentrations during the night more than otherwise expected. Secondly, better

understanding of the mechanisms responsible for LLJ formation and prediction in the Mid-Atlantic are of particular interest for operational meteorologists in addition to the air quality community. Enhanced nocturnal convection has been linked to the LLJ (Helfand; Schubert 1995; Higgins et al. 1997; Tai-Jen Chen; Yu 1988; Wang; Chen 2009), and a similar relationship would be expected in the Mid-Atlantic. In addition to scientific advancement, this research also affects aviation, fog forecasting, temperature anomalies (from sea breezes, DW, and LLJ phenomena), and an overall realization of the significant impact shallow circulations have in governing Mid-Atlantic weather. The findings of this research should encourage more field campaigns in the future. We underscore the need for more high resolution observation profiles which can be utilized for investigating and diagnosing intriguing phenomena. Observations are also useful for verification against models with increasingly higher resolutions.

Future research is needed to quantify some of the findings of this study and identify the dominant causation mechanisms or triggers. While the overall synoptic setting of this case study is quite common, more research is needed to establish how often low-level winds similar to this case study occur within the mid-Atlantic region. One of the primary areas for future work will be modeling other similar case studies that can be identified by similar signatures in wind profiler data. By modeling other case studies, common themes could be identified and applied for better forecasting of nocturnal events. Manually scanning through profiler observations during the warm seasons of 2006 – present shows many other intriguing low-level flows are present in the dataset and await further investigation. Additionally, it would be ideal to examine

other case studies where other nearby wind profilers were also running. A new wind profiler near Cambridge, Maryland, will become operational this year. Once this happens, comparisons between profiler measurements in the mountains (Piney run), the Piedmont (Beltsville), and the coastal region (Cambridge) can be made. Often the research lidar systems operated by NASA, Howard University, and University of Maryland Baltimore County are simultaneously running and collecting profiles that can be analyzed. Future work could also examine the erroneous model precipitation produced in this case study and investigate the mechanisms responsible for forecast convergence.

The WAVES field campaign in 2006 inspired and formed the basis for this research. Our hope is that more field campaigns such as this can take place in the future, allowing the continued investigation of low-level transport within the Mid-Atlantic which remains an understudied, yet complex, region of the country.

Glossary of Acronyms

ACARS: automated aircraft reports

ACM2: Asymmetric Convective Model boundary layer parameterization

ASR: aerosol scattering ratio

ASL: above sea level

AGL: above ground level

BC: boundary conditions

BLH: boundary layer height

BMJ: Betts-Miller-Janjic cumulus parameterization

BOULAC: Bougeault-Lacarrère boundary layer parameterization

CBL: convective boundary layer

CSI: critical success index

CU: cumulus

D1: outer domain of simulation

D2: inner domain of simulation

DW: downslope winds

G3: Grell-3D cumulus parameterization

GD: Grell-Devenyi cumulus parameterization

GSFC: Goddard Space Flight Center

GSS: Gilbert skill score

HCR: horizontal convective rolls

HUBC: Howard University research campus

IC: initial conditions

KF: Kain-Fritsch cumulus parameterization

LDT: Local daylight savings time

LLJ: low-level jet

LU: land use

MADIS: Meteorological Assimilation Data Ingest System

MAP: Multi-Agency Profiler network

MDE: Maryland Department of the Environment

ME: mean error

MET: Model Evaluation Tools

MODE: Method for Object-based Diagnosis and Evaluation

MRF: Medium Range Forecast boundary layer parameterization

MYJ: Mellor-Yamada-Janjic boundary layer parameterization

MYNN2: Mellor-Yamada Nakanishi and Niino Level 2.5 boundary layer parameterization

MYNN3: Mellor-Yamada Nakanishi and Niino Level 3 boundary layer parameterization

NAM: North American Mesoscale

NARR: North American Regional Reanalysis

NASA: National Aeronautics and Space Administration

NATIVE: Nittany Atmospheric Trailer and Integrated Validation Experiment

NCEP: National Center for Environmental Prediction

NLCD: National Land Cover Dataset

NO: runs using no cumulus parameterization

NOAA: National Oceanic and Atmospheric Administration

NPN: NOAA Profiler Network

NWP: numerical weather prediction

PBL: planetary boundary layer

PBLH: planetary boundary layer height

PBLT: planetary boundary layer top

PSU: Pennsylvania State University

PW: precipitable water

QNSE: Quasi-Normal Scale Elimination boundary layer parameterization

QPF: quantitative precipitation forecasts

RASS: radio acoustic sounding system

RH: relative humidity

RMSE: root mean square error

RUC: Rapid Update Cycle

SBL: stable boundary layer

SRL: Scanning Raman Lidar

T00: run initialized at 0000 UTC 4 August

T12: run initialized at 1200 UTC 3 August

T15: run initialized at 1500 UTC 3 August

T18: run initialized at 1800 UTC 3 August

T21: run initialized at 2100 UTC 3 August

TKE: turbulent kinetic energy

UCM: Urban Canopy Model

U_G : meridional component of geostrophic flow

UTC: universal time coordinates

U-wind: zonal component of wind

V_T : meridional component of thermal wind

V-wind: meridional component of wind

WAVES: Water Vapor Variability – Satellite/Sondes

WDIR: wind direction

WRF: Weather Research and Forecasting

WRF-ARW: Advanced Research WRF dynamic core

WSPD: wind speed

WVMR: water vapor mixing ratio

YSU: Yonsei University boundary layer parameterization

θ (Theta): potential temperature

θ_e (Theta-E): equivalent potential temperature

Appendix A: Sensitivity to Model Initialization Time

The final sensitivity test was one that examined model performance versus initialization time. Many modeling studies are initialized at 0000 or 1200 UTC. The reasons behind this are varied, including the availability of operational datasets, traditional convention, consistency, or large domains where this may be less relevant. Regardless, in this study it was not assumed that those particular times necessarily led to accurate forecasts. At one end of the time spectrum, it seems reasonable for a model's spinup phase to begin with quiescent fields near dawn that can evolve naturally and consistently with model dynamics. At the other end of the spectrum, the inclusion of recent transient meteorological features pertinent to convection, such as moisture convergence anomalies, within the model's initialization fields may provide the best placement, timing, and triggering of cells. In this paper, the purpose is not to resolve this debate but to look objectively at the performance of runs initialized at various times. Specifically, runs were initialized every three hours throughout the convective period of 1200 UTC 3 August to 0000 UTC 4 August. These runs are henceforth referred to as T12, T15, T18, T21, and T00 according to their respective initialization time.

The physics and dynamics for these runs were: (i) Goddard microphysics, (ii) RRTM longwave radiation, (iii) Dudhia shortwave radiation, (iv) Noah Land Surface Model, (v) Urban Canopy Model, (vi) Mellor-Yamada-Janjic, and (vii) no CU scheme. The initial and boundary conditions used NARR data.

A.1 Upper-air verification

The same observation verification methodology was applied to these runs as described in the previous sensitivity studies. Upper air ME comparisons did not reveal significant disagreement between initialization times. Ironically, even though runs began at different starting points and fields, the upper air error between runs tended to converge over time and together oscillate about the zero axes. This was indicative of a stable regime with little forecast divergence. Nevertheless, the average mixing ratio ME was best for the T12 run and decreased with each successive initialization run. Average temperature ME showed the opposite trend and improved with later forecast times. Wind data averaged ME was best starting somewhere in the middle. These results were somewhat incoherent, with no major differences between the initialization times. Statistically all of those runs performed rather well.

A.2 Surface verification

Verification using MADIS surface observations showed a similar pattern to the upper air data. All fields showed spread in ME within the first 12 hours due to the various initialization times, but then converged tightly within 24 hours and remained that way throughout the duration of the forecast. All data curves moved with a striking coherence in time.

A.3 Precipitation verification

One of the more important aspects to consider in assessing initialization time was examining model performance at generating convection on the afternoon of 3 August into the early morning of 4 August. Shortly after dawn on 3 August, a

decaying convective cluster was moving east out of Illinois which provided surrounding environmental instability for areas of new convection later in the afternoon with increasing surface heating. The primary areas of development were: (1) a cluster in Ohio and western Pennsylvania, from 1800-0000 UTC 3 August, (2) the tri-state area of Pennsylvania - New York - New Jersey, from 1800-0000 UTC 3 August, and (3) a line along the Ohio River valley following the western border of Kentucky and West Virginia, from 0000-0500 UTC 4 August. A close examination of 1-hour accumulated precipitation objects showed realistic precipitation distribution within 4-6 hours of model initialization. By 2000 UTC, the run initialized at T15 showed better placement of objects than the T12 run. Likewise, by 2300 UTC, the T18 run showed better placement than either the T12 or T15 runs. This pattern continued with each subsequent run. The optimal time to accurately spinup, develop, and correctly place precipitation was 5 hours. Shorter than this, insufficient precipitation would develop. Longer than this allowed too much forecast divergence between the modeled precipitation and actual observations, as small errors in initial placement grew larger with time resulting in model cells that significantly drifted from reality. Furthermore, WRF tended to overestimate precipitation area with time. Runs with 5-6 hour spinup prior to the event of interest usually best captured it, with the exception of T12 which was the only run to accurately model the tri-state region (2). The T21 run best replicated precipitation in region (3) and T15 run best captured the development in region (1). Popup convection is still challenging for models to accurately simulate. However, due to the converging nature of forecasts within this regime there were few differences in precipitation among the runs beyond the first 24

hours. Convective cell lifetimes in this case study were typically short, driven by afternoon heating and decay after sunset. There was usually little carryover into the following day, allowing atmospheric fields a chance to equilibrate and converge. The result was precipitation coverage and locations were very similar between runs during the afternoon of 4 August, unlike the previous day. The T12 run produced slightly more precipitation in central North Carolina, while T21 produced more along the North Carolina coast, and T00 produced more precipitation along the southern Tennessee boarder. However, these were relatively small differences without any run approximating a perfect forecast. By 5 August all runs were virtually identical in their precipitation forecasts. This indicates that internal model error during this time period was more significant than error introduced through initial field perturbations. However, there was short term benefit to using more accurate initial fields within 5-6 hours of the event of interest. Ultimately, though, these differences collapsed and model error appeared to dominate the converging forecasts.

A.4 WAVES verification

Verification using Beltsville surface observations showed similar convergence of ME, although evaluation in one location naturally introduced more spread. Again, with respect to humidity measurements, the T12 run had the lowest overall average ME. The same was true with temperature and wind fields. T21 showed the overall lowest relative humidity error. Runs initialize between 1500-2100 UTC showed the lowest upwelling shortwave radiation error, and T00 showed the lowest upwelling long wave radiation error. There was not much difference among runs verified against SRL WVMR measurements. However, runs initialized between 1200-1800 UTC

helped mitigate the dry bias in the PBL. Mixing ratio verification using Beltsville sonde data showed T18 performed best. The same was true with relative humidity and temperature fields. Winds were better modeled in T21. Again, it must be emphasized that the differences between runs with various initialization times was relatively small.

Another important aspect of evaluating runs with different initialization times was to compare model profiles against Beltsville sondes. Humidity, temperature, and wind from six profiles were carefully examined. Model data for these fields were interpolated in 4D, using 15-minute model output frequency, 8 km grid resolution, and 40 vertical layers. Therefore, sonde data points were matched in time and space as the radiosonde rose vertically and drifted horizontally. Overall, there were more differences in mixing ratio and wind profiles. Temperature profiles did not deviate significantly unless otherwise mentioned.

The afternoon mixing ratio of the 1755 UTC 3 August sonde was compared with runs T12, T15, and T18 (Figure A.1a). The T12 run, with a 6-hour spinup, outperformed the other two in PBL humidity representation. The PBL mixing ratio was within 1 g kg^{-1} up to the boundary layer height (BLH). The model showed decreasing moisture from the surface up, whereas sonde measurements showed increasing values to the PBL top. On the other hand, the T15 run had a -3.0 g kg^{-1} dry bias throughout the PBL. The T18 run, which basically represented the model's initial fields, showed a mixing ratio profile smoothed over the entire PBL with a gradual decrease with height. From 3-6 km AGL is where WRF consistently had the most difficulty in correctly representing moisture. At this time, WRF established a layer

above the PBL roughly 2-4 km AGL, whereas in reality this layer was thinner from 2-3 km AGL. The results from all runs show a dry bias 2-3 km AGL and a moist bias 3-4 km. The U-wind comparisons were reasonable, although the PBL profile was much more uniform than observations. V-wind performed more poorly and did not represent the distinct atmospheric layers well (Figure A.1b). The plot marks each of the 40 vertical levels with a dot, and so it is evident that the poor representation is not a factor of vertical resolution, but likely the combined result of model vertical consistency and over-smoothed (inaccurate) initial condition fields.

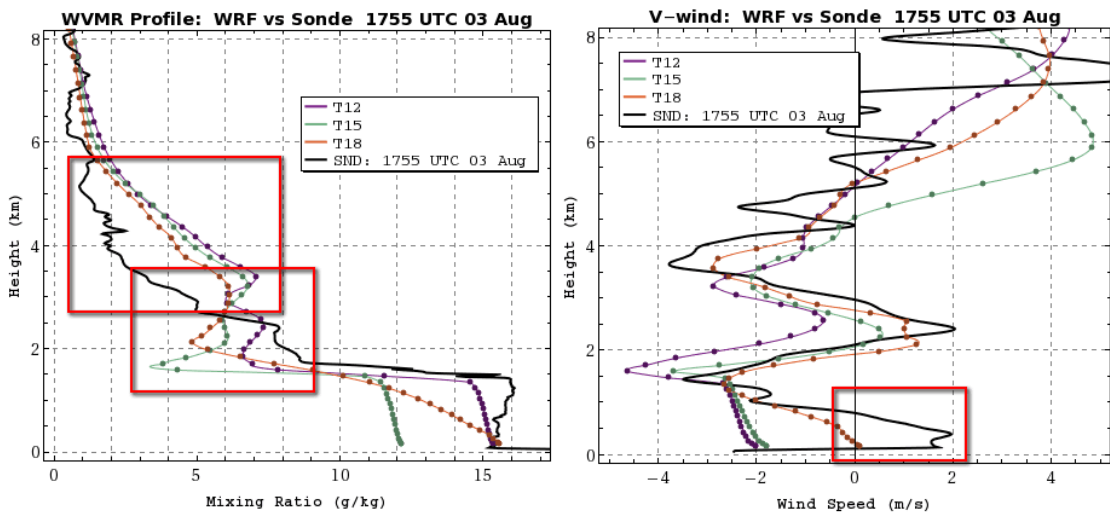


Figure A.1: Initialization sensitivity runs compared with 1755 UTC 3 August radiosonde: left profile is (a) mixing ratio and right profile is (b) V-wind.

The nocturnal hours in the early morning of 4 August showed more disagreement between initialization times. The comparison with the 0559 UTC 4 August sounding revealed that the most recent initialization times subsequently contained more moisture in the PBL and better replicated the profile shape (Figure A.2a). The exception was the T00 run which had a distinctly different profile from the other runs and radiosonde. The same was generally true for a moist layer 3-5.5 km AGL and another at 7-9 km. All model runs portrayed those as dryer than reality,

especially for the moist layer immediately above the PBL that was $1-3 \text{ g kg}^{-1}$ drier than observations. A dry slot 5.5-7 km was moister than measurements indicated. Overall, the best performing run was T18 and the worst was the latest run T00. Although WRF replicated the eroding nocturnal PBL, it was not able to represent the individual layers and the sharp gradient transitions between layers well. The meridional and zonal wind components were well-simulated at this time, in particular the sub-kilometer V-wind showing the DW influence (Figure A.2b). The more recent initialization times showed better agreement with the overall wind profile. T00 had a wind profile notably closer to the radiosonde than the others.

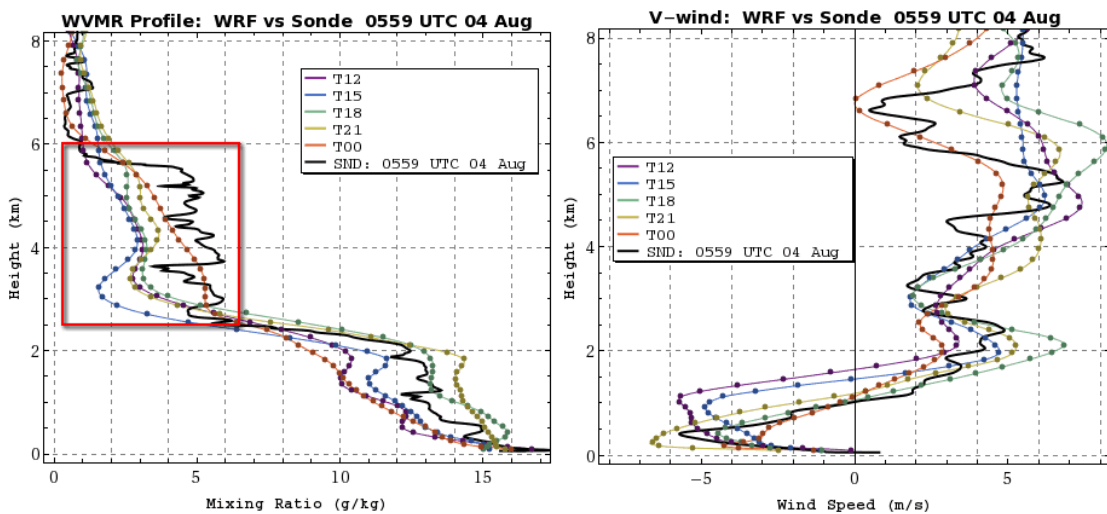


Figure A.2: Initialization sensitivity runs compared with 0559 UTC 4 August radiosonde: left profile is (a) mixing ratio and right profile is (b) V-wind.

At 1706 UTC 4 August, another sonde was launched. This time, all runs more closely represented the mixing ratio profile (Figure A.3a). The T18 and T21 runs were the closest with very little disagreement with observations. Overall, WRF fairly accurately represented all vertical layers and their moisture content, which may have resulted from better model skill in representing a smoother well-mixed moisture profile. The only exception was a sharp decrease in mixing ratio above the BLH,

whereas observations showed a more gradual tapering 1.75-2.5 km AGL. The radiosonde temperature profile showed three large inversions at 2, 4, and 7 km (Figure A.3b). All WRF temperature profiles smoothed over these features marking significant divisions in atmospheric layering. This led to more blurred transitions in the wind profile as well. U-wind was better captured than the V-wind which was much more layered with large oscillations between northerly and southerly tendencies. Below 5 km AGL was characterized by a northerly flow component, while above that had a southerly component. At this time in the forecast, there was not much difference among the initialization runs. The model runs tend to auto-cluster, often breaking completely with the observation profile. Again, this appears indicative of systemic inherent model error as opposed to initial condition error. Similar to the previous daytime sounding, the MYJ scheme effectively blurred the daytime mixed PBL profile so it was unrealistically uniform, even though it was a TKE scheme. New parameterizations should be considered for more realistic PBL modeling under more layered subsidence atmospheric conditions.

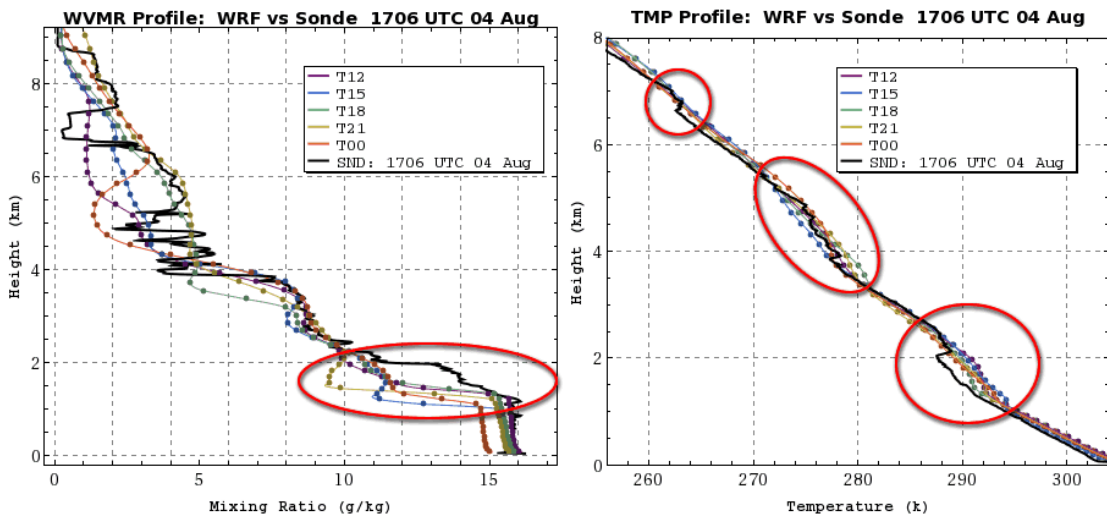


Figure A.3: Initialization sensitivity runs compared with 1706 UTC 4 August radiosonde: left profile is (a) mixing ratio and right profile is (b) temperature.

Later that evening another sonde was released at 2313 UTC 4 August, approximately when the cold front was passing over Beltsville. WRF was not able to capture the quick erosion of moisture 2-4 km AGL by the frontal passage (Figure A.4a). Measurements show that within 6 hours mixing ratio at 3 km dropped from 9 g kg⁻¹ down to 0.5 g kg⁻¹. The model was not able to adjust quickly enough to the incoming dry air and still showed a mixing ratio of 3-5 g kg⁻¹ within this region. However, moisture profiles above and below this were in agreement with observations. In this sounding, the U-wind broke more significantly with observation by consistently overestimating the 4-7 km values and not reproducing the sub-kilometer easterly flow from the cold front (Figure A.4b). The V-wind observation profile continued to show oscillations that the model runs could not mimic. It is supposed that too much kinetic energy was transferred between layers which were not properly isolated by the multiple subsidence inversion layers, which acted to smooth the overall wind profile.

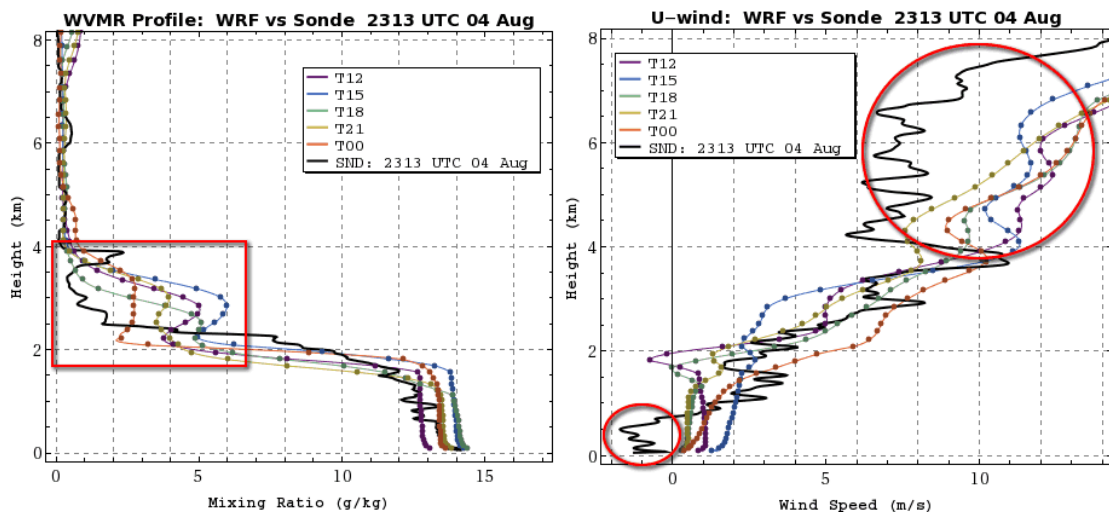


Figure A.4: Initialization sensitivity runs compared with 2313 UTC 4 August radiosonde: left profile is (a) mixing ratio and right profile is (b) U-wind.

The 0601 UTC 5 August radiosonde reflected the first post-front sounding. Mixing ratio profiles varied significantly between the runs (Figure A.5a). Sonde data showed the PBL had retained a well-mixed humidity profile late into nighttime hours which sharply decreased above 2 km. Although the T00 retained the best shape, all runs indicated the model was simulating a stable PBL with moisture quickly eroding from the top down under the post-frontal air mass. In reality, however, it appeared that strong nocturnal winds created turbulent mixing below a very strong inversion trapping moisture in the PBL. Model temperature profiles clearly showed the absence of this inversion (Figure A.5b) which undoubtedly contributed to an inaccurate PBL moisture profile. Unfortunately, radiosonde equipment malfunctions resulted in loss of wind information below 3.5 km, so further investigation of PBL winds from radiosonde data could not be done.

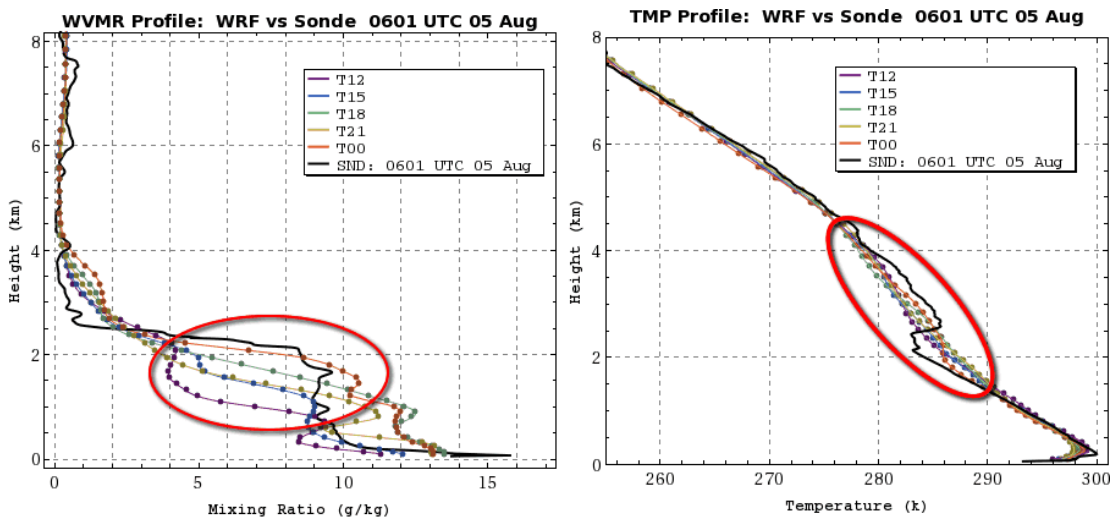


Figure A.5: Initialization sensitivity runs compared with 0601 UTC 5 August radiosonde: left profile is (a) mixing ratio and right profile is (b) temperature.

During the afternoon of 5 August, a final sonde was launched at 1837 UTC. No model runs were able to represent the amount of moisture in the PBL correctly (Figure A.6a). This is likely linked to the model deficiency discussed in the previous

sounding. They were $1-3 \text{ g kg}^{-1}$ drier than observations, with the latest initialization time, T00, performing worst, and the initialization time just 3 hours prior performing best. However, model comparisons above the PBL were quite good. In fact, WRF was able to accurately depict BLH and a moist layer 5-7 km AGL. U-wind comparisons were very good among the runs. V-wind comparisons showed all runs did not represent the northerly winds in a 5-13 km layer well (Figure A.6b). In this region winds were observed to be 10 m s^{-1} stronger than model simulations. This was the most significant model deviation in upper level winds. As in the previous soundings, all initialization runs tended to auto-correlate in this stable regime, but fine scale observations did not necessarily converge.

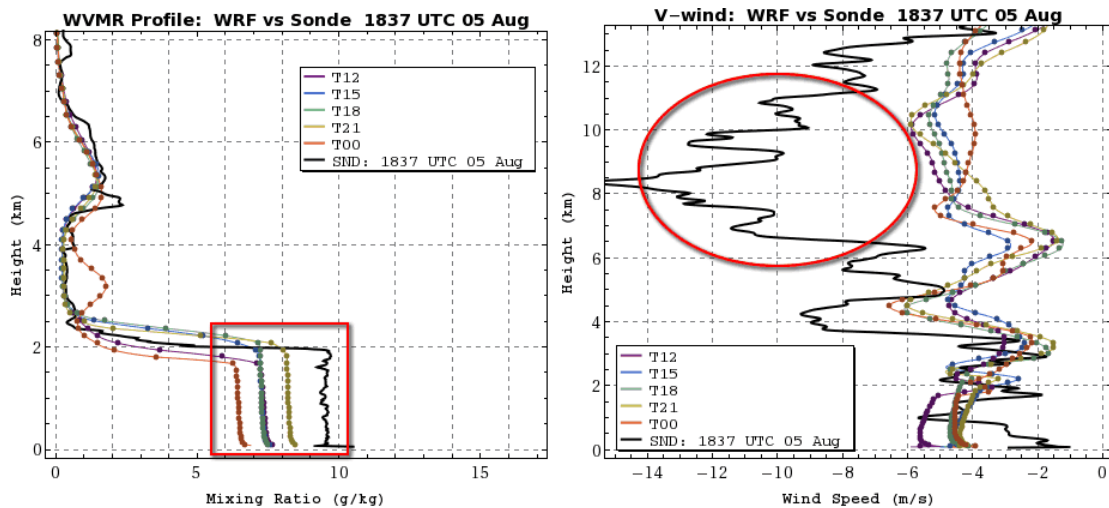


Figure A.6: Initialization sensitivity runs compared with 1837 UTC 5 August radiosonde: left profile is (a) mixing ratio and right profile is (b) V-wind.

Appendix B: Post-processing and Graphics Generation

B.1 WRF Output

For the high resolution numerical simulations, WRF data was output every 15 min for D1 and every 5 min for D2. Output frames were lumped into hourly files so they had a more manageable size. An important aspect of post-processing WRF data was to use software that could efficiently handle operations on large files. The functions provided within the Netcdf Operator (NCO) software (<http://nco.sourceforge.net/>) allowed easy and computationally efficient manipulation of WRF output. The most useful functions included spatio-temporal sub sampling (*ncks*) to extract vertical profiles, cross-sections, domain subsets, or separation of output time frames from the larger output history file. Likewise, output times could be concatenated together (*ncrcat*). Arithmetic operations can also be applied to field variables (*ncap2*). Furthermore, there are functions tailored for working with ensemble data (*ncea*, *necat*).

B.2 Intermediate Processing

The post-processing of WRF variables was done using Mathematica, Matlab, and NCAR Command Language (NCL). All three software packages allowed direct input/output of netcdf files. The basic strategy was to post-process all WRF/NCO files using the above software and then output the newly computed meteorological fields on other vertical coordinates in netcdf files. These intermediate files consumed storage space but saved additional computational overhead down the road. NCL has a library with several WRF functions that were particularly useful for calculating more

cumbersome fields, such as CAPE, CIN, reflectivity, etc. However, it was more tedious to write netcdf files from NCL than either Matlab or Mathematica.

B.3 Mathematica Graphics

Most graphics in this dissertation were created using Mathematica. Mathematica has a steep learning curve but can ultimately do virtually any computational or graphical task with fine control over plotting details. The following section will broadly convey some important points in generating graphics.

First, most plots in this dissertation were graphics overlays. For this, the *Show* function was used to combine several independent plots into a combined graphic. Example code snippets that generated Figure 3.7a will be shown in the following subsections.

B.3.1 Function "ArrayPlot"

Starting with the bottom layer of the plot, the wind speed shading was produced by:

```
gWspd=ArrayPlot[wspd2d,ColorFunctionScaling->False,
                ColorFunction->Function[{z},Which[z<0,Transparent,z>maxWspd,
                MyColorFunc1[1],True,MyColorFunc1[z/maxWspd]]]];

```

where a custom color function (*MyColorFunc1*) for wind speed was created by:

```
colorLst={Pink,Magenta,Purple,Blue,Cyan,RGBColor[0,.5,0],Green,Yellow,Orange,
          Red,RGBColor[.5,0,0]};
redFunc=Interpolation[Thread[{Range[0,1,1/(Length[colorLst]-1)],
                              colorLst[[All,1]]}],InterpolationOrder->1];
grnFunc=Interpolation[Thread[{Range[0,1,1/(Length[colorLst]-1)],
                              colorLst[[All,2]]}],InterpolationOrder->1];
bluFunc=Interpolation[Thread[{Range[0,1,1/(Length[colorLst]-1)],
                              colorLst[[All,3]]}],InterpolationOrder->1];
MyColorFunc1[n_]:=RGBColor[redFunc[n],grnFunc[n],bluFunc[n]];

```

The above routine will generate a graphics object ($gWspd$) showing wind speed shading from a two dimensional array of data ($wspd2d$).

B.3.2 Function "ListContourPlot"

The next layer in the example plot is the θ contour graphic which is produced by:

```
gThCnt=ListContourPlot[theta2d,Contours->thLevs,
    ContourStyle->Directive[AbsoluteThickness[.75],Darker[White,.1]],
    ContourShading->Transparent];
```

where custom θ contour values ($thLevs$) always include 300 K as a reference with contours spaced according to $d\theta$ above and below the reference:

```
centerθ=300; dθ=10/5; r=Range[0,200,dθ];
thLevs=Select[Union[centerθ-r,centerθ+r],
    Ceiling[minTh,dθ]<=#<=Floor[maxTh,dθ]&];
```

This above routine will produce a graphic object ($gThCnt$) of θ contours.

B.3.3 Function "ListVectorPlot"

Wind vectors can be generated using *ListVectorPlot*. As with the former plotting functions, there are many optional parameters that are omitted in these examples that can be used to override default values. It would behoove the user to explore these options to understand what Mathematica is capable of generating.

```
gVect=ListVectorPlot[vectLst,VectorPoints->vectLst[[All,1]],
    VectorStyle->Directive[Opacity[1.],Black,AbsoluteThickness[1]],
    VectorScale->{.018,0.9,None}]
```

The above function outputs a graphic object ($gVect$) showing wind vectors where the input variable ($vectLst$) is a list of objects $\{\{x,z\},\{u,w\}\}$ that represent the wind components at a given location.

B.3.4 Graphics primitives

Mathematica has the ability to plot many types of graphics primitives (circles, spheres, lines, etc.) including polygon objects. It is useful to use polygons to represent the terrain profile of a cross-section.

```
pts=Thread[{Range[nxM],HGT[[j]]}];
pts=Join[pts,{{nxM,0},{1,0}}];
gTerr=Graphics[{FaceForm[Darker[Brown]],EdgeForm[{Black,Thin}],Polygon[pts]}];
```

The above code produces a polygon graphic object (*gTerr*) where the input was WRF terrain height (*HGT*) at a given y-cross-section (*j*) having an x-dimension length (*nxM*).

The blue lines that designated locations of water bodies (Figure 3.7a) were created similar to the above, but used *Line* instead of *Polygon*.

B.3.5 Function "Show"

As previously mentioned, the final step (in Mathematica) of generating Figure 3.7a is to assemble all graphics layers together similar to the onion skinning process used in animation.

```
gFnl=Show[{gWspd,gThCnt,gVect,gTerr,gWat},
PlotRange->{{1,nxM},{0,4}},PlotRangePadding->0,
PlotRangeClipping->True,AspectRatio->1/3,ImageSize->800,
Frame->True,FrameStyle->AbsoluteThickness[1],
FrameTicks->{xTks1,yTks1,xTks2,yTks2}]
```

where *xTks1*, *yTks1*, ..., etc. are custom lists that specify tick marks on the graphic (see below). Provided that all graphic objects use the same coordinates, they can all be overlaid into a final graphic. This is a very powerful feature enabling virtually unlimited graphic compositions.

B.3.6 Tick marks

It is very important to explore all available options for a given plotting function. For example, calling `Options[ListContourPlot]` will display a variety of default options that can be overridden to precisely control the appearance of the graphic that is produced. One such example is the `(Frame)Ticks` option. One can use this option to define custom tick mark spacing, placing, line width/length, etc for each independent plot frame or axis. Tick mark labels can display text as well as numbers, which can be independent from the plot coordinates. This is a very useful trick for generating specialized plots such as atmospheric soundings. In this case, negative values can be assigned to all pressure data (y-axis) while overriding the default `Ticks` to display their absolute value instead of their real value, thus giving the appearance that the y-axis is reversed (e.g. 1000 mb at bottom and 100 mb at top).

```
minor={{0.005,0.},{GrayLevel[0],Opacity[.5],AbsoluteThickness[0.75]}};
major={{0.01,0.},{GrayLevel[0],AbsoluteThickness[1.20]}};
TxtSty[x_]:=Style[ToString[x],12,FontFamily->"Arial",FontWeight->"Normal"]
yMin=-1000; yMax=-100; yDelMj=50; yDelMn=25;
yTcks1=Join[{
  Map[Join[{#,TxtSty[Abs[#]]},major]&,Range[yMinMj=Ceiling[yMin,yDelMj],
  yMaxMj=Floor[yMax,yDelMj],yDelMj]],
  Map[Join[{#,TxtSty[" "]},minor]&,Range[yMinMn=Floor[yMin,yDelMn],
  yMaxMn=Ceiling[yMax,yDelMn],yDelMn]]];
```

The `(Frame)TicksStyle` parameter can also be used to assign color, line thickness, etc. The ability to precisely control the finest details of plotting is what makes Mathematica so appealing for graphics generation.

B.3.6 GIS data

Geographic projections can be done in Mathematica but it is somewhat arduous. For example, the State and County boundaries in Figure 3.5 were downloaded from the USGS seamless data distribution server. These SHP files can be read by Mathematica, but the coordinate system is lat-lon. These boundaries had to be re-projected into the Lambert Conformal projection, which was native grid for the WRF simulations. To do this, it is possible to use:

```
Map[GeogridPosition[GeoPosition[#, "ITRF00"], proj]&, latLonList]
```

where *proj* is projection information (e.g. Lambert Conformal specifications) and *latLonList* is the coordinate list to be remapped. The resulting data points can then be linearly scaled to fit the model grid and plotted as a polygon overlay for the desired graphic.

In conclusion, the above descriptions represent a few examples of how to use Mathematica to generate graphics, but there is no substitute for learning the details of the programming language. The graphics in this dissertation were produced with advanced knowledge in Mathematica programming.

B.4 Adobe Software

The final step in the graphics pipeline was to use Adobe Illustrator to add finishing touches that make the graphics publication-worthy. First, the graphics in Mathematica needed to be exported as EPS or PDF files (vector format). These files were imported by Illustrator so that all plot line work (contours, axes, labels, etc) was vectorized. Plot shading is not vectorized but imported as an image. The benefit of working with vector data is that the graphics can be precisely sized for any given

publication specifications. Font sizes and line thickness can be directly manipulated to ensure that they meet the publication criteria (e.g. no line widths below 0.5 pt). Illustrator also provides several professional drawing tools that make the addition of legends or arrows on diagrams easy to add. Layout tools also make it easy to perfectly align and scale multi-paneled plots. The graphics produced by Illustrator can be saved as a vector PDF or a high resolution image to meet the criteria of the publisher.

Adobe Photoshop was used to generate animations. Looping functions in Mathematica were used to output a sequence of image files at each desired model time. These images were imported by Photoshop and then converted to movie files (wmv, avi, mov, etc).

Bibliography

- Adam, M., and Coauthors, 2010: Water vapor measurements by Howard University Raman lidar during the WAVES 2006 campaign. *J. Atmos. Ocean. Technol.*, **27**, 42-60.
- Andreas, E. L., K. J. Claffy, and A. P. Makshtas, 2000: Low-level atmospheric jets and inversions over the western Weddell Sea. *Boundary Layer Meteorol.*, **97**, 459-486.
- Ansmann, A., U. Wandinger, M. Riebesell, C. Weitkamp, and W. Michaelis, 1992a: Independent measurement of extinction and backscatter profiles in cirrus clouds by using a combined Raman elastic-backscatter lidar. *Appl. Opt.*, **31**, 7113-7113.
- Ansmann, A., M. Riebesell, U. Wandinger, C. Weitkamp, E. Voss, W. Lahmann, and W. Michaelis, 1992b: Combined raman elastic-backscatter LIDAR for vertical profiling of moisture, aerosol extinction, backscatter, and LIDAR ratio. *Appl. Phys. B*, **55**, 18-28.
- Arshinov, Y., and Coauthors, 2005: Daytime operation of a pure rotational Raman lidar by use of a Fabry-Perot interferometer. *Appl. Opt.*, **44**, 3593-3603.
- Arya, S. P. S., 1981: Parameterizing the Height of the Stable Atmospheric Boundary Layer. *J. Appl. Meteorol.*, **20**, 1192-1202.
- Atlas, D., 1960: RADAR DETECTION OF THE SEA BREEZE. *J. Meteorol.*, **17**, 244-258.

- Baas, P., F. C. Bosveld, H. Klein Baltink, and A. A. M. Holtslag, 2009: A climatology of nocturnal low-level jets at Cabauw. *J. Appl. Meteor. Climatol.*, **48**, 1627-1642.
- Bader, D. C., and T. B. McKee, 1992: Mesoscale boundary-layer evolution over complex terrain. Part II: Factors controlling nocturnal boundary-layer structure. *Mon. Weather Rev.*, **120**, 802-816.
- Baker, R. D., B. H. Lynn, A. Boone, W.-K. Tao, and J. Simpson, 2001: The Influence of Soil Moisture, Coastline Curvature, and Land-Breeze Circulations on Sea-Breeze-Initiated Precipitation. *Journal of Hydrometeorology*, **2**, 193-211.
- Banta, R., and W. R. Cotton, 1981: An Analysis of the Structure of Local Wind Systems in a Broad Mountain Basin. *J. Appl. Meteorol.*, **20**, 1255-1266.
- Banta, R. M., L. D. Olivier, and D. H. Levinson, 1993: Evolution of the Monterey Bay Sea-Breeze Layer As Observed by Pulsed Doppler Lidar. *J. Atmos. Sci.*, **50**, 3959-3982.
- Banta, R. M., R. K. Newsom, J. K. Lundquist, Y. L. Pichugina, R. L. Coulter, and L. Mahrt, 2002: Nocturnal low-level jet characteristics over Kansas during Cases-99. *Boundary Layer Meteorol.*, **105**, 221-252.
- Banta, R. M., L. S. Darby, J. D. Fast, J. O. Pinto, C. D. Whiteman, W. J. Shaw, and B. W. Orr, 2004: Nocturnal Low-Level Jet in a Mountain Basin Complex. Part I: Evolution and Effects on Local Flows. *J. Appl. Meteorol.*, **43**, 1348-1365.
- Bao, J. W., S. A. Michelson, P. O. G. Persson, I. V. Djalalova, and J. M. Wilczak, 2008: Observed and WRF-Simulated Low-Level Winds in a High-Ozone

- Episode during the Central California Ozone Study. *J. Appl. Meteor. Climatol.*, **47**, 2372-2394.
- Behrendt, A., T. Nakamura, M. Onishi, R. Baumgart, and T. Tsuda, 2002: Combined Raman Lidar for the Measurement of Atmospheric Temperature, Water Vapor, Particle Extinction Coefficient, and Particle Backscatter Coefficient. *Appl. Opt.*, **41**, 7657-7666.
- Blackadar, A. K., 1957: Boundary layer wind maxima and their significance for the growth of nocturnal inversions. *Bull. Am. Meteorol. Soc.*, **38**, 283-290.
- Blier, W., 1998: The Sundowner winds of Santa Barbara, California. *Weather and forecasting*, **13**, 702-716.
- Bonner, W. D., 1968: Climatology of the low level jet. *Mon. Weather Rev.*, **96**, 833-850.
- Bonner, W. D., and J. A. N. Paegle, 1970: Diurnal Variations in Boundary Layer Winds Over the South-central United States in Summer. *Mon. Weather Rev.*, **98**, 735-744.
- Bosart, L. F., V. Pagnotti, and B. Lettau, 1973: Climatological aspects of eastern United States back-door cold frontal passages. *Mon. Weather Rev.*, **101**, 627-635.
- Bösenberg, J., 1998: Ground-Based Differential Absorption Lidar for Water-Vapor and Temperature Profiling: Methodology. *Appl. Opt.*, **37**, 3845-3860.
- Bossert, J. E., 1997: An Investigation of Flow Regimes Affecting the Mexico City Region. *J. Appl. Meteorol.*, **36**, 119-140.

- Bossert, J. E., and W. R. Cotton, 1994: Regional-Scale Flows in Mountainous Terrain. Part I: A Numerical and Observational Comparison. *Mon. Weather Rev.*, **122**, 1449-1471.
- Bougeault, P., and P. Lacarrere, 1989: Parameterization of Orography-Induced Turbulence in a Mesobeta--Scale Model. *Mon. Weather Rev.*, **117**, 1872-1890.
- Brinkmann, W. A. R., 1974: Strong downslope winds at Boulder, Colorado. *Mon. Weather Rev.*, **102**, 592-602.
- Browell, E. V., T. D. Wilkerson, and T. J. McIlrath, 1979: Water vapor differential absorption lidar development and evaluation. *Appl. Opt.*, **18**, 3474-3483.
- Catalano, F., and A. Cenedese, 2010: High-Resolution Numerical Modeling of Thermally Driven Slope Winds in a Valley with Strong Capping. *J. Appl. Meteor. Climatol.*, **49**, 1859-1880.
- Clark, A. J., W. A. Gallus, and T.-C. Chen, 2008: Contributions of Mixed Physics versus Perturbed Initial/Lateral Boundary Conditions to Ensemble-Based Precipitation Forecast Skill. *Mon. Weather Rev.*, **136**, 2140-2156.
- Clark, A. J., W. A. Gallus, M. Xue, and F. Kong, 2009: A Comparison of Precipitation Forecast Skill between Small Convection-Allowing and Large Convection-Parameterizing Ensembles. *Weather and forecasting*, **24**, 1121-1140.
- Clarke, J. F., 1969: Nocturnal Urban Boundary Layer Over Cincinnati, Ohio. *Mon. Weather Rev.*, **97**, 582-589.

- Colle, B. A., and C. F. Mass, 1998: Windstorms along the Western Side of the Washington Cascade Mountains. Part II: Characteristics of Past Events and Three-Dimensional Idealized Simulations. *Mon. Weather Rev.*, **126**, 53-71.
- Colle, B. A., and D. R. Novak, 2009: The New York Bight Jet: Climatology and dynamical evolution. *Mon. Weather Rev.*, **138**, 2385-2404.
- Cuxart, J., M. A. Jiménez, and D. Martínez, 2007: Nocturnal Meso-Beta Basin and Katabatic Flows on a Midlatitude Island. *Mon. Weather Rev.*, **135**, 918-932.
- Darby, L. S., R. M. Banta, and R. A. Pielke, 2002: Comparisons between Mesoscale Model Terrain Sensitivity Studies and Doppler Lidar Measurements of the Sea Breeze at Monterey Bay. *Mon. Weather Rev.*, **130**, 2813-2838.
- Darby, L. S., K. J. Allwine, and R. M. Banta, 2006: Nocturnal Low-Level Jet in a Mountain Basin Complex. Part II: Transport and Diffusion of Tracer under Stable Conditions. *J. Appl. Meteor. Climatol.*, **45**, 740-753.
- Davis, C., B. Brown, and R. Bullock, 2006: Object-Based Verification of Precipitation Forecasts. Part II: Application to Convective Rain Systems. *Mon. Weather Rev.*, **134**, 1785-1795.
- Davis, C. A., K. W. Manning, R. E. Carbone, S. B. Trier, and J. D. Tuttle, 2003: Coherence of Warm-Season Continental Rainfall in Numerical Weather Prediction Models. *Mon. Weather Rev.*, **131**, 2667-2679.
- de Foy, B., A. Clappier, L. T. Molina, and M. J. Molina, 2006: Distinct wind convergence patterns in the Mexico City basin due to the interaction of the gap winds with the synoptic flow. *Atmos. Chem. Phys.*, **6**, 1249-1265.

- De Wekker, S. F. J., D. G. Steyn, J. D. Fast, M. W. Rotach, and S. Zhong, 2005: The performance of RAMS in representing the convective boundary layer structure in a very steep valley. *Environ. Fluid Mech.*, **5**, 35-62.
- Decker, S. G., and D. A. Robinson, 2011: Unexpected high winds in northern New Jersey: A downslope windstorm in modest topography. *Weather and forecasting*, **26**, 902-921.
- Di Girolamo, P., R. Marchese, D. N. Whiteman, and B. B. Demoz, 2004: Rotational Raman Lidar measurements of atmospheric temperature in the UV. *Geophys. Res. Lett.*, **31**, L01106.
- Done, J., C. A. Davis, and M. Weisman, 2004: The next generation of NWP: explicit forecasts of convection using the weather research and forecasting (WRF) model. *Atmos. Sci. Lett.*, **5**, 110-117.
- Ebert, E. E., 2008: Fuzzy verification of high-resolution gridded forecasts: a review and proposed framework. *Meteorol. Appl.*, **15**, 51-64.
- Ebert, E. E., and J. L. McBride, 2000: Verification of precipitation in weather systems: determination of systematic errors. *J. Hydrol.*, **239**, 179-202.
- Estoque, M. A., 1981: Further Studies of a Lake Breeze Part I: Observational Study. *Mon. Weather Rev.*, **109**, 611-618.
- Estoque, M. A., and J. M. Gross, 1981: Further Studies of a Lake Breeze Part II: Theoretical Study. *Mon. Weather Rev.*, **109**, 619-634.
- Estournel, C., and D. Guedalia, 1985: Influence of Geostrophic Wind on Atmospheric Nocturnal Cooling. *J. Atmos. Sci.*, **42**, 2695-2698.

- Etherton, B., and P. Santos, 2008: Sensitivity of WRF Forecasts for South Florida to Initial Conditions. *Weather and forecasting*, **23**, 725-740.
- Farquharson, J. S., 1939: The diurnal variation of wind over tropical Africa. *Q. J. R. Meteorolog. Soc.*, **65**, 165-184.
- Fast, J. D., and L. S. Darby, 2004: An Evaluation of Mesoscale Model Predictions of Down-Valley and Canyon Flows and Their Consequences Using Doppler Lidar Measurements during VTMX 2000. *J. Appl. Meteorol.*, **43**, 420-436.
- Feng, J., and Y.-L. Chen, 2001: Numerical Simulations of Airflow and Cloud Distributions over the Windward Side of the Island of Hawaii. Part II: Nocturnal Flow Regime. *Mon. Weather Rev.*, **129**, 1135-1147.
- Ferrare, R., and Coauthors, 2006: Evaluation of daytime measurements of aerosols and water vapor made by an operational Raman lidar over the Southern Great Plains. *J. Geophys. Res.*, **111**, D05S08.
- Gaffin, D. M., 2009: On high winds and Foehn warming associated with mountain-wave events in the western foothills of the southern Appalachian Mountains. *Weather and forecasting*, **24**, 53-75.
- Gallus, W. A., and J. F. Bresch, 2006: Comparison of Impacts of WRF Dynamic Core, Physics Package, and Initial Conditions on Warm Season Rainfall Forecasts. *Mon. Weather Rev.*, **134**, 2632-2641.
- Garratt, J. R., 1982: Surface Fluxes and the Nocturnal Boundary-Layer Height. *J. Appl. Meteorol.*, **21**, 725-729.
- Gentry, B. M., H. Chen, and S. X. Li, 2000: Wind measurements with 355-nm molecular Doppler lidar. *Opt. Lett.*, **25**, 1231-1233.

- Givati, A., and D. Rosenfeld, 2004: Quantifying precipitation suppression due to air pollution. *J. Appl. Meteorol.*, **43**, 1038-1056.
- Godowitch, J. M., J. K. S. Ching, and J. F. Clarke, 1985: Evolution of the nocturnal inversion layer at an urban and nonurban location. *J. Clim. Appl. Meteorol.*, **24**, 791-804.
- Goldsmith, J. E. M., F. H. Blair, S. E. Bisson, and D. D. Turner, 1998: Turn-key Raman lidar for profiling atmospheric water vapor, clouds, and aerosols. *Appl. Opt.*, **37**, 4979-4990.
- Gopalakrishnan, S. G., M. Sharan, R. T. McNider, and M. P. Singh, 1998: Study of radiative and turbulent processes in the stable boundary layer under weak wind conditions. *J. Atmos. Sci.*, **55**, 954-960.
- Grell, G. A., and D. Dévényi, 2002: A generalized approach to parameterizing convection combining ensemble and data assimilation techniques. *Geophys. Res. Lett.*, **29**, 1693.
- Grisogono, B., and D. Belušić, 2009: A review of recent advances in understanding the meso- and microscale properties of the severe Bora wind. *Tellus A*, **61**, 1-16.
- Grubisic, V., and M. Xiao, 2006: Climatology of westerly wind events in the lee of the Sierra Nevada. *12th Conf. on Mountain Meteorology*, Amer. Meteor. Soc.
- Hacker, J. P., and C. Snyder, 2005: Ensemble Kalman Filter Assimilation of Fixed Screen-Height Observations in a Parameterized PBL. *Mon. Weather Rev.*, **133**, 3260-3275.

- Hakim, G. J., 1992: The eastern United States side-door cold front of 22 April 1987: A case study of an intense atmospheric density current. *Mon. Weather Rev.*, **120**, 2738-2762.
- Haman, C. L., B. Lefer, and G. A. Morris, 2012: Seasonal variability in the diurnal evolution of the boundary layer in a near coastal urban environment. *J. Atmos. Ocean. Technol.*
- Helfand, H. M., and S. D. Schubert, 1995: Climatology of the Simulated Great Plains Low-Level Jet and Its Contribution to the Continental Moisture Budget of the United States. *J. Clim.*, **8**, 784-806.
- Hidalgo, J., V. Masson, and L. Gimeno, 2009: Scaling the Daytime Urban Heat Island and Urban-Breeze Circulation. *J. Appl. Meteor. Climatol.*, **49**, 889-901.
- Higgins, R. W., Y. Yao, E. S. Yarosh, J. E. Janowiak, and K. C. Mo, 1997: Influence of the Great Plains Low-Level Jet on Summertime Precipitation and Moisture Transport over the Central United States. *J. Clim.*, **10**, 481-507.
- Holton, J. R., 1967: The diurnal boundary layer wind oscillation above sloping terrain. *Tellus*, **19**, 199-205.
- , 2004: *An introduction to dynamic meteorology*. 4th ed. Elsevier Academic Press, xii, 535 p. pp.
- Hong, S.-s., and P.-l. Lin, 1982: Topographic Effects on the Land-Sea Breeze Circulation. *Bulletin of Geophysics, National Central University*, **23**.
- Hong, S.-Y., and H.-L. Pan, 1996: Nonlocal Boundary Layer Vertical Diffusion in a Medium-Range Forecast Model. *Mon. Weather Rev.*, **124**, 2322-2339.

- Hong, S.-Y., Y. Noh, and J. Dudhia, 2006: A New Vertical Diffusion Package with an Explicit Treatment of Entrainment Processes. *Mon. Weather Rev.*, **134**, 2318-2341.
- Hu, X.-M., J. W. Nielsen-Gammon, and F. Zhang, 2010: Evaluation of Three Planetary Boundary Layer Schemes in the WRF Model. *J. Appl. Meteor. Climatol.*, **49**, 1831-1844.
- Ismail, S., and E. V. Browell, 1989: Airborne and spaceborne lidar measurements of water vapor profiles: a sensitivity analysis. *Appl. Opt.*, **28**, 3603-3615.
- Janjić, Z. I., 1994: The Step-Mountain Eta Coordinate Model: Further Developments of the Convection, Viscous Sublayer, and Turbulence Closure Schemes. *Mon. Weather Rev.*, **122**, 927-945.
- , 2000: Comments on “Development and Evaluation of a Convection Scheme for Use in Climate Models”. *J. Atmos. Sci.*, **57**, 3686-3686.
- Jankov, I., W. A. Gallus, M. Segal, B. Shaw, and S. E. Koch, 2005: The Impact of Different WRF Model Physical Parameterizations and Their Interactions on Warm Season MCS Rainfall. *Weather and forecasting*, **20**, 1048-1060.
- Jauregui, E., and E. Romales, 1996: Urban effects on convective precipitation in Mexico city. *Atmos. Environ.*, **30**, 3383-3389.
- Jiang, Q., J. D. Doyle, and R. B. Smith, 2006: Interaction between Trapped Waves and Boundary Layers. *J. Atmos. Sci.*, **63**, 617-633.
- Jiang, X., N.-C. Lau, I. M. Held, and J. J. Ploshay, 2007: Mechanisms of the Great Plains low-level jet as simulated in an AGCM. *J. Atmos. Sci.*, **64**, 532-547.

- Kain, J. S., 2004: The Kain–Fritsch Convective Parameterization: An Update. *J. Appl. Meteorol.*, **43**, 170-181.
- Karipot, A., M. Y. Leclerc, and G. Zhang, 2009: Characteristics of nocturnal low-level jets observed in the north Florida area. *Mon. Weather Rev.*, **137**, 2605-2621.
- Keeler, J. M., and D. A. R. Kristovich, 2012: Observations of Urban Heat Island Influence on Lake-Breeze Frontal Movement. *J. Appl. Meteor. Climatol.*, **51**, 702-710.
- Keen, C. S., and W. A. Lyons, 1978: Lake/Land Breeze Circulations on the Western Shore of Lake Michigan. *J. Appl. Meteorol.*, **17**, 1843-1855.
- Klemp, J. B., and D. R. Lilly, 1975: The dynamics of wave-induced downslope winds. *J. Atmos. Sci.*, **32**, 320-339.
- Koch, S. E., C. Flamant, J. W. Wilson, B. M. Gentry, and B. D. Jamison, 2008: An Atmospheric Soliton Observed with Doppler Radar, Differential Absorption Lidar, and a Molecular Doppler Lidar. *J. Atmos. Ocean. Technol.*, **25**, 1267-1287.
- Koletsis, I., K. Lagouvardos, V. Kotroni, and A. Bartzokas, 2009: Numerical study of a downslope windstorm in northwestern Greece. *Atmospheric Research*, **94**, 178-193.
- Krishna, T. B. P. S. R. V., M. Sharan, S. G. Gopalakrishnan, and Aditi, 2003: Mean structure of the nocturnal boundary layer under strong and weak wind conditions: EPRI case study. *J. Appl. Meteorol.*, **42**, 952-969.

- Kumar, M. S., V. K. Anandan, T. N. Rao, and P. N. Reddy, 2012: A climatological study of the nocturnal boundary layer over a complex-terrain station. *J. Appl. Meteor. Climatol.*, **51**, 813-825.
- Lehner, M., C. D. Whiteman, and S. W. Hoch, 2010: Diurnal Cycle of Thermally Driven Cross-Basin Winds in Arizona's Meteor Crater. *J. Appl. Meteor. Climatol.*, **50**, 729-744.
- Lilly, D. K., 1990: Numerical prediction of thunderstorms—has its time come? *Q. J. R. Meteorolog. Soc.*, **116**, 779-798.
- Lott, F., 2007: The Reflection of a Stationary Gravity Wave by a Viscous Boundary Layer. *J. Atmos. Sci.*, **64**, 3363-3371.
- Mahrer, Y., and R. A. Pielke, 1977: The Effects of Topography on Sea and Land Breezes in a Two-Dimensional Numerical Model. *Mon. Weather Rev.*, **105**, 1151-1162.
- Mahrt, L., 1998: Nocturnal Boundary-Layer Regimes. *Boundary Layer Meteorol.*, **88**, 255-278.
- Mahrt, L., and R. C. Heald, 1979: Comments on "Determining Height of the Nocturnal Boundary Layer". *J. Appl. Meteorol.*, **18**, 383-383.
- Martilli, A., 2002: Numerical study of urban impact on boundary layer structure: Sensitivity to wind speed, urban morphology, and rural soil moisture. *J. Appl. Meteorol.*, **41**, 1247-1266.
- Mastrantonio, G., and Coauthors, 1994: Observations of sea breeze events in Rome and the surrounding area by a network of Doppler sodars. *Boundary Layer Meteorol.*, **71**, 67-80.

- Melfi, S. H., D. Whiteman, and R. Ferrare, 1989: Observation of atmospheric fronts using Raman lidar moisture measurements. *J. Appl. Meteorol.*, **28**, 789-806.
- Mellor, G. L., and T. Yamada, 1982: Development of a turbulence closure model for geophysical fluid problems. *Rev. Geophys.*, **20**, 851-875.
- Mestayer, P. G., and Coauthors, 2005: The urban boundary-layer field campaign in marseille (ubl/clu-escompte): set-up and first results. *Boundary Layer Meteorol.*, **114**, 315-365.
- Meyer, J. H., 1971: Radar Observations of Land Breeze Fronts. *J. Appl. Meteorol.*, **10**, 1224-1232.
- Meyers, M. P., J. S. Snook, D. A. Wesley, and G. S. Poulos, 2003: A Rocky Mountain storm. Part II: The forest blowdown over the west slope of the northern Colorado mountains—observations, analysis, and modeling. *Weather and forecasting*, **18**, 662-674.
- Nakanishi, M., and H. Niino, 2006: An Improved Mellor–Yamada Level-3 Model: Its Numerical Stability and Application to a Regional Prediction of Advection Fog. *Boundary Layer Meteorol.*, **119**, 397-407.
- Nielsen-Gammon, J. W., X.-M. Hu, F. Zhang, and J. E. Pleim, 2010: Evaluation of Planetary Boundary Layer Scheme Sensitivities for the Purpose of Parameter Estimation. *Mon. Weather Rev.*, **138**, 3400-3417.
- Niyogi, D., and Coauthors, 2010: Urban modification of thunderstorms: An observational storm climatology and model case study for the Indianapolis urban region. *J. Appl. Meteor. Climatol.*, **50**, 1129-1144.

- Nkemdirim, L. C., 1986: Chinooks in southern Alberta: Some distinguishing nocturnal features. *Journal of Climatology*, **6**, 593-603.
- Novak, D. R., and B. A. Colle, 2006: Observations of Multiple Sea Breeze Boundaries during an Unseasonably Warm Day in Metropolitan New York City. *Bulletin of the American Meteorological Society*, **87**, 169-174.
- O'Steen, L. B., 2000: Numerical Simulation of Nocturnal Drainage Flows in Idealized Valley-Tributary Systems. *J. Appl. Meteorol.*, **39**, 1845-1860.
- Ólafsson, H., and P. Bougeault, 1997: The Effect of Rotation and Surface Friction on Orographic Drag. *J. Atmos. Sci.*, **54**, 193-210.
- Pan, Z., M. Segal, and R. W. Arritt, 2004: Role of Topography in Forcing Low-Level Jets in the Central United States during the 1993 Flood-Altered Terrain Simulations. *Mon. Weather Rev.*, **132**, 396-403.
- Parish, T. R., and L. D. Oolman, 2010: On the role of sloping terrain in the forcing of the Great Plains low-level jet. *J. Atmos. Sci.*, **67**, 2690-2699.
- Parish, T. R., A. R. Rodi, and R. D. Clark, 1988: A case study of the summertime Great Plains low level jet. *Mon. Weather Rev.*, **116**, 94-105.
- Parker, M. D., and D. A. Ahijevych, 2007: Convective Episodes in the East-Central United States. *Mon. Weather Rev.*, **135**, 3707-3727.
- Peng, M. S., and W. T. Thompson, 2003: Some aspects of the effect of surface friction on flows over mountains. *Q. J. R. Meteorolog. Soc.*, **129**, 2527-2557.
- Pinto, J. O., D. B. Parsons, W. O. J. Brown, S. Cohn, N. Chamberlain, and B. Morley, 2006: Coevolution of Down-Valley Flow and the Nocturnal Boundary Layer in Complex Terrain. *J. Appl. Meteor. Climatol.*, **45**, 1429-1449.

- Pleim, J. E., 2007: A Combined Local and Nonlocal Closure Model for the Atmospheric Boundary Layer. Part I: Model Description and Testing. *J. Appl. Meteor. Climatol.*, **46**, 1383-1395.
- Porson, A., D. Steyn, and G. Schayes, 2007: Sea-breeze scaling from numerical model simulations, part II: Interaction between the sea breeze and slope flows. *Boundary Layer Meteorol.*, **122**, 31-41.
- Qian, T., C. C. Epifanio, and F. Zhang, 2011: Topographic Effects on the Tropical Land and Sea Breeze. *J. Atmos. Sci.*, **69**, 130-149.
- Raphael, M. N., 2003: The Santa Ana winds of California. *Earth Interactions*, **7**, 1-13.
- Rees, D., and I. S. McDermid, 1990: Doppler lidar atmospheric wind sensor: reevaluation of a 355-nm incoherent Doppler lidar. *Appl. Opt.*, **29**, 4133-4144.
- Reichardt, J., S. Reichardt, A. Behrendt, and T. J. McGee, 2002: Correlations among the optical properties of cirrus-cloud particles: Implications for spaceborne remote sensing. *Geophys. Res. Lett.*, **29**, 1668.
- Roberts, N. M., and H. W. Lean, 2008: Scale-Selective Verification of Rainfall Accumulations from High-Resolution Forecasts of Convective Events. *Mon. Weather Rev.*, **136**, 78-97.
- Rosenfeld, D., and T. L. Bell, 2011: Why do tornados and hailstorms rest on weekends? *J. Geophys. Res.*, **116**, D20211.
- Sakiyama, S. K., 1990: Drainage flow characteristics and inversion breakup in two Alberta mountain valleys. *J. Appl. Meteorol.*, **29**, 1015-1030.

- Schmidli, J., G. S. Poulos, M. H. Daniels, and F. K. Chow, 2009: External Influences on Nocturnal Thermally Driven Flows in a Deep Valley. *J. Appl. Meteor. Climatol.*, **48**, 3-23.
- Schultz, D. M., 2005: A review of cold fronts with prefrontal troughs and wind shifts. *Mon. Weather Rev.*, **133**, 2449-2472.
- Seaman, N. L., B. J. Gaudet, D. R. Stauffer, L. Mahrt, S. J. Richardson, J. R. Zielonka, and J. C. Wyngaard, 2011: Numerical prediction of submesoscale flow in the nocturnal stable boundary layer over complex terrain. *Mon. Weather Rev.*, **140**, 956-977.
- Seluchi, M. E., F. A. Norte, P. Satyamurty, and S. C. Chou, 2003: Analysis of Three Situations of the Foehn Effect over the Andes (Zonda Wind) Using the Eta-CPTEC Regional Model. *Weather and forecasting*, **18**, 481-501.
- Shin, H., and S.-Y. Hong, 2011: Intercomparison of Planetary Boundary-Layer Parametrizations in the WRF Model for a Single Day from CASES-99. *Boundary Layer Meteorol.*, **139**, 261-281.
- Simpson, J. E., D. A. Mansfield, and J. R. Milford, 1977: Inland penetration of sea-breeze fronts. *Q. J. R. Meteorolog. Soc.*, **103**, 47-76.
- Sjostedt, D. W., J. T. Sigmon, and S. J. Colucci, 1990: The Carolina nocturnal low-level jet : Synoptic climatology and a case study. *Weather and forecasting*, **5**, 404-415.
- Skamarock, W. C., and Coauthors, 2008: A Description of the Advanced Research WRF Version 3.

- Smith, C. M., and E. D. Skyllingstad, 2009: Investigation of Upstream Boundary Layer Influence on Mountain Wave Breaking and Lee Wave Rotors Using a Large-Eddy Simulation. *J. Atmos. Sci.*, **66**, 3147-3164.
- , 2011: Effects of Inversion Height and Surface Heat Flux on Downslope Windstorms. *Mon. Weather Rev.*, **139**, 3750-3764.
- Song, J., K. Liao, R. L. Coulter, and B. M. Lesht, 2005: Climatology of the low-level jet at the southern Great Plains atmospheric boundary layer experiments site. *J. Appl. Meteorol.*, **44**, 1593-1606.
- Stull, R. B., 1983: Integral Scales for the Nocturnal Boundary Layer. Part 1: Empirical Depth Relationships. *J. Clim. Appl. Meteorol.*, **22**, 673-686.
- Stull, R. B., 1988: *An introduction to boundary layer meteorology*. Vol. 13, Kluwer Academic Publishers, 666-666 pp.
- Sukoriansky, S., B. Galperin, and V. Perov, 2005: 'Application of a New Spectral Theory of Stably Stratified Turbulence to the Atmospheric Boundary Layer over Sea Ice'. *Boundary Layer Meteorol.*, **117**, 231-257.
- Tai-Jen Chen, G., and C.-C. Yu, 1988: Study of Low-Level Jet and Extremely Heavy Rainfall over Northern Taiwan in the Mei-Yu Season. *Mon. Weather Rev.*, **116**, 884-891.
- Tao, W.-K., J. Simpson, and M. McCumber, 1989: An Ice-Water Saturation Adjustment. *Mon. Weather Rev.*, **117**, 231-235.
- Tie, X., S. Madronich, G. Li, Z. Ying, A. Weinheimer, E. Apel, and T. Campos, 2009: Simulation of Mexico City plumes during the MIRAGE-Mex field campaign using the WRF-Chem model. *Atmos. Chem. Phys.*, **9**, 4621-4638.

- Ting, M., and H. Wang, 2006: The Role of the North American Topography on the Maintenance of the Great Plains Summer Low-Level Jet*. *J. Atmos. Sci.*, **63**, 1056-1068.
- Trachte, K., T. Nauss, and J. Bendix, 2010: The Impact of Different Terrain Configurations on the Formation and Dynamics of Katabatic Flows: Idealised Case Studies. *Boundary Layer Meteorol.*, **134**, 307-325.
- Turner, D. D., W. F. Feltz, and R. A. Ferrare, 2000: Continuous water vapor profiles from operational ground-based active and passive remote sensors. *Journal Name: Bulletin of the American Meteorological Society*, *81(6):1301-1317*, Medium: X.
- Uccellini, L. W., 1980: On the Role of Upper Tropospheric Jet Streaks and Leaside Cyclogenesis in the Development of Low-Level Jets in the Great Plains. *Mon. Weather Rev.*, **108**, 1689-1696.
- Verghese, S. J., S. N. Kizhakkemadam, A. Willitsford, J. P. Collier, S. Unni, and C. R. Philbrick, 2003: Characterization of nocturnal jets over Philadelphia during air pollution episodes using radar/RASS and Raman lidar. *AMS 5th Conference on Atmospheric Chemistry*, Long Beach, CA.
- Vermeesch, K., M. Weldegaber, B. Demoz, and V. Demetrius, 2009: Mesoscale Analysis and WRF Model Verification of a Low-Level Jet, Bay Breeze, and Undular Bore at the Howard University Beltsville Research Campus. *American Meteorological Society 13th Conference on Mesoscale Processes*.
- Vickers, D., and L. Mahrt, 2004: Evaluating Formulations of Stable Boundary Layer Height. *J. Appl. Meteorol.*, **43**, 1736-1749.

- Wang, S.-Y., and T.-C. Chen, 2009: The Late-Spring Maximum of Rainfall over the U.S. Central Plains and the Role of the Low-Level Jet. *J. Clim.*, **22**, 4696-4709.
- Wang, W., and N. L. Seaman, 1997: A Comparison Study of Convective Parameterization Schemes in a Mesoscale Model. *Mon. Weather Rev.*, **125**, 252-278.
- Weckwerth, T. M., J. W. Wilson, R. M. Wakimoto, and N. A. Crook, 1997: Horizontal Convective Rolls: Determining the Environmental Conditions Supporting their Existence and Characteristics. *Mon. Weather Rev.*, **125**, 505-526.
- Weisman, M. L., C. Davis, W. Wang, K. W. Manning, and J. B. Klemp, 2008: Experiences with 0–36-h Explicit Convective Forecasts with the WRF-ARW Model. *Weather and forecasting*, **23**, 407-437.
- Weitkamp, C., 2005: Lidar range-resolved optical remote sensing of the atmosphere. Springer, 460.
- Wexler, H., 1961: A Boundary Layer Interpretation of the Low-level Jet. *Tellus*, **13**, 368-378.
- Whiteman, C. D., and X. Bian, 1996: Solar semidiurnal tides in the Troposphere: Detection by radar profilers. *Bulletin of the American Meteorological Society*, **77**, 529-542.
- Whiteman, C. D., and S. Zhong, 2008: Downslope Flows on a Low-Angle Slope and Their Interactions with Valley Inversions. Part I: Observations. *J. Appl. Meteor. Climatol.*, **47**, 2023-2038.

- Whiteman, C. D., X. Bian, and S. Zhong, 1997: Low-level jet climatology from enhanced rawinsonde observations at a site in the southern Great Plains. *J. Appl. Meteorol.*, **36**, 1363-1376.
- Whiteman, D. N., 2003: Examination of the traditional Raman lidar technique. II. Evaluating the ratios for water vapor and aerosols. *Appl. Opt.*, **42**, 2593-2608.
- Whiteman, D. N., B. Demoz, and Z. Wang, 2004: Subtropical cirrus cloud extinction to backscatter ratios measured by Raman Lidar during CAMEX-3. *Geophys. Res. Lett.*, **31**, L12105.
- Whiteman, D. N., K. Rush, I. Veselovskii, M. Cadirola, J. Comer, J. R. Potter, and R. Tola, 2007: Demonstration Measurements of Water Vapor, Cirrus Clouds, and Carbon Dioxide Using a High-Performance Raman Lidar. *J. Atmos. Ocean. Technol.*, **24**, 1377-1388.
- Whiteman, D. N., and Coauthors, 2006: Raman lidar measurements during the International H₂O Project. Part I: Instrumentation and analysis techniques. *J. Atmos. Ocean. Technol.*, **23**, 157-169.
- Wolyn, P. G., and T. B. McKee, 1994: The Mountain-Plains Circulation East of a 2-km-High North-South Barrier. *Mon. Weather Rev.*, **122**, 1490-1508.
- Wulfmeyer, V., and J. Bösenberg, 1998: Ground-Based Differential Absorption Lidar for Water-Vapor Profiling: Assessment of Accuracy, Resolution, and Meteorological Applications. *Appl. Opt.*, **37**, 3825-3844.
- Yamada, T., 1979: Prediction of the Nocturnal Surface Inversion Height. *J. Appl. Meteorol.*, **18**, 526-531.

- Ying, Q., and F. Baopu, 1993: A theoretical study on the interaction between airflow over a mountain and the atmospheric boundary layer. *Boundary Layer Meteorol.*, **64**, 101-126.
- Yoshikado, H., 1990: Vertical Structure of the Sea Breeze Penetrating through a Large Urban Complex. *J. Appl. Meteorol.*, **29**, 878-891.
- Yu, T.-W., 1978: Determining Height of the Nocturnal Boundary Layer. *J. Appl. Meteorol.*, **17**, 28-33.
- Zhang, D.-L., and J. M. Fritsch, 1986: Numerical Simulation of the Meso- β Scale Structure and Evolution of the 1977 Johnstown Flood. Part I: Model Description and Verification. *J. Atmos. Sci.*, **43**, 1913-1944.
- Zhang, D.-L., and W.-Z. Zheng, 2004: Diurnal cycles of surface winds and temperatures as simulated by five boundary layer parameterizations. *J. Appl. Meteorol.*, **43**, 157-169.
- Zhang, D.-L., S. Zhang, and S. J. Weaver, 2006: Low-level jets over the Mid-Atlantic states: Warm-season climatology and a case study. *J. Appl. Meteor. Climatol.*, **45**, 194-209.
- Zhong, S., and C. D. Whiteman, 2008: Downslope Flows on a Low-Angle Slope and Their Interactions with Valley Inversions. Part II: Numerical Modeling. *J. Appl. Meteor. Climatol.*, **47**, 2039-2057.
- Zhong, S., J. D. Fast, and X. Bian, 1996: A Case Study of the Great Plains Low-Level Jet Using Wind Profiler Network Data and a High-Resolution Mesoscale Model. *Mon. Weather Rev.*, **124**, 785-806.

Zumpfe, D. E., and J. D. Horel, 2007: Lake-Breeze Fronts in the Salt Lake Valley. *J. Appl. Meteor. Climatol.*, **46**, 196-211.